Reforming Characteristics of Methane–Ammonia Mixed Fuel on Ni–YSZ Catalyst: Fundamental Study toward Application to SOFC

Katsuyuki TERAMOTO

2020

Reforming Characteristics of Methane–Ammonia Mixed Fuel on Ni–YSZ Catalyst: Fundamental Study toward Application to SOFC

Katsuyuki TERAMOTO

2020

A dissertation submitted in partial fulfillment of the requirements
for the degree of Doctor of Philosophy

Department of Aeronautics and Astronautics
Graduate School of Engineering
Kyoto University

Contents

Acknowledgement

It is my great pleasure to express my sincere appreciation to all people who have supported me throughout my Ph.D. work in the Thermal Engineering Laboratory in Kyoto University.

First of all, my deepest appreciation goes to professor Hiroshi Iwai for his invaluable guidance and extraordinary tolerant support for research. His sharp comments from his deep understanding on the topic always showed me the path to take. I am greatly indebt to professor Hideo Yoshida, whose suggestions and comments, not only for research but for life, from his substantial experience always had inestimable value for me to broaden my view as a responsible person. I would like to express my gratitude to assistant professor Motohiro Saito for his insightful comments and encouragements for my academic life since my master course period. I would also like to express my great appreciation to assistant professor Masashi Kishimoto for his illuminating comments and discussion, and great support for writing papers. I would like to offer special thanks to the members of the Thermal Engineering Laboratory, particularly to Mr. Tomohisa Kawaguchi and Mr. Masashi Takemoto for their passionate hard work for the collaborative research. I would also like to thank Mrs. Nashika Ogami for her generous non-academic assistance.

The academic life with having a job in a company was tough, to be honest, but it has already become my precious memory. The experience through Ph.D. work has brought me the tremendous insights.

Finally, I would like to express my heartfelt thanks to my wife, Mrs. Yuka Teramoto, my son, Mr. Takuto Teramoto, my parents, my brother, and my parents-in-law for their understanding and constant encouragement throughout my study.

Chapter 1

Introduction

1.1 Background

Solid oxide fuel cells (SOFCs) are one type of fuel cells using solid oxide electrolyte that conducts oxygen ions from the air electrode (cathode) to the fuel electrode (anode). Compared to other types of fuel cells, such as polymer electrolyte fuel cells (PEFCs), SOFCs are characterized by their high operation temperature because typical ceramic electrolytes show sufficient ion conductivity at a temperature higher than 600 °C [1,2].

This high operation temperature brings several advantages to SOFCs. One advantage is that SOFCs do not require a precious metal catalyst such as platinum, which is necessary for other type of low-temperature fuel cells. For instance, nickel is widely used as a catalyst for the electrochemical reaction on the anode reactions and this makes SOFCs cost-competitive among the renewable energy market. In fact, several models of SOFC power generation systems for both business and home usage had already been commercialized from the several manufacturers for more than ten years [3]. Another advantage is the efficient heat utilization as a system. Since the operation temperature is relatively high, it is possible to utilize excess

heat for a combined heat and power system (CHP) or a cogeneration system. When a reformer which produces hydrogen from fuels such as hydrocarbons is used, the excess heat can also be used for endothermic reforming reactions [4]. The heat generated in an SOFC stack is transferred to the CHP or the external reformer by thermal radiation and convective heat transfer from the stack surface, which can also be regarded as an external cooling process of the stack for the SOFCs [5]. Fuel flexibility is also a strong advantage of SOFCs [6–21]. Since nickel can work as a catalyst for reforming/decomposition of various fuels such as hydrocarbons and ammonia at the operation temperature of SOFCs, on-site production of hydrogen from the fuels is realized. Therefore, it is allowed for us to choose a fuel depending on the system requirement.

Contrary to the advantages described above, their high operation temperature gives the strict restrictions in its material selection. Since the electrodes are exposed to strongly reduced or oxidizing atmosphere with the high temperature, conventional metal-based materials are not suitable and composite ceramic-based materials have to ensure a long-time stability. In addition, their thermal expansion coefficients should be equivalent to those of electrolyte materials to prevent the mechanical failure during thermal cycle in the operation sequence. Finally, cost issue is also significant considering the current economic situation and the competition against other energy devices. As the materials which meet these requirements, Ni–YSZ (yttria-stabilized zirconia), Ni–GDC (gadolinium-doped ceria) or Ni–SDC (samarium-doped ceria) are typical for the anode, LSM (lanthanum strontium manganite), LSCF (lanthanum strontium cobalt ferrite) or LSC (lanthanum strontium cobaltite) are typical for the cathode, and YSZ, GDC or LSGM (lanthanum strontium gallium magnesium oxide) are typical for the electrolyte [22–25].

Direct reforming of SOFCs has been attracting attention because it allows us to directly supply various hydrogen carriers to SOFCs instead of using an external reformer [4,26–28]. This

operation is possible due to the high operation temperature of SOFCs and catalytic function of nickel in the electrode for reforming/decomposition of the hydrogen carriers. The reformer can thus be eliminated from the system, making it simple and cost-effective. An improvement of the system efficiency is also expected when the endothermic reforming/decomposition reaction in the stack is properly controlled because the endothermic reaction which proceeds inside the stack can be regarded as an internal cooling process of the stack and contribute to realizing a uniform stack temperature. Depending on the reforming/decomposition reaction characteristics of the fuel, however, it is sometimes difficult to control the reaction rate on the cells in the stack. It is often observed that the fuel reacts rapidly near the inlet of the cell so that the local temperature sharply decreases. This causes not only the low performance of the system but also the unacceptable thermal stress, resulting in the mechanical failure of the cell [29–31]. To control the reaction and avoid the drawbacks of direct reforming process, it is important to understand the reaction characteristics of the fuels.

Considering the reaction characteristics among various hydrogen carriers, methane, which is the most commonly adopted fuel, is identified by its strong endothermic nature [6,32,33]. It also has a feature that steam is required in the reforming process. Ammonia is recently attracting attention as a hydrogen carrier. The reaction characteristics of ammonia is totally different from that of methane [34–37]. The endothermic reaction heat is relatively small and the reaction does not require steam. This makes the ammonia decomposition reaction easy to proceed. Detail comparison of hydrogen carriers is discussed in Chapter 2.

Mixing fuel is one method which directly affects the reaction system and controls the reaction process. In fact, in the combustion field, this idea has already been widely attempted [38]. One common example of mixed fuel is bio-fuel mixing to gasoline or diesel [39,40]. Although the original motivation is not controlling the reaction system but is from the environmental concerns in this case, the effect of mixing on the reaction characteristics in

heat engines, such as temperature, pressure, and exhausted gas compositions, has been widely investigated. As for the fuel for SOFCs, however, the concept of mixing fuel has not been widely spread despite its high fuel flexibility. Although a few studies are found which utilize mixed fuel characteristics to suppress a coke formation on the electrode surface [41], no study has been reported for more well-controlled flexible operation of SOFCs.

Considering the various aspects discussed above, the mixed fuel of methane and ammonia is selected in this study. The main objective of this study can be summarized into two parts: i) experimental clarification of methane–ammonia mixed fuel characteristics and verification of possibility to adopt it as a fuel for direct reforming of SOFCs, ii) building up the reaction model including the competitive adsorption phenomenon of methane and ammonia and introducing the reaction rate formulae applicable to stack level simulations of SOFCs fed with the methane–ammonia mixed fuel.

1.2 Outline of the Thesis

Chapter 2 presents the motivation of mixing methane and ammonia referring to the basic knowledge of a surface reaction. The reaction characteristics of various hydrogen carriers are compared and possible combinations of the fuels are discussed. The expected advantages of the methane–ammonia mixed fuel are also considered.

Chapter 3 presents the experimental results of reforming characteristics of the methane–ammonia mixed fuel on a Ni–YSZ catalyst. A small amount of the crashed catalyst is packed in a quartz tube and a mixture gas of methane, ammonia, steam and balance argon is supplied. The test section is placed in an electric furnace to control the catalyst temperature. The exhaust gas compositions are measured by a gas chromatography varying the inlet gas composition and the furnace temperature to clarify the effect of mixture.

Chapter 4 presents the experimental results of several important characteristics as a fuel for solid oxide fuel cells of the methane–ammonia mixed fuel. The streamwise length of the catalyst region packed in the test tube is increased to 21 mm and 42 mm and the temperature distribution of the catalyst along the flow direction is measured by an infrared camera to clarify the reaction region where one fuel is consumed dominantly. Comparing with two different catalyst lengths, the proportion of two reactions, namely steam methane reforming and ammonia decomposition, is estimated along the flow direction. Hydrogen production rate and excess heat utilization of the mixed fuel are compared to those in the case of single fuel of methane or ammonia.

Chapter 5 presents a reaction model and rate formulae of the steam methane reforming and ammonia decomposition considering the situation where methane and ammonia coexist. The concept of adsorption constant is introduced to describe the phenomenon which methane and ammonia are competitively adsorbed on Ni–YSZ catalyst. The model is characterized by

its simple description of the reactions for a computationally-heavily large scale simulation. By fitting the experimental results to the model, reaction rate formulae of the steam methane reforming and ammonia decomposition are estimated. The validity of the reaction rate formulae is examined by comparing the exhausted gas compositions of the numerical simulation with those of the experiments.

Chapter 6 presents the summary of this research and suggestions for the future works.

Bibliography

1. Hoseinnia S, Sadeghzadeh SM. A comparative study of fuel cell technologies and their role in distributed generation. *Ieee Eurocon 2009, Eurocon 2009*. 2009:464-469. doi:10.1109/EURCON.2009.5167673
2. Blum L, Deja R, Peters R, Stolten D. Comparison of efficiencies of low, mean and high temperature fuel cell Systems. *Int J Hydrogen Energy*. 2011;36(17):11056-11067. doi:10.1016/j.ijhydene.2011.05.122
3. Ishikawa T, Yamashita S, Sobue T, Hase K. SOFC development by Tokyo Gas, Kyocera, Rinnai and Gastar. *Int Gas Union World Gas Conf Pap*. 2006;3:1516-1527.
4. Liese EA, Gemmen RS. Performance comparison of internal reforming against external reforming in a solid oxide fuel cell, gas turbine hybrid system. *J Eng Gas Turbines Power*. 2005;127(1):86-90. doi:10.1115/1.1788689
5. Aguiar P, Chadwick D, Kershenbaum L. Modelling of an indirect internal reforming solid oxide fuel cell. *Chem Eng Sci*. 2002;57(1):1665-1677. doi:https://doi.org/10.1016/S0009-2509(02)00058-1
6. Laosiripojana N, Assabumrungrat S. Catalytic steam reforming of methane, methanol, and ethanol over Ni/YSZ: The possible use of these fuels in internal reforming SOFC. *J Power Sources*. 2007;163(2):943-951. doi:10.1016/j.jpowsour.2006.10.006
7. Lo Faro M, La Rosa D, Monforte G, Antonucci V, Arico AS, Antonucci P. Propane conversion over a Ru/CGO catalyst and its application in intermediate temperature solid oxide fuel cells. *J Appl Electrochem*. 2007;37(2):203-208. doi:10.1007/s10800-006-9245-5
8. Farrell B, Linic S. Direct electrochemical oxidation of ethanol on SOFCs: Improved carbon tolerance of Ni anode by alloying. *Appl Catal B Environ*. 2016;183:386-393.

doi:10.1016/j.apcatb.2015.11.002

9. Murray EP, Harris SJ, Jen H. Solid oxide fuel cells utilizing dimethyl ether fuel. *J Electrochem Soc*. 2002;149(9):A1127. doi:10.1149/1.1496484

10. Liu Y, Guo Y, Wang W, et al. Study on proton-conducting solid oxide fuel cells with a conventional nickel cermet anode operating on dimethyl ether. *J Power Sources*. 2011;196(22):9246-9253. doi:10.1016/j.jpowsour.2011.07.051

11. Su C, Ran R, Wang W, Shao Z. Coke formation and performance of an intermediate-temperature solid oxide fuel cell operating on dimethyl ether fuel. *J Power Sources*. 2011;196(4):1967-1974. doi:10.1016/j.jpowsour.2010.10.011

12. Sato K, Tanaka Y, Negishi A, Kato T. Dual fuel type solid oxide fuel cell using dimethyl ether and liquefied petroleum gas as fuels. *J Power Sources*. 2012;217:37-42. doi:10.1016/j.jpowsour.2012.06.001

13. Lo Faro M, Antonucci V, Antonucci PL, Aricó AS. Fuel flexibility: A key challenge for SOFC technology. *Fuel*. 2012;102:554-559. doi:10.1016/j.fuel.2012.07.031

14. Huang TJ, Wu CY, Wang CH. Fuel processing in direct propane solid oxide fuel cell and carbon dioxide reforming of propane over Ni–YSZ. *Fuel Process Technol*. 2011;92(8):1611-1616. doi:10.1016/j.fuproc.2011.04.007

15. Lo Faro M, La Rosa D, Nicotera I, Antonucci V, Aricò AS. Electrochemical investigation of a propane-fed solid oxide fuel cell based on a composite Ni–perovskite anode catalyst. *Appl Catal B Environ*. 2009;89(1-2):49-57. doi:10.1016/j.apcatb.2008.11.019

16. Jiang Y, Virkar A V. A High Performance, Anode-supported solid oxide fuel cell operating on direct alcohol. *J Electrochem Soc*. 2001;148(7):A706. doi:10.1149/1.1375166

17. Liu M, Peng R, Dong D, Gao J, Liu X, Meng G. Direct liquid methanol-fueled solid

oxide fuel cell. *J Power Sources*. 2008;185(1):188-192. doi:10.1016/j.jpowsour.2008.06.076

18. Lo Faro M, Stassi A, Antonucci V, et al. Direct utilization of methanol in solid oxide fuel cells: An electrochemical and catalytic study. *Int J Hydrogen Energy*. 2011;36(16):9977-9986. doi:10.1016/j.ijhydene.2011.05.053
19. Jordão B, Sarruf M, Hong J, Steinberger-wilckens R, Emílio P, Miranda V De. CeO2eCo3O4eCuO anode for direct utilisation of methane or ethanol in solid oxide fuel cells. *Int J Hydrogen Energy*. 2018;43:6340-6351. doi:10.13140/RG.2.2.13804.46721
20. Hong-xin YOU, Guo-dong GAO, Liang Z, Abudula A. Power generating performances of ethanol on the SOFC. *J Fuel Chem Technol*. 2010;38(1):116-120. doi:10.1016/S1872-5813(10)60023-0
21. Steil MC, Nobrega SD, Georges S, Gelin P, Uhlenbruck S, Fonseca FC. Durable direct ethanol anode-supported solid oxide fuel cell. *Appl Energy*. 2017;199(1):180-186. doi:10.1016/j.apenergy.2017.04.086
22. Mahato N, Banerjee A, Gupta A, Omar S, Balani K. Progress in material selection for solid oxide fuel cell technology: A review. *Prog Mater Sci*. 2015;72:141-337. doi:10.1016/j.pmatsci.2015.01.001
23. Shri Prakash B, Senthil Kumar S, Aruna ST. Properties and development of Ni/YSZ as an anode material in solid oxide fuel cell: A review. *Renew Sustain Energy Rev*. 2014;36:149-179. doi:10.1016/j.rser.2014.04.043
24. Shaikh SPS, Muchtar A, Somalu MR. A review on the selection of anode materials for solid-oxide fuel cells. *Renew Sustain Energy Rev*. 2015;51:1-8. doi:10.1016/j.rser.2015.05.069
25. Yokokawa H, Sakai N, Horita T, Yamaji K. Recent developments in solid oxide fuel

cell Materials. *Fuel Cells*. 2001;1(2):117-131.

26. Janardhanan VM, Heuveline V, Deutschmann O. Performance analysis of a SOFC under direct internal reforming conditions. *J Power Sources*. 2007;172(1):296-307. doi:10.1016/j.jpowsour.2007.07.008

27. Peters R, Dahl R, Klüttgen U, Palm C, Stolten D. Internal reforming of methane in solid oxide fuel cell systems. *J Power Sources*. 2002;106(1-2):238-244. doi:10.1016/S0378-7753(01)01039-4

28. Aguiar P, Adjiman CS, Brandon NP. Anode-supported intermediate temperature direct internal reforming solid oxide fuel cell. I: Model-based steady-state performance. *J Power Sources*. 2004;138(1-2):120-136. doi:10.1016/j.jpowsour.2004.06.040

29. Dicks AL. Advances in catalysts for internal reforming in high temperature fuel cells. *J Power Sources*. 1998;71(1-2):111-122. doi:10.1016/S0378-7753(97)02753-5

30. Iwai H, Yamamoto Y, Saito M, Yoshida H. Numerical simulation of intermediate-temperature direct-internal-reforming planar solid oxide fuel cell. *Energy*. 2011;36(4):2225-2234. doi:10.1016/j.energy.2010.03.058

31. Wongchanapai S, Iwai H, Saito M, Yoshida H. Selection of suitable operating conditions for planar anode-supported direct-internal-reforming solid-oxide fuel cell. *J Power Sources*. 2012;204:14-24. doi:10.1016/j.jpowsour.2011.12.029

32. Achenbach E, Riensche E. Methane/steam reforming kinetics for solid oxide fuel cells. *J Power Sources*. 1994;52(2):283-288. doi:10.1016/0378-7753(94)02146-5

33. Achenbach E. Three-dimensional and time-dependent simulation of a planar solid oxide fuel cell stack. *J Power Sources*. 1994;49(1-3):333-348. doi:10.1016/0378-7753(93)01833-4

34. Wojcik A, Middleton H, Damopoulos I, Van Herle J. Ammonia as a fuel in solid oxide fuel cells. *J Power Sources*. 2003;118:342-348. doi:10.1016/S0378-7753(03)00083-1

35. Okanishi T, Okura K, Srifa A, et al. Comparative study of ammonia-fueled solid oxide fuel cell systems. *Fuel Cells*. 2017;17(3):383-390. doi:10.1002/fuce.201600165

36. Klerke A, Christensen CH, Nørskov JK, Vegge T. Ammonia for hydrogen storage: Challenges and opportunities. *J Mater Chem*. 2008;18(20):2304-2310. doi:10.1039/b720020j

37. Lan R, Irvine JTS, Tao S. Ammonia and related chemicals as potential indirect hydrogen storage materials. *Int J Hydrogen Energy*. 2012;37(2):1482-1494. doi:10.1016/j.ijhydene.2011.10.004

38. Tutak W, Lukács K, Szwaja S, Bereczky Á. Alcohol-diesel fuel combustion in the compression ignition engine. *Fuel*. 2015;154:196-206. doi:10.1016/j.fuel.2015.03.071

39. Sadeghinezhad E, Kazi SN, Sadeghinejad F, et al. A comprehensive literature review of bio-fuel performance in internal combustion engine and relevant costs involvement. *Renew Sustain Energy Rev*. 2014;30:29-44. doi:10.1016/j.rser.2013.09.022

40. Golovitchev VI, Yang J. Construction of combustion models for rapeseed methyl ester bio-diesel fuel for internal combustion engine applications. *Biotechnol Adv*. 2009;27(5):641-655. doi:10.1016/j.biotechadv.2009.04.024

41. Wang W, Ran R, Su C, Guo Y, Farrusseng D, Shao Z. Ammonia-mediated suppression of coke formation in direct-methane solid oxide fuel cells with nickel-based anodes. *J Power Sources*. 2013;240:232-240. doi:10.1016/j.jpowsour.2013.04.014

Chapter 2

Concept of Solid Oxide Fuel Cells Directly Fed with Mixed Fuels

2.1 Motivation for Mixing Fuels

The concept of solid oxide fuel cells (SOFCs) directly fed with mixed fuels derives from an idea that more flexible operation can be achieved if the differences of reaction characteristics of each fuel are effectively utilized. It is also expected that it can be a solution for technical difficulties that have not been solved so far and, as a result, prevent SOFCs from being more widely pervasive.

As discussed in Chapter 1, various types of hydrogen carrier such as methane [1–3], propane [4–6], methanol [3,7–9], ethanol [3,7,10–13], dimethyl ether [14–16], carbon monoxide [17–19], and ammonia [20–22] have been considered as well as the conventional hydrogen as fuels for direct reforming of SOFCs. This diversity of fuels is due to the high operation temperature [23,24] and typical anode materials, such as Ni–YSZ (yttria-stabilized zirconia), contain Ni, which works as a reforming/decomposition catalyst for hydrogen carriers [25,26]. The reforming/decomposition reactions of these hydrogen carriers are endothermic, thus, the heat generated by the

electrochemical reaction in SOFCs can be effectively utilized for the reforming/decomposition reactions in the anode, which improves the efficiency of the SOFCs [27–29]. Since the electrochemical reaction is a strongly exothermic reaction, it is ideal if the reforming reaction has a strongly endothermic nature which compensates the reaction heat generated by the electrochemical power generation.

Methane, which is the most commonly adopted fuel today, meets this requirement. The steam methane reforming reaction is one of the strongest endothermic reactions among the reforming of hydrogen carriers. However, one significant problem is its rapid reaction rate near the inlet edge of fuel passages in cells. A large proportion of the supplied methane is reformed near the inlet, resulting in a decrease in local cell temperature. This leads to not only a decline of the cell performance but a steep temperature gradient, rather than a uniform temperature, which generates unacceptable thermal stress and increase the risk of mechanical failure of cells [30–32].

Several approaches have been attempted to cope with this problem. Peters et al. [33] and Ni et al. [34] proposed that methane be partially reformed by a reformer before it is supplied to SOFCs to prevent the intensive reforming reaction near the inlet of the cells. Andersson et al. [35] experimentally investigated the effects of the pre-reforming rate, reported the effectiveness of using a pre-reformer, and successfully mitigated the temperature drop near the inlet. However, the use of a reformer cannot be the best solution compared with the direct reforming operation because SOFC system becomes more complicated. Boder et al. [36] proposed the method of covering the surface of a Ni catalyst near the inlet region with Cu, which is a less active reforming catalyst. They also successfully prevented the sharp temperature drop near the inlet region. One drawback of this method is that there is little operation flexibility. The distribution of the Cu cover should be determined in the design stage and cannot be tuned during the operation, while in an actual operation, the reforming reaction needs to be controlled depending

on the operational load. The usage of ammonia as a directly supplied fuel to SOFCs is also regarded as a method to prevent the steep temperature drop by utilizing the weakly endothermic nature of the ammonia decomposition reaction [20,22]. In this case, the local temperature drop near the inlet can be moderate so that the cell performance can be maintained, but, in return, the advantage of excess heat utilization is also moderate. The restriction of the fuel concentration at the inlet can also be regarded the simplest way to challenge this problem. It can prevent the steep temperature drop by suppressing the amount of endothermic reforming reaction near the inlet, however, the heat utilization efficiency is sacrificed because the amount of excess heat utilization is determined by the overall reactions taking place in the cells. So far, there seems to be no simple method of simultaneously achieving the high excess heat utilization and the suppression of the low-temperature region near the inlet in the direct reforming operation of SOFCs.

In this study, we propose a new approach to this problem: mixing fuels. Since the surface of a Ni catalyst is of primary importance for all reforming/decomposition reactions, if a mixed fuel is supplied, the reactions may compete with each other and proceed selectively. If this is the case, it provides us with an opportunity to delay the start of one (or more) reaction(s) by simply tuning the composition of the supplied mixture gas. It may also be possible to control the location and magnitude of the endothermic reactions.

To have the mixed fuel own the ideal functionality discussed above, we focus on two different characteristics of the component fuels: reaction activity and endothermic/exothermic nature. If the component fuels of the mixed fuel supplied to SOFCs have large differences in their reaction activities, it is expected that one or more reactions which have larger reaction activities proceed selectively when their concentrations are sufficiently high as a result of the competitive reaction situation. This will end up with creating the several regions on the cells where some specific reaction(s) is (are) dominant. Moreover, if these reactions have large

differences in their amounts of reaction heat, since the thermal condition in each region is mainly determined by the dominant reaction(s), the temperature profile in each region is characterized by the endothermic/exothermic nature of the dominant reaction(s) in that region. This indicates that, as a result, the overall temperature distribution in the cell is determined by the reaction activities and endothermic/exothermic natures of the fuels in the mixed fuel. Therefore, the components of the mixed fuel should be carefully selected on the basis of their reaction activities and endothermic/exothermic natures.

2.2 Reaction Characteristics of Hydrogen Carriers

Table 2.1 shows the steam reforming characteristics of typical hydrogen carriers [37–41].The amount of endothermic/exothermic heat and suitable temperatures for their reforming are compared. It also contains the activation energy ΔE, the frequency factor A, and the powers on the concentrations of reactant and steam when their reaction rates are expressed by the power-law type equation, as described in Eq. (2.1) and (2.2).

$$r = k[\mathrm{X}]^n \tag{2.1}$$

$$k = A \exp\left(-\frac{\Delta E}{RT}\right) \tag{2.2}$$

where [X] shows the concentration of reactant X and R is the ideal gas constant.

The interpretation of the term $A[\mathrm{X}]^n$ is that it represents the probability of molecule collisions which cause the reaction and that of the term $\exp(-\Delta E/RT)$ is that the proportion of the collisions which excess the activation energy of the reaction. Therefore, by comparing the values of $A[\mathrm{X}]^n$ and $\exp(-\Delta E/RT)$, the reaction activity can be estimated.

As discussed in Section 2.1, the concept of mixing fuel is aiming at utilizing the differences of reaction heat and reaction activity. In this point of view, the combination of hydrocarbons,

such as methane or propane, or dimethyl ether and ammonia can be a suitable option. Although alcohols such as methanol and ethanol have a larger reaction activity and methanol has a relatively small endothermic nature, their suitable temperature for reforming is relatively low compared to the hydrocarbons or ammonia, which makes it difficult to simply mix them as a fuel.

Table 2.1 Steam reforming characteristics of hydrogen carriers.

Reactants	ΔH^0_{298} [kJ mol^{-1}]	Reforming temperature [°C]	A [−]	ΔE [kJ mol^{-1}]	The power of fuel n_1	The power of water n_2
CH_4	206	600–800	1.42E+03	1.56E+05	1.29	-0.53
C_3H_8	497	600–800	7.90E+10	1.12E+05	1	−
CH_3OH	49	250–350	7.29E+03	7.97E+04	0.11	-0.17
C_2H_5OH	173	250–350	4.39E+02	2.30E+04	0.711	2.71
CH_3OCH_3	124	300–400	1.46E+10	1.98E+05	1.19	-0.73
NH_3	46	600–800	9.84E+01	1.20E+05	0.69	−

2.3 Combination of Methane and Ammonia

Among several conceivable combinations of mixing fuels as discussed in the previous section, we adopt the combination of methane and ammonia. This is because two fuels are quite common and have been well studied as a fuel for SOFCs [1–3,20–22].

When the methane–ammonia mixed fuel is supplied to Ni–YSZ anode of SOFCs, it is expected that the ammonia decomposition reaction selectively proceeds when the concentration of ammonia in the fuel is large. As ammonia is consumed through passing the catalyst, the steam methane reforming reaction gradually becomes active. If this is the case, since the endothermic heat of ammonia decomposition is small and that of steam methane reforming is large, the temperature distribution of the catalyst can be controlled by changing the mixing composition in the mixed fuel.

2.4 Reactions on Ni–YSZ Catalyst

2.4.1 Reactions to be Considered

The overall reactions of steam methane reforming and ammonia decomposition are described by Eq. (2.3) and Eq. (2.4), respectively.

$$CH_4 + H_2O \rightarrow CO + 3H_2 \qquad \Delta H^0{}_{298} = 206 \text{ kJ/mol} \tag{2.3}$$

$$NH_3 \rightarrow \frac{1}{2}N_2 + \frac{3}{2}H_2 \qquad \Delta H^0{}_{298} = 46 \text{ kJ/mol} \tag{2.4}$$

When these reactions proceed on the surface of nickel in Ni–YSZ catalyst, each of them is composed of several elementary reactions. The kinetics for both steam methane reforming and ammonia decomposition on various catalysts such as nickel and iron have been intensively studied and several kinds of elementary reaction models have been constructed [42–46]. These elementary reactions on the surface can be categorized either in the following three steps: adsorption, associative reaction, or desorption. When the mixed fuel is supplied, since two fuels are exposed to the competitive adsorption condition, it is important to consider the adsorption phenomena in the reaction model.

2.4.2 Adsorptions

When one fuel is supplied to a catalyst, it is adsorbed on the surface of the catalyst based on its adsorption characteristic. When the adsorption phenomena on the surface can be regarded as equilibrium, the adsorption constant is the value to describe the adsorption activity. The proportion of the active sites on the surface that are covered by the adsorbed molecules is expressed by coverage.

2.4.2.1 Sequential Adsorption Reactions

When methane is supplied to Ni–YSZ catalyst, the adsorption of methane on the nickel surface, which is described by Eq. (2.5), is composed of four sequential reactions, shown from Eq. (2.6) to Eq. (2.9).

$$CH_4 + 4V \leftrightarrow CH_{4ad} \quad (2.5)$$

$$CH_4 + V \rightarrow CH_{3ad} + H_{ad} \quad (2.6)$$

$$CH_3 + V \rightarrow CH_{2ad} + H_{ad} \quad (2.7)$$

$$CH_2 + V \rightarrow CH_{ad} + H_{ad} \quad (2.8)$$

$$CH + V \rightarrow C_{ad} + H_{ad} \quad (2.9)$$

where V shows a vacant site of the adsorption on the surface [47,48].

Once the elementary reactions, such as Eq. (2.6) to Eq. (2.9), are considered, it is necessary to consider all elementary reactions to construct the reaction model. As a result, the reaction rate estimation on the basis of the constructed model also requires the consideration of the elementary reaction systems. Contrary to this, if the adsorption phenomena are represented by Eq. (2.5) as an overall adsorption reaction, it is possible to regard CH_{4ad} as a reactant in the reforming reaction, thus, the reaction model can be simpler and more practical.

2.4.2.2 Competitive Adsorption Conditions

When the mixed fuel of methane and ammonia is supplied to Ni–YSZ catalyst, two fuels are competitively adsorbed depending on the magnitude of their adsorption constants [49]. The coverage of each species on the surface is determined by the relationship of all adsorption constants and concentrations of the component gases, namely methane, ammonia, steam, carbon monoxide, carbon dioxide, hydrogen, and nitrogen. As the reactions proceed, the concentrations of methane and ammonia in the mixed fuel change, so that the coverage of each

gas also changes, resulting in the change of the reaction rates of two fuels. Therefore, to describe the reactions of the mixed fuel, it is significant to introduce the idea of competitive adsorption by using the adsorption constants.

2.4.3 Associative Reactions

As mentioned in the previous section, one chemical reaction is usually composed of several elementary reactions. Each elementary reaction, however, does not always occur at the same rate, and the overall reaction rate is restricted by the slowest elementary reaction. This elementary reaction is called rate-determining reaction. It is known that the associative reaction on the surface is often rate-determining in the catalytic reaction process [48,50].

Since we adopted the model to handle the adsorption by an overall adsorption, as shown in Eq. (2.5), instead of the sequential elementary reactions, as shown from Eq. (2.6) to Eq. (2.9), it enables us to consider the associative reaction on the surface as one overall associative reaction, represented by Eq. (2.10).

$$CH_{4ad} + H_2O_{ad} \leftrightarrow 6H_{ad} + CO_{ad} \tag{2.10}$$

This assumption makes the model relatively simple and practical to introduce the reaction rates of steam methane reforming and ammonia decomposition under the competitive adsorption condition, as more detail is explained in Chapter 5.

2.4.4 Effect of YSZ on Reforming Reaction

It is reported that the catalyst support gives a large effect on the reaction rate of steam methane reforming. Depending on the material of the support, the power of steam concentration on the reforming rate is varied from –0.6 to 1 when the rate is expressed by the power-law type equation as shown in Eq. (2.1) [51]. This is interpreted as the steam adsorption on the support. Steam adsorbed on the active sites on the support, namely YSZ, affects the associative reaction

of steam methane reforming on nickel. In the case of single fuel of methane, the effect of steam adsorption on YSZ is automatically included in the reaction rate estimation. When the mixed fuel of methane and ammonia is supplied, however, the adsorption of the gases on the YSZ surface is changed because of ammonia and its decomposed gases. As a result, the reaction rate of steam methane reforming on nickel is affected.

2.5 Hydrogen Reuse in SOFCs

Fig. 2.1 shows the schematic picture of surface reaction of the mixed fuel on Ni–YSZ anode of SOFCs. Considering the difference of the activation energy of steam methane reforming and ammonia decomposition, it is expected that ammonia decomposition preferentially proceeds over steam methane reforming. If this is the case, when methane–ammonia mixed fuel is supplied to SOFCs, hydrogen is first produced from the decomposition of ammonia. This hydrogen is used as a fuel for the electrochemical reaction to generate electricity and, as a result, steam is produced. This steam can be used for steam methane reforming so that hydrogen is again produced and used for the electrochemical reaction. This indicates that the hydrogen atoms originally contained in ammonia can act twice as a fuel for the electrochemical reaction. The amount of steam supply can also be reduced. This is one more advantage that can be expected from mixing methane and ammonia. This study only covers the phenomena in the anode and does not include electrochemical reaction as SOFCs, therefore, further research is needed to clarify the water reuse effectiveness.

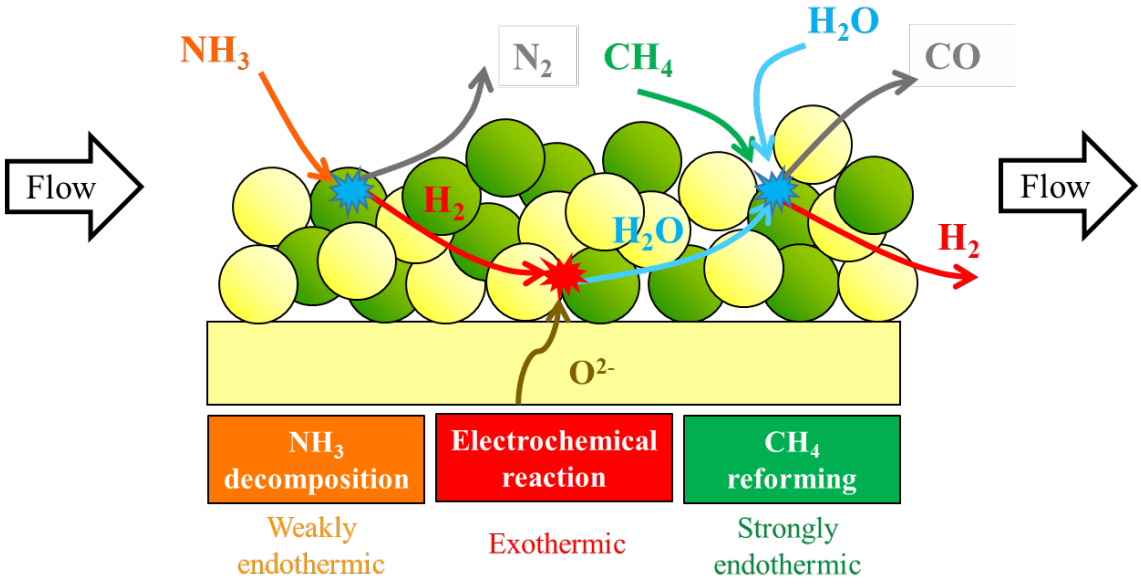

Fig. 2.1 Schematic picture of the reactions on a Ni–YSZ catalyst.

Bibliography

1. Achenbach E, Riensche E. Methane/steam reforming kinetics for solid oxide fuel cells. *J Power Sources*. 1994;52(2):283-288. doi:10.1016/0378-7753(94)02146-5
2. Achenbach E. Three-dimensional and time-dependent simulation of a planar solid oxide fuel cell stack. *J Power Sources*. 1994;49(1-3):333-348. doi:10.1016/0378-7753(93)01833-4
3. Laosiripojana N, Assabumrungrat S. Catalytic steam reforming of methane, methanol, and ethanol over Ni/YSZ: The possible use of these fuels in internal reforming SOFC. *J Power Sources*. 2007;163(2):943-951. doi:10.1016/j.jpowsour.2006.10.006
4. Lo Faro M, La Rosa D, Monforte G, Antonucci V, Arico AS, Antonucci P. Propane conversion over a Ru/CGO catalyst and its application in intermediate temperature solid oxide fuel cells. *J Appl Electrochem*. 2007;37(2):203-208. doi:10.1007/s10800-006-9245-5
5. Huang TJ, Wu CY, Wang CH. Fuel processing in direct propane solid oxide fuel cell and carbon dioxide reforming of propane over Ni–YSZ. *Fuel Process Technol*. 2011;92(8):1611-1616. doi:10.1016/j.fuproc.2011.04.007
6. Lo Faro M, La Rosa D, Frontera P, Antonucci P, Antonucci V, Aricò AS. Propane-fed solid oxide fuel cell based on a composite Ni–La–CGO anode catalyst. *Catal Letters*. 2010;136(1-2):57-64. doi:10.1007/s10562-010-0295-2
7. Jiang Y, Virkar A V. A High Performance, Anode-supported solid oxide fuel cell operating on direct alcohol. *J Electrochem Soc*. 2001;148(7):A706. doi:10.1149/1.1375166
8. Liu M, Peng R, Dong D, Gao J, Liu X, Meng G. Direct liquid methanol-fueled solid oxide fuel cell. *J Power Sources*. 2008;185(1):188-192.

doi:10.1016/j.jpowsour.2008.06.076

9. Lo Faro M, Stassi A, Antonucci V, et al. Direct utilization of methanol in solid oxide fuel cells: An electrochemical and catalytic study. *Int J Hydrogen Energy*. 2011;36(16):9977-9986. doi:10.1016/j.ijhydene.2011.05.053
10. Jordão B, Sarruf M, Hong J, Steinberger-wilckens R, Emílio P, Miranda V De. CeO_2–Co_3O_4–CuO anode for direct utilisation of methane or ethanol in solid oxide fuel cells. *Int J Hydrogen Energy*. 2018;43:6340-6351. doi:10.13140/RG.2.2.13804.46721
11. Hong-xin YOU, Guo-dong GAO, Liang Z, Abudula A. Power generating performances of ethanol on the SOFC. *J Fuel Chem Technol*. 2010;38(1):116-120. doi:10.1016/S1872-5813(10)60023-0
12. Steil MC, Nobrega SD, Georges S, Gelin P, Uhlenbruck S, Fonseca FC. Durable direct ethanol anode-supported solid oxide fuel cell. *Appl Energy*. 2017;199(1):180-186. doi:10.1016/j.apenergy.2017.04.086
13. Farrell B, Linic S. Direct electrochemical oxidation of ethanol on SOFCs: Improved carbon tolerance of Ni anode by alloying. *Appl Catal B Environ*. 2016;183:386-393. doi:10.1016/j.apcatb.2015.11.002
14. Murray EP, Harris SJ, Jen H. Solid oxide fuel cells utilizing dimethyl ether fuel. *J Electrochem Soc*. 2002;149(9):A1127. doi:10.1149/1.1496484
15. Liu Y, Guo Y, Wang W, et al. Study on proton-conducting solid oxide fuel cells with a conventional nickel cermet anode operating on dimethyl ether. *J Power Sources*. 2011;196(22):9246-9253. doi:10.1016/j.jpowsour.2011.07.051
16. Su C, Ran R, Wang W, Shao Z. Coke formation and performance of an intermediate-temperature solid oxide fuel cell operating on dimethyl ether fuel. *J Power Sources*. 2011;196(4):1967-1974. doi:10.1016/j.jpowsour.2010.10.011
17. Homel M, Gür TM, Koh JH, Virkar A V. Carbon monoxide-fueled solid oxide fuel

cell. *J Power Sources*. 2010;195(19):6367-6372. doi:10.1016/j.jpowsour.2010.04.020

18. Zhang H, Chen J, Zhang J. Performance analysis and parametric study of a solid oxide fuel cell fueled by carbon monoxide. *Int J Hydrogen Energy*. 2013;38(36):16354-16364. doi:10.1016/j.ijhydene.2013.09.144
19. Li C, Shi Y, Cai N. Carbon deposition on nickel cermet anodes of solid oxide fuel cells operating on carbon monoxide fuel. *J Power Sources*. 2013;225:1-8. doi:10.1016/j.jpowsour.2012.10.018
20. Wojcik A, Middleton H, Damopoulos I, Van Herle J. Ammonia as a fuel in solid oxide fuel cells. *J Power Sources*. 2003;118(1-2):342-348. doi:10.1016/S0378-7753(03)00083-1
21. Molouk AFS, Okanishi T, Muroyama H, Matsui T, Eguchi K. Electrochemical and catalytic behaviors of Ni–YSZ anode for the direct utilization of ammonia fuel in solid oxide fuel cells. *J Electrochem Soc*. 2015;162(10):F1268-F1274. doi:10.1149/2.1011510jes
22. Okanishi T, Okura K, Srifa A, et al. Comparative study of ammonia-fueled solid oxide fuel cell systems. *Fuel Cells*. 2017;17(3):383-390. doi:10.1002/fuce.201600165
23. Hoseinnia S, Sadeghzadeh SM. A comparative study of fuel cell technologies and their role in distributed generation. *Ieee Eurocon 2009, Eurocon 2009*. 2009:464-469. doi:10.1109/EURCON.2009.5167673
24. Blum L, Deja R, Peters R, Stolten D. Comparison of efficiencies of low, mean and high temperature fuel cell Systems. *Int J Hydrogen Energy*. 2011;36(17):11056-11067. doi:10.1016/j.ijhydene.2011.05.122
25. Shri Prakash B, Senthil Kumar S, Aruna ST. Properties and development of Ni/YSZ as an anode material in solid oxide fuel cell: A review. *Renew Sustain Energy Rev*. 2014;36:149-179. doi:10.1016/j.rser.2014.04.043

26. Shaikh SPS, Muchtar A, Somalu MR. A review on the selection of anode materials for solid-oxide fuel cells. *Renew Sustain Energy Rev*. 2015;51:1-8. doi:10.1016/j.rser.2015.05.069

27. Janardhanan VM, Heuveline V, Deutschmann O. Performance analysis of a SOFC under direct internal reforming conditions. *J Power Sources*. 2007;172(1):296-307. doi:10.1016/j.jpowsour.2007.07.008

28. Peters R, Dahl R, Klüttgen U, Palm C, Stolten D. Internal reforming of methane in solid oxide fuel cell systems. *J Power Sources*. 2002;106(1-2):238-244. doi:10.1016/S0378-7753(01)01039-4

29. Aguiar P, Adjiman CS, Brandon NP. Anode-supported intermediate temperature direct internal reforming solid oxide fuel cell. I: Model-based steady-state performance. *J Power Sources*. 2004;138(1-2):120-136. doi:10.1016/j.jpowsour.2004.06.040

30. Dicks AL. Advances in catalysts for internal reforming in high temperature fuel cells. *J Power Sources*. 1998;71(1-2):111-122. doi:10.1016/S0378-7753(97)02753-5

31. Iwai H, Yamamoto Y, Saito M, Yoshida H. Numerical simulation of intermediate-temperature direct-internal-reforming planar solid oxide fuel cell. *Energy*. 2011;36(4):2225-2234. doi:10.1016/j.energy.2010.03.058

32. Wongchanapai S, Iwai H, Saito M, Yoshida H. Selection of suitable operating conditions for planar anode-supported direct-internal-reforming solid-oxide fuel cell. *J Power Sources*. 2012;204:14-24. doi:10.1016/j.jpowsour.2011.12.029

33. Peters R, Riensche E, Cremer P. Pre-reforming of natural gas in solid oxide fuel-cell systems. *J Power Sources*. 2000;86(1):432-441. doi:10.1016/S0378-7753(99)00440-1

34. Ni M. Modeling of SOFC running on partially pre-reformed gas mixture. *Int J Hydrogen Energy*. 2012;37(2):1731-1745. doi:10.1016/j.ijhydene.2011.10.042

35. Andersson M, Nakajima H, Kitahara T, et al. Comparison of humidified hydrogen and

partly pre-reformed natural gas as fuel for solid oxide fuel cells applying computational fluid dynamics. *Int J Heat Mass Transf*. 2014;77:1008-1022. doi:10.1016/j.ijheatmasstransfer.2014.06.033

36. Boder M, Dittmeyer R. Catalytic modification of conventional SOFC anodes with a view to reducing their activity for direct internal reforming of natural gas. *J Power Sources*. 2006;155(1):13-22. doi:10.1016/j.jpowsour.2004.11.075
37. Teramoto K. Experimental estimation of reaction rate for steam reforming of dimethyl ether and methanol and its application for numerical simulation. *Master thesis, Grad School of Engineering, Dep Aeronautics and Astronautics, Kyoto Univ*. 2011.
38. Sugihara S, Kawamura Y, Iwai H. Formulation of steam-methane reforming rate in Ni–YSZ porous anode of solid oxide fuel cells. *Heat Mass Transf*. 2018;54(8):2497-2505. doi:10.1007/s00231-018-2299-1
39. Kishimoto M, Furukawa N, Kume T, Iwai H, Yoshida H. Formulation of ammonia decomposition rate in Ni–YSZ anode of solid oxide fuel cells. *Int J Hydrogen Energy*. 2017;42(4):2370-2380. doi:10.1016/j.ijhydene.2016.11.183
40. Ma L. Hydrogen Production from steam reforming of light hydrocarbons in an autothermic system. *Doctoral thesis, School of Chemical Engineering and Industrial Chemistry, University of New South Wales*. 1995.
41. Uskov SI, Enikeeva L V., Potemkin DI, et al. Kinetics of low-temperature steam reforming of propane in a methane excess on a Ni-based catalyst. *Catal Ind*. 2017;9(2):104-109. doi:10.1134/S2070050417020118
42. Bebelis S, Zeritis A, Tiropani C, Neophytides SG. Intrinsic kinetics of internal steam reforming of CH_4 over a Ni–YSZ–cermet catalyst-electrode. *Ind Eng Chem Res*. 2000;39(12):4920-4927.
43. Ahmed K, Foger K. Kinetics of internal steam reforming of methane on Ni/YSZ-based

anodes for solid oxide fuel cells. *Catal Today*. 2000;63(2-4):479-487. doi:10.1016/S0920-5861(00)00494-6

44. Wang Y, Yoshiba F, Kawase M, Watanabe T. Performance and effective kinetic models of methane steam reforming over Ni/YSZ anode of planar SOFC. *Int J Hydrogen Energy*. 2009;34(9):3885-3893. doi:10.1016/j.ijhydene.2009.02.073

45. Appari S, Janardhanan VM, Jayanti S, Maier L, Tischer S, Deutschmann O. Micro-kinetic modeling of NH_3 decomposition on Ni and its application to solid oxide fuel cells. *Chem Eng Sci*. 2011;66(21):5184-5191. doi:10.1016/j.ces.2011.07.007

46. Duan X, Qian G, Fan C, et al. First-principles calculations of ammonia decomposition on Ni(110) surface. *Surf Sci*. 2012;606(3-4):549-553. doi:10.1016/j.susc.2011.11.030

47. Blaylock DW, Ogura T, Green WH, Beran GJO. Computational investigation of thermochemistry and kinetics of steam methane reforming on Ni(111) under realistic conditions. *J Phys Chem C*. 2009;(113):4898-4908.

48. Xu J, Froment GF. Methane steam reforming, methanation and water–gas shift: I. Intrinsic kinetics. *AIChE J*. 1989;35(1):88-96. doi:10.1002/aic.690350109

49. Ihara M, Kusano T, Yokoyama C. Competitive adsorption reaction mechanism of Ni/Yttria-stabilized zirconia cermet anodes in H_2–H_2O solid oxide fuel cells. *J Electrochem Soc*. 2001;148(3). doi:10.1149/1.1345873

50. Wei J, Iglesia E. Isotopic and kinetic assessment of the mechanism of reactions of CH_4 with CO_2 or H_2O to form synthesis gas and carbon on nickel catalysts. *J Catal*. 2004;224(2):370-383. doi:10.1016/j.jcat.2004.02.032

51. Igarashi A. Recent topics on production and use of hydrogen. *J Hydrog Energy Syst Soc Japan*. 2000;25(2):62-70.

Chapter 3

Fundamental Characteristics of Methane–Ammonia Mixed Fuel Reforming on Ni–YSZ Catalysts

3.1 Introduction

In the previous chapter, the trade-off relationship between the efficient utilization of the excess heat and the prevention of the steep temperature drop near the inlet of the cell in solid oxide fuel cells (SOFCs) is discussed. The steep temperature drop also causes the decline of the hydrogen production by the reforming/decomposition because these reactions have a positive temperature dependency [1–5]. Therefore, the challenges which should be tackled by our new proposed method, namely mixing fuel, are summarized to the following three key factors: i) efficient utilization of the excess heat of electrochemical reaction, ii) moderate temperature distribution in the cell, and iii) high production rate of hydrogen.

As discussed, the combination of methane and ammonia is selected because of the large differences in their reaction activity and endothermic nature. If the mixed fuel enables us to delay the start of one (or more) reaction(s) by simply tuning the composition of the mixed fuel,

the trade-off relationship can be overcome and we may be able to accomplish the three key factors discussed above. So far, to the best of the authors' knowledge, not even basic data on the reactions of any mixed fuel of hydrogen carriers on the Ni–YSZ (yttria-stabilized zirconia) anodes of SOFCs with the aiming of controlling the reactions can be found in the literature, let alone the mixed fuel of methane and ammonia.

Therefore, in this chapter, we aim to experimentally clarify the characteristics of the reforming and decomposition reactions when methane–ammonia mixed fuel is supplied to a Ni–YSZ catalyst. The effects of the mixture compositions and the catalyst temperature on the conversion rates are investigated.

3.2 Experimental

In this chapter, the fundamental characteristics of the a porous Ni–YSZ catalyst, which is a typical anode material of SOFCs, are experimentally investigated. A small amount of the catalyst is packed in a thin quartz tube while maintaining its temperature at a desired value using an electric furnace. A mixture gas of methane, ammonia, steam, and balance argon is supplied to the Ni–YSZ catalysts varying the supply gas composition and temperature. The reaction rates of the steam methane reforming and ammonia decomposition are evaluated by measuring the exhaust gas composition.

3.2.1 Reforming/Decomposition Reactions

When humidified methane is supplied to a Ni-based catalysts, a steam methane reforming reaction, Eq. (3.1), and a water–gas shift reaction, Eq. (3.2), proceed as dominant reactions.

$$CH_4 + H_2O \rightarrow CO + 3H_2 \qquad \Delta H^0{}_{298} = 206 \text{ kJ/mol} \tag{3.1}$$

$$CO + H_2O \leftrightarrow CO_2 + H_2 \qquad \Delta H^0{}_{298} = -41 \text{ kJ/mol} \tag{3.2}$$

Steam methane reforming is a strongly endothermic reaction, which enables us to efficiently utilize the heat generated by the electrochemical reaction in the cell of SOFCs. On the other hand, it often causes an undesirable steep temperature drop near the inlet of the cell. Moreover, the steam reforming of methane fuel requires at least twice as much steam as methane.

The ammonia decomposition reaction can be expressed by the following Eq. (3.3).

$$NH_3 \rightarrow \frac{1}{2}N_2 + \frac{3}{2}H_2 \qquad \Delta H^0{}_{298} = 46 \text{ kJ/mol} \tag{3.3}$$

This is a weakly endothermic reaction and does not require a supply of steam, which is one of the advantages of using ammonia as a fuel for SOFCs compared with the reforming of hydrocarbons.

3.2.2 Catalyst Preparation

The reforming reactions of the mixed fuel are expected to occur on the anode of the SOFCs. To investigate the fundamental characteristics of the reforming reactions on the SOFC anode, crushed anode of an SOFC is employed as a reforming catalysts. A typical SOFC anode is a porous composite of Ni–YSZ (Ni:YSZ = 50:50 vol.%, 8 mol% Y_2O_3-ZrO_2). The Ni–YSZ catalyst was prepared as follows.

NiO powder (Wako Pure Chemical Industries, Ltd.), YSZ powder (Tosoh Co.) and carbon black (Asahi #15, Asahi Carbon Co., Ltd., 3.3 weight % to the total weight of NiO and YSZ) as a pore-forming agent were mixed and ball-milled for 2 hours with zirconia balls (φ=4.0 mm) and ethanol to disperse the powder particles. After the ball-milling, the ethanol was completely evaporated using a hot stirrer at approximately 130 °C. The resultant powder was die-pressed with a load of 64 MPa for 2 minutes to obtain a disk-shaped catalyst sample. The diameter of the disk and its thickness were approximately 30 and 3 mm, respectively. The disk was then sintered in a high temperature electric furnace at 1400 °C for 5 hours and crushed into granules. By sieving them with a mesh, the granules whose sizes were from 250 to 500 μm were screened and used as a catalyst. The catalyst after the sieving process is shown in Fig. 3.1. The granules are green because the nickel in the granules exists as NiO. The NiO should be reduced to Ni before the reforming experiments to function as a reforming catalyst. The NiO in the catalyst was reduced by supplying hydrogen at 800 °C. The catalyst granules were dark gray.

3.2.3 Test Section

Fig. 3.2 shows a picture of the test section. The crushed Ni–YSZ catalyst (0.3 g) was packed in a thin quartz tube whose inner diameter was 7.0 mm. Quartz wool was used to hold the Ni-YSZ at the set position. The streamwise length of the catalyst was approximately 3 mm.

Fig. 3.1 Crushed NiO-YSZ catalyst before the reduction process.

Fig. 3.2 Test section.

3.2.4 Experimental Apparatus

A schematic view of the experimental apparatus, which can be divided into three parts, is shown in Fig. 3.3. The first part is the gas supply system. Methane, ammonia, argon and hydrogen are supplied by mass flow controllers to precisely control their flow rates. Note that hydrogen is supplied only in the reduction process of the catalyst at the beginning of the experiments. Steam is supplied by passing methane and argon through a bubbler. The bubbler

temperature is controlled using a constant-temperature water bath. The gas-containing steam is heated by ribbon heaters to prevent the condensation of the steam inside the supply pipe. The supply pipe for ammonia is also heated near the test section to avoid its functioning as a cooling fin. The second part of the apparatus is the test section. A thin quartz tube containing the catalyst is placed in an electric furnace. A thermocouple is attached on the quartz tube close to the catalyst, and the power of the electric furnace is automatically controlled to set the temperature of the test section. The last part of the apparatus is the gas analyzing system. After passing through the test section, the mixture gas composition should be different from that of the supplied gas depending on the degree of the reforming reactions. It firstly passes through a sulfuric acid trap where the remaining ammonia is removed. Then the steam is removed by the following cold trap. After removing ammonia and steam, the exhaust gas composition is measured by a gas chromatograph (GC-8A, Shimadzu Co.) to evaluate the conversion rates of methane and ammonia. The flow rate of the exhaust gas is measured using a film flow meter.

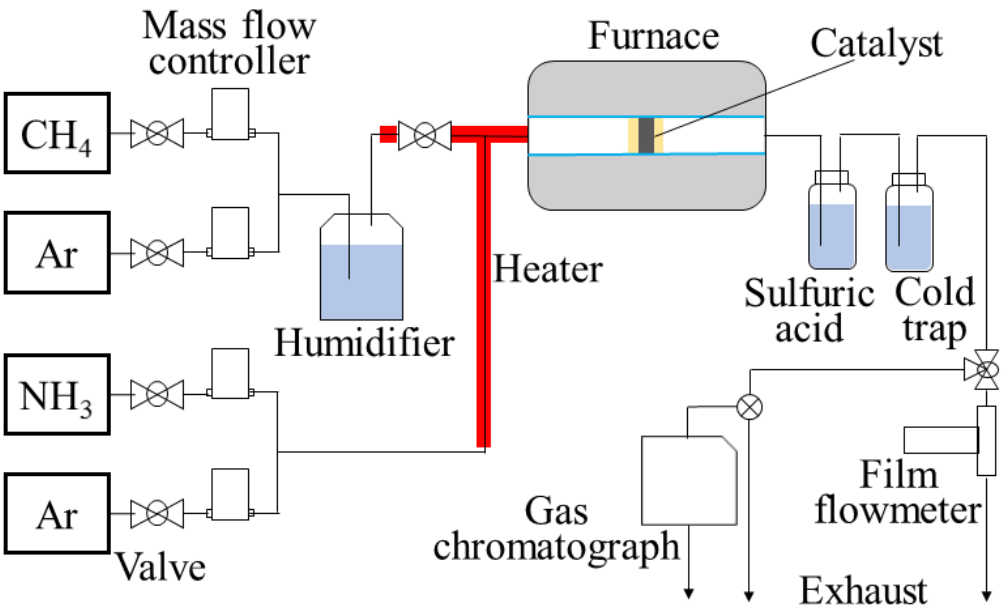

Fig. 3.3 Experimental setup for the reforming/decomposition experiments.

3.2.5 Reforming and Decomposition Rates

The reaction rates of the steam methane reforming and ammonia decomposition are calculated from the inlet/outlet gas compositions as follows:

$$\mathrm{CH_4\ reforming\ rate} = \left(\frac{\Delta VF_{\mathrm{CH_4}}}{VF_{\mathrm{CH_4,\ in}}}\right) \times 100 = \left(1 - \frac{VF_{\mathrm{CH_4,\ out}}}{VF_{\mathrm{CH_4,\ in}}}\right) \times 100\ [\%] \tag{3.4}$$

$$\mathrm{NH_3\ decomposition\ rate} = \left(\frac{\Delta VF_{\mathrm{NH_3}}}{VF_{\mathrm{NH_3,\ in}}}\right) \times 100 = \left(1 - \frac{2VF_{\mathrm{N_2,\ out}}}{VF_{\mathrm{NH_3,\ in}}}\right) \times 100\ [\%] \tag{3.5}$$

where $VF_{\mathrm{CH4,in}}$ and $VF_{\mathrm{NH3,in}}$ are the volumetric flow rates of methane and ammonia at the inlet, respectively. They are precisely controlled by the mass flow controllers. $VF_{\mathrm{CH4,out}}$ and $VF_{\mathrm{N2,out}}$ are those of methane and nitrogen at the outlet measured by gas chromatography, respectively. The amount of converted ammonia is calculated from the nitrogen production because $VF_{\mathrm{NH3,out}}$ cannot be measured since the remaining ammonia is completely removed at the sulfuric acid trap. Note that the volume flow rates are all evaluated under the standard condition.

3.2.6 Experimental Conditions

The effects of the inlet gas composition and reaction temperature on the reforming characteristics are investigated in this chapter. The inlet gas composition and furnace temperature are varied while keeping the total gas flow rate at the inlet constant. It is set at 360 ml/min under the standard condition (sccm: standard cubic centimeters per minute). The experimental conditions are summarized in Table 3.1. X_j in the table denotes the mole fraction of species j. Note that the balance argon is not listed in the table for the sake of visibility.

When methane is supplied to the catalyst, a certain amount of steam should be mixed for two reasons. The first reason is that the steam is needed for the methane reforming reaction. The other reason is to prevent carbon formation on the catalyst. Precise control of the steam flow rate is generally difficult, particularly when the flow rate is small, such as in this study.

To achieve a reliable supply of steam, the bubbler temperature and gas flow supplied to the bubbler were kept constant throughout the experiments, resulting in a constant steam flow rate of 100 ml/min, which corresponds to X_{H2O}=0.28. The maximum flow rate of methane was set at 60 ml/min so that the steam-to-carbon ratio, S/C, was higher than 1.7 to avoid the carbon formation problem. The furnace temperature was varied in the range from 600 to 750 °C.

Fig. 3.4 shows the equilibrium gas compositions calculated in the temperature range from 100 to 800 °C under typical inlet gas compositions set in this study. The calculation was done by CHEMKIN, a commercial software package. The figure shows that methane or ammonia contained in the inlet gas is almost fully converted in the temperature range set in this study when the gas reaches its equilibrium state.

Table 3.1 Experimental conditions.

Case	Furnace Temperature [°C $^{-1}$]	Mole fraction			S/C
		X_{CH4}	X_{H2O}	X_{NH3}	
X_{CH4}=0	600 / 650 / 700 /750	-	-	0.011 / 0.017 / 0.022 / 0.028 / 0.042 / 0.056 / 0.083 / 0.11 / 0.17	-
X_{CH4}=0056		0.056	0.28	0 / 0.011 / 0.017 / 0.022 / 0.028 / 0.042 / 0.056 / 0.083 / 0.11 / 0.17	5.0
X_{CH4}=011		0.11	0.28	0 / 0.011 / 0.017 / 0.022 / 0.028 / 0.042 / 0.056 / 0.083 / 0.11 / 0.17	2.5
X_{CH4}=014		0.14	0.28	0 / 0.011 / 0.017 / 0.022 / 0.028 / 0.042 / 0.056 / 0.083 / 0.11 / 0.17	2.0
X_{CH4}=017		0.17	0.28	0 / 0.011 / 0.017 / 0.022 / 0.028 / 0.042 / 0.056 / 0.083 / 0.11 / 0.17	1.7

Balance argon is not shown in the table.

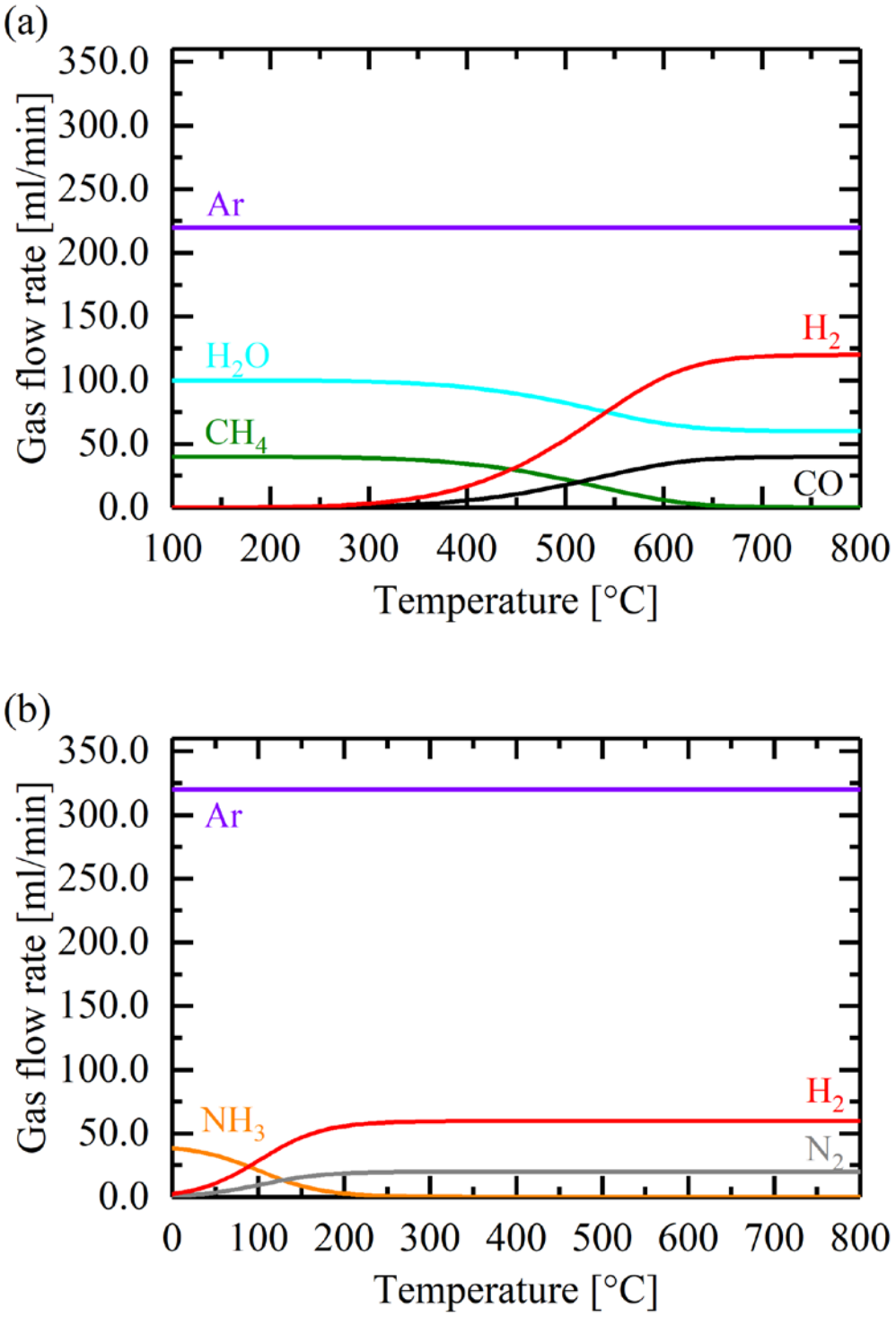

Fig. 3.4 Equilibrium gas composition calculated under typical inlet gas compositions.

(a) Steam methane reforming and (b) ammonia decomposition.

3.3 Results and Discussion

3.3.1 Reliability and Reproducibility

The ammonia decomposition may proceed as a gas phase reaction without the help of the catalyst at an elevated temperature. To clarify the characteristics of the catalytic reforming reactions, the gas phase decomposition of ammonia should be avoided in this study. Fig. 3.5 shows the results of a preliminary experiment on ammonia decomposition. This experiment was conducted without the Ni–YSZ catalyst. Only the quartz wool was packed in the quartz test tube, and diluted ammonia, whose composition was X_{NH3}=0.11, X_{Ar}=0.89, was supplied in the temperature range from 600 to 850 °C. The total flow rate was 360 ml/min. The figure shows that a small fraction of the ammonia is decomposed when the temperature is higher than 700 °C, implying the gas phase reaction of ammonia. It also shows that the gas phase reaction can be limited to less than 1% of the supplied ammonia if the temperature is set at 750 °C or less. The experimental conditions shown in Table 3.1 are determined on the basis of these results.

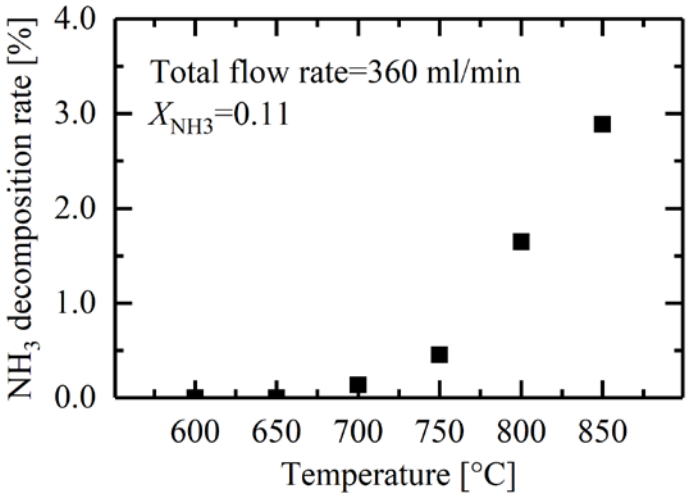

Fig. 3.5 Gas phase decomposition rate of ammonia.

The stability of the Ni–YSZ catalyst is also important for obtaining reliable experimental results. The Ni–YSZ catalyst (0.3 g) is packed in the test section, and a durability test is conducted by supplying a mixture gas of ammonia and argon at a constant flow rate at 700 °C. The supplied gas composition is the same as that in the previous experiment, that is, X_{NH3}=0.11, X_{Ar}=0.89. Fig. 3.6 shows the results of the durability test. A slight decrease in the reaction rate can be observed at the beginning of the experiment. After 90 minutes, the activity of the catalyst becomes stable, and the reaction rate is reasonably constant for approximately 20 hours, which is sufficiently long to conduct one series of the experiments in this study. Following this result, a waiting time of 90 minutes was set at the beginning of the experiments to ensure the stable activity of the catalysts. In addition, to further confirm that the obtained results are not affected by serious degradation of the catalyst, the reaction rate under a certain reference condition, i.e., ammonia flow rate of 40 ml/min with balance argon of 320 ml/min at 700 °C, is checked before and after the experiments. It was found that in all the experiments in this study, the difference in the reaction rate between before and after the experiment was less than 3.5%. This confirms the stability of the catalyst.

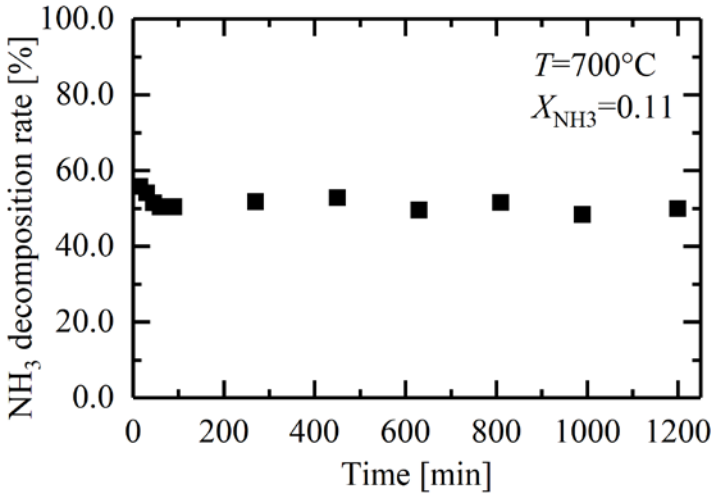

Fig. 3.6 Time variation of the NH_3 decomposition rate.

Fig. 3.7 confirms the reproducibility of the experimental results. The Ni–YSZ catalysts (0.3 g) prepared in different lots are packed in the test section, and their reaction activities are compared under the same experimental conditions. As shown in Fig. 3.7, the methane reforming rate and ammonia decomposition rate match each other well, which confirms the reproducibility of the experimental results.

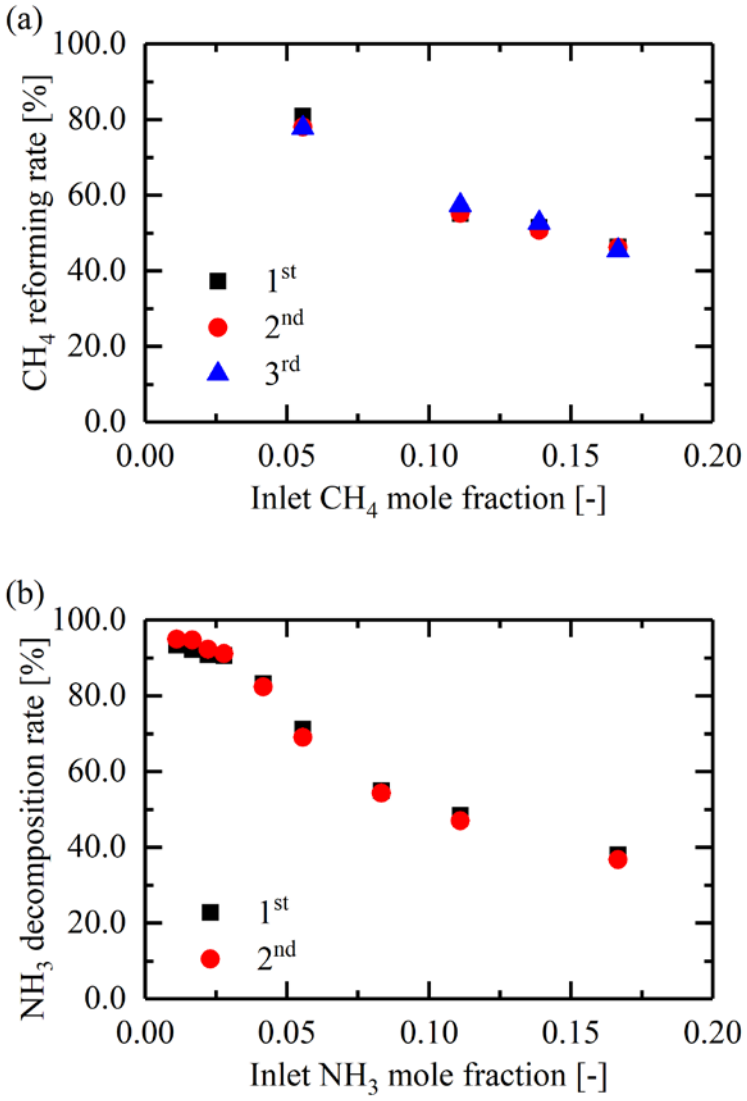

Fig. 3.7 Reproducibility of the experiments.
(a) Steam methane reforming and (b) ammonia decomposition.

3.3.2 Effect of Inlet Gas Composition

While keeping the total flow rate of the inlet gas at 360 ml/min, the inlet gas compositions are varied at constant temperatures of 600, 650, 700 and 750 °C as summarized in Table 3.1. Fig. 3.8 shows the amount of converted methane and the methane reforming rate at 600 °C., whereas the amount of converted ammonia and the ammonia decomposition rate at the same temperature are shown in Fig. 3.9.

When the mole fraction of ammonia at the inlet is zero, only the methane reforming reactions can occur in the test section. A certain amount of methane is consumed by the reforming reactions as shown in Fig. 3.8. When the mole fraction of methane at the inlet is low, the amount of methane consumed is naturally small whereas the reforming rate is high. The addition of ammonia to the inlet gas significantly affects the reforming reaction. The methane reforming reaction is suppressed and only the ammonia decomposition proceeds. Fig. 3.9 shows that the amount of converted ammonia and the ammonia decomposition rate are not affected by the methane concentration in the supplied gas. Note that CH_4=0 is the case when no methane is included in the inlet gas. The existence of methane in the inlet gas and the methane concentration have little effect on the ammonia decomposition reaction under this condition.

Similar characteristics can be observed even when the temperature is increased to 650 °C. Figs. 3.10 and 3.11 show the results at 650 °C corresponding to Figs. 3.8 and 3.9. In Fig. 3.10, the reaction rate of the methane reforming is clearly decreased by the addition of ammonia to the inlet gas. The suppression effect of ammonia on the methane reforming is significant. The methane reforming rate is close to zero when the ammonia mole fraction is higher than 0.042. A slight but clear difference from the results at 600 °C can be seen in Fig. 3.10. A small proportion of the supplied methane is reformed even when ammonia is added to the inlet gas

if the amount of added ammonia is small. The methane reforming reaction is not fully suppressed when the mole fraction of the inlet ammonia is less than 0.04. Under this condition, the methane reforming rate decreases with an increase in the ammonia mole fraction in the inlet gas. The methane reforming rate is higher for the case with a higher methane concentration if the inlet concentration of ammonia is the same. Another clear and interesting feature is found in the ammonia decomposition rate shown in Fig. 3.11. The ammonia decomposition rate is affected by the inlet methane concentration when the mole fraction of the inlet ammonia is less than 0.04. In this range, the ammonia decomposition rate decreases with an increase in the methane concentration.

Figs. 3.12 and 3.13 show the results at 700 °C corresponding to the previous figures. Even at this temperature, the suppression effects of the ammonia are clear. However, the methane reforming reaction is not fully suppressed, particularly when the inlet methane concentration is relatively high, as shown in Fig. 3.12. Fig. 3.13 shows that the effects of the methane concentration on the ammonia decomposition are more visible than those shown in the previous figure for 650 °C. The amount of converted ammonia decreases as the methane concentration increases. The effects of the methane addition on the ammonia decomposition can be more clearly observed in the ammonia decomposition rate. The ammonia decomposition rates are much lower than in the case of CH_4=0, under which only ammonia decomposition occurs.

The results at 750 °C are shown in Figs. 3.14 and 3.15. At this temperature, the methane reforming reaction occurs under all inlet gas conditions set in this study, although the reaction rate is lowered by the ammonia addition. The effects of the inlet methane concentration on the ammonia decomposition are even clearer than the previous figures for the relatively lower temperatures. Even the addition of a small amount of methane, X_{CH4}=0.056, to the ammonia fuel decreases the ammonia decomposition rate by 10%. The decrease in the ammonia decomposition rate is significant when the inlet ammonia concentration is relatively low,

X_{NH3}=0.011‑0.028. It is worth noting that the methane reforming reaction is relatively high under the same condition.

The results shown in Figs. 3.8 to 3.15 reveal some fundamental and important features of the reforming/decomposition reactions of the methane–ammonia mixed fuel on the Ni–YSZ catalyst. The methane reforming reaction is suppressed when ammonia is added to the fuel. This effect is more prominent at relatively low temperatures. At 600 °C, the methane reforming can be almost fully suppressed by ammonia addition. As the temperature increases, the suppression effect becomes milder. Both reactions occur simultaneously although both reaction rates are decreased if they are compared with the results for a pure methane reforming reaction or a pure ammonia decomposition reaction. A careful examination of the figures shows a competitive feature of the mixed fuel. The methane reforming reaction and the ammonia decomposition reaction show a trade-off relationship, implying that they share the same reaction sites on the catalyst and are competing for it. It is natural to assume that the main reaction sites are on the nickel surface. Kishimoto et al. [5] experimentally investigated the ammonia decomposition reaction on the Ni–YSZ catalyst and successfully formulated a reaction rate equation per unit area of Ni surface. A similar study was carried out by Sughihara et al [3] for the methane reforming reactions. Their successful formulations of the reaction rate equations per unit area of nickel support the assumption that the main reaction sites are on the nickel surface. It can be expected that this assumption can also be applied to build up a model for the reactions of the mixed fuel.

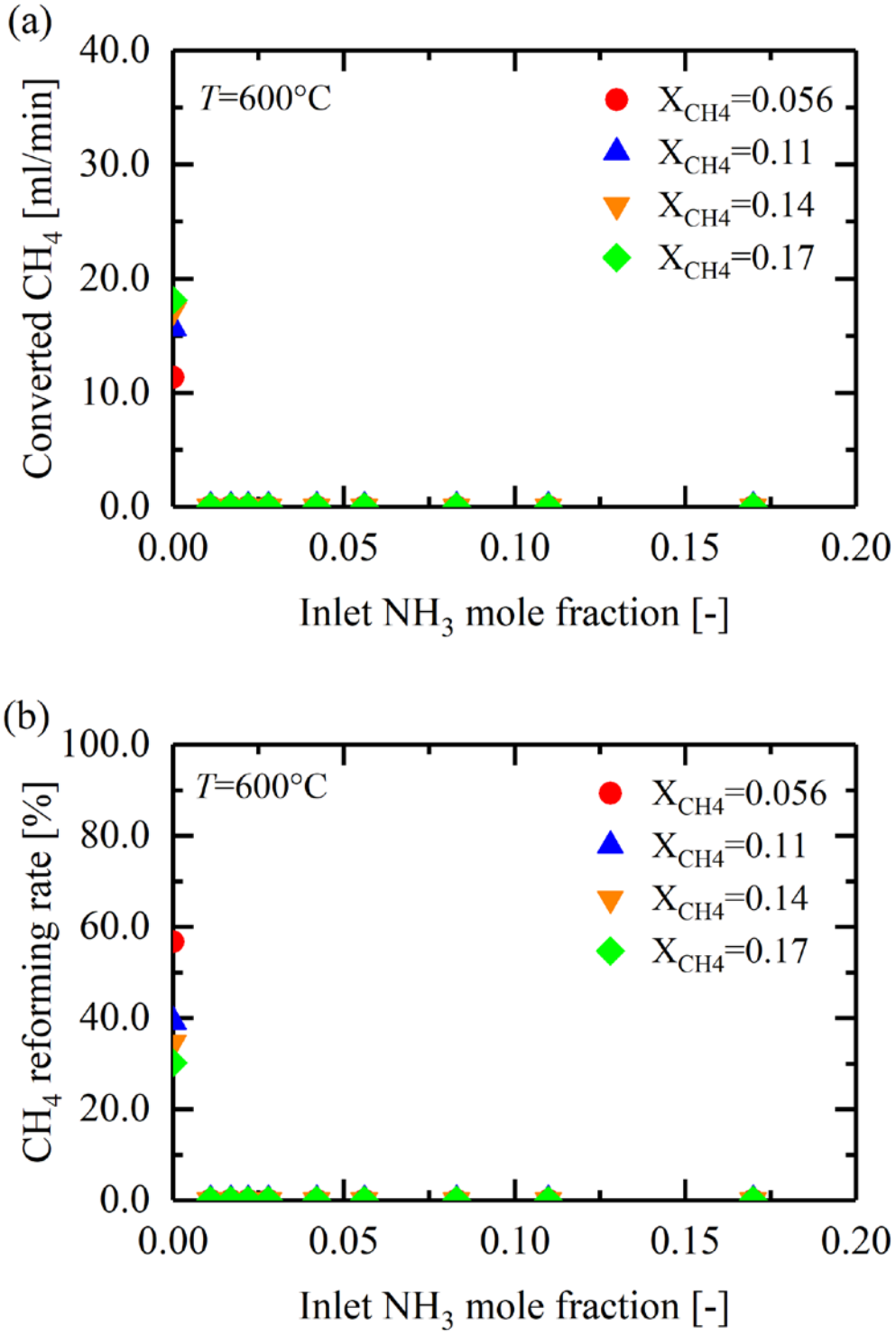

Fig. 3.8 Reaction characteristics of the methane reforming at 600 °C. (a) Converted methane and (b) methane reforming rate.

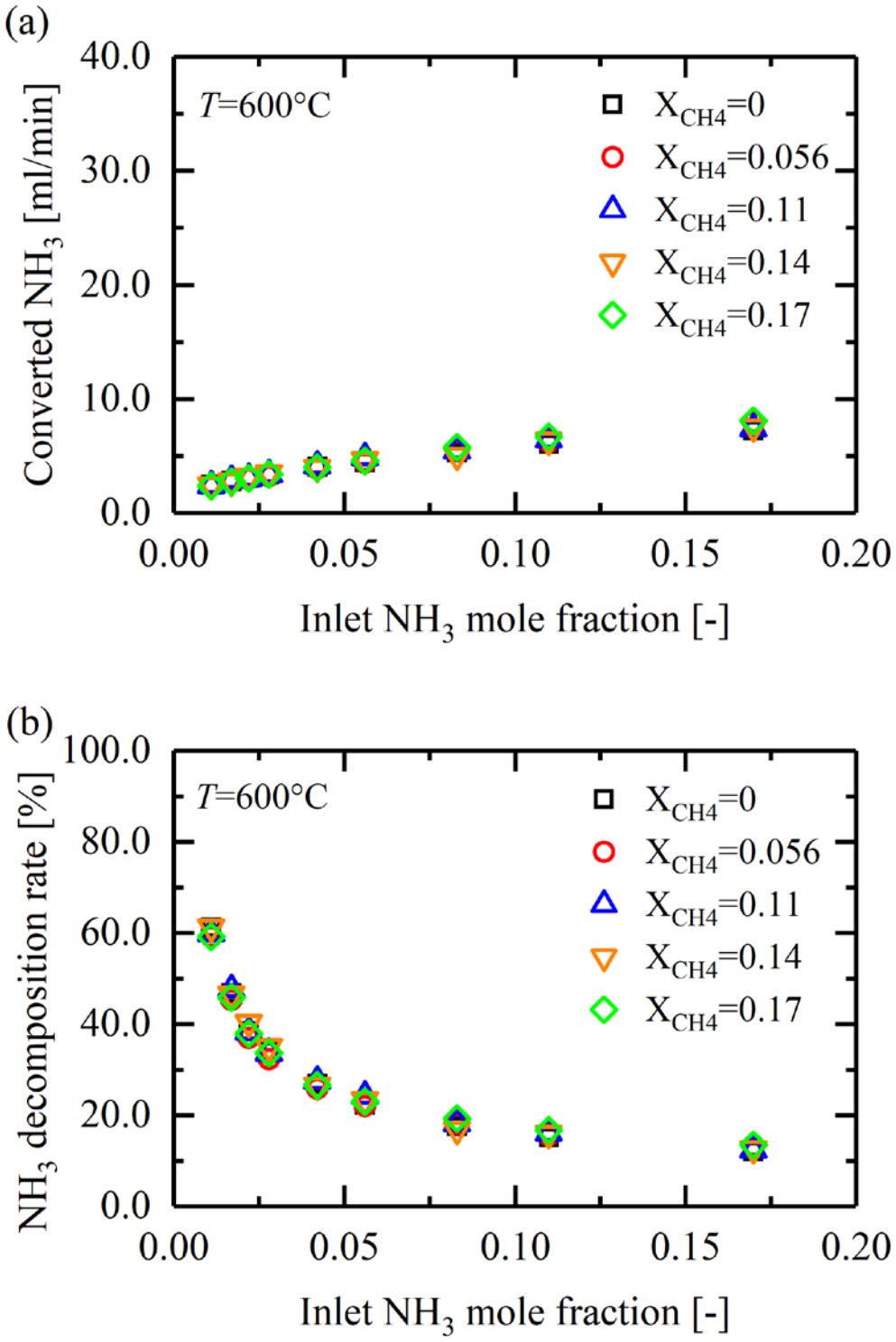

Fig. 3.9 Reaction characteristics of the ammonia decomposition at 600 °C.
(a) Converted ammonia and (b) ammonia decomposition rate.

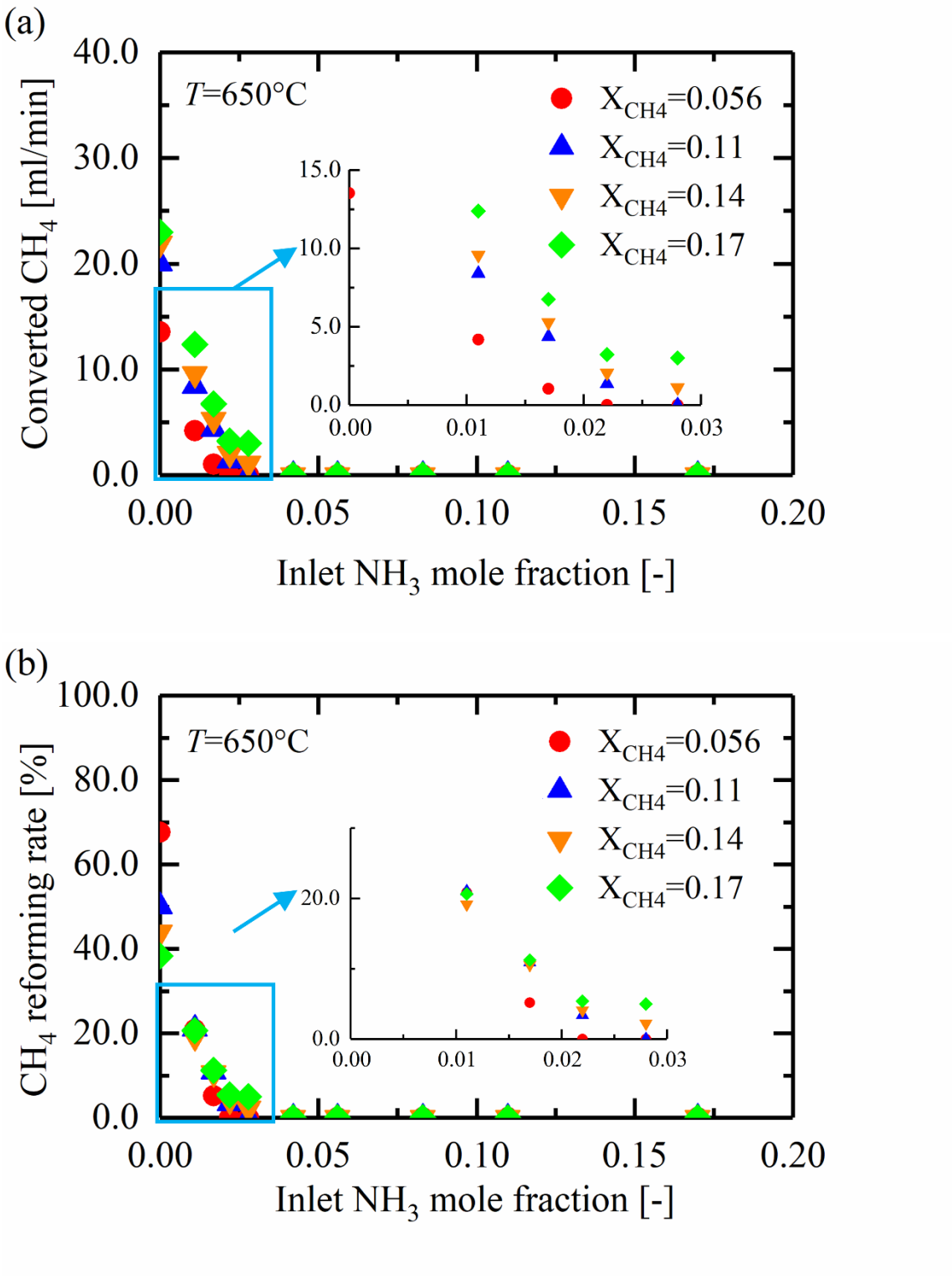

Fig. 3.10 Reaction characteristics of the methane reforming at 650 °C.
(a) Converted methane and (b) methane reforming rate.

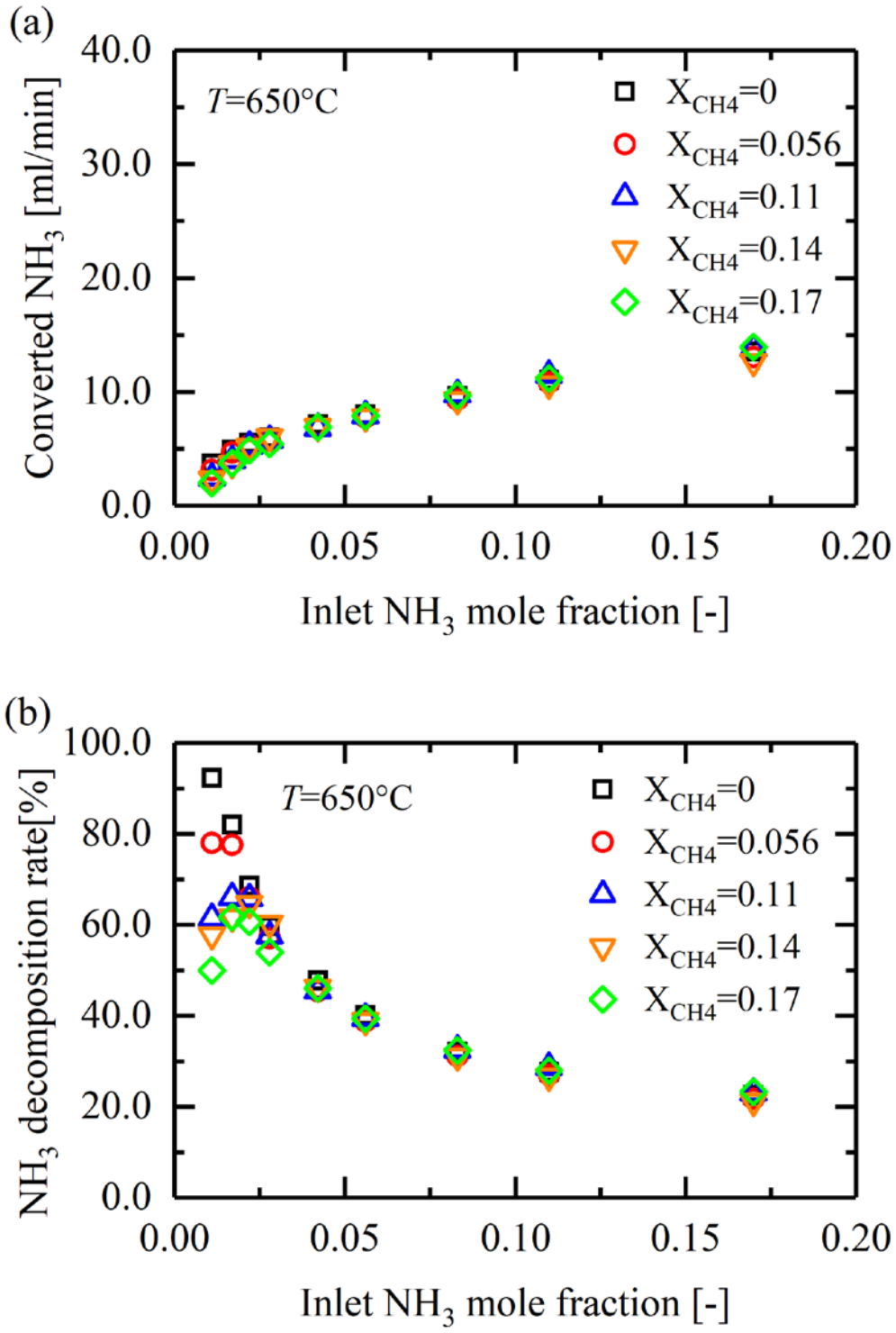

Fig. 3.11 Reaction characteristics of the ammonia decomposition at 650 °C. (a) Converted ammonia and (b) ammonia decomposition rate.

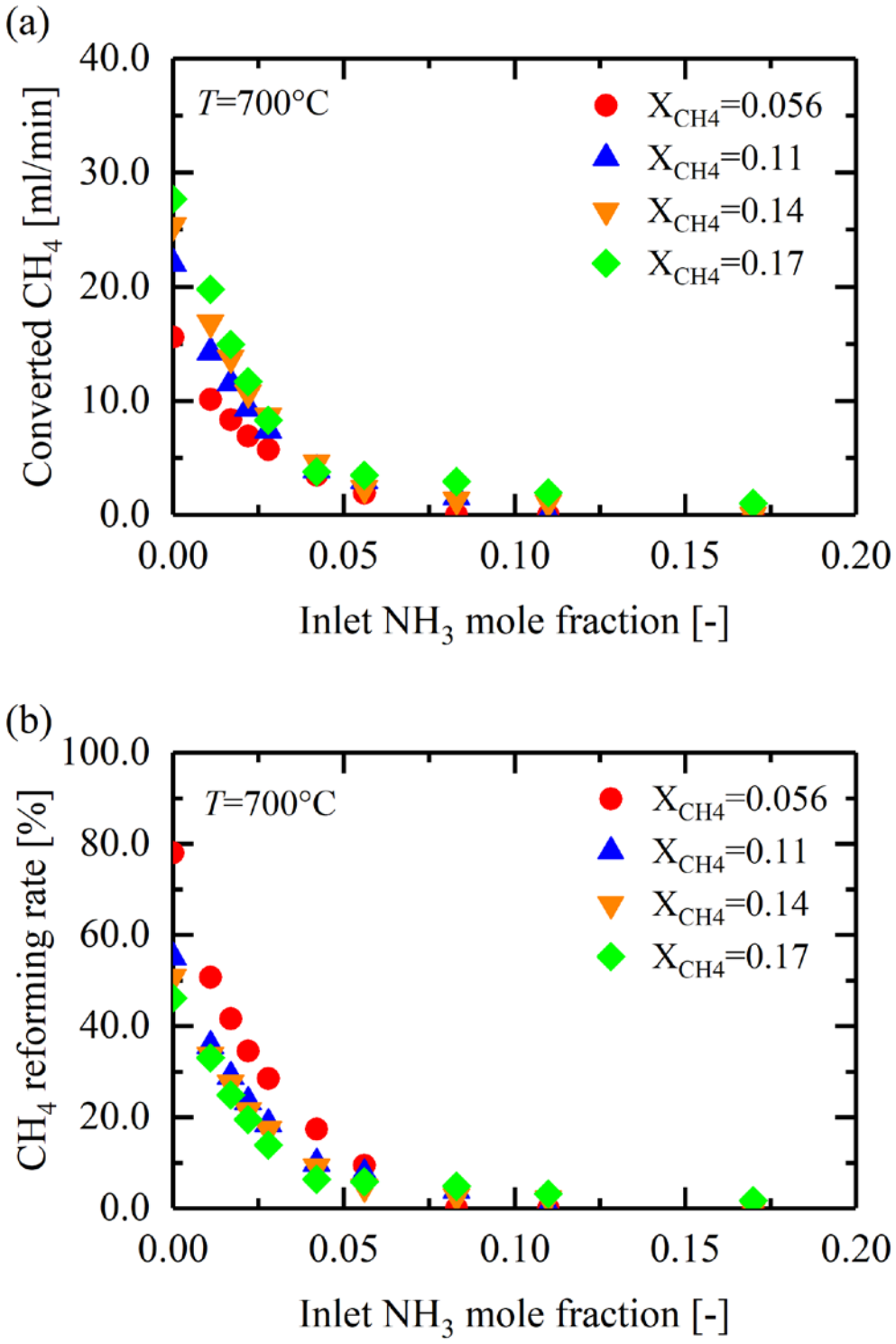

Fig. 3.12 Reaction characteristics of the methane reforming at 700 °C.
(a) Converted methane and (b) methane reforming rate.

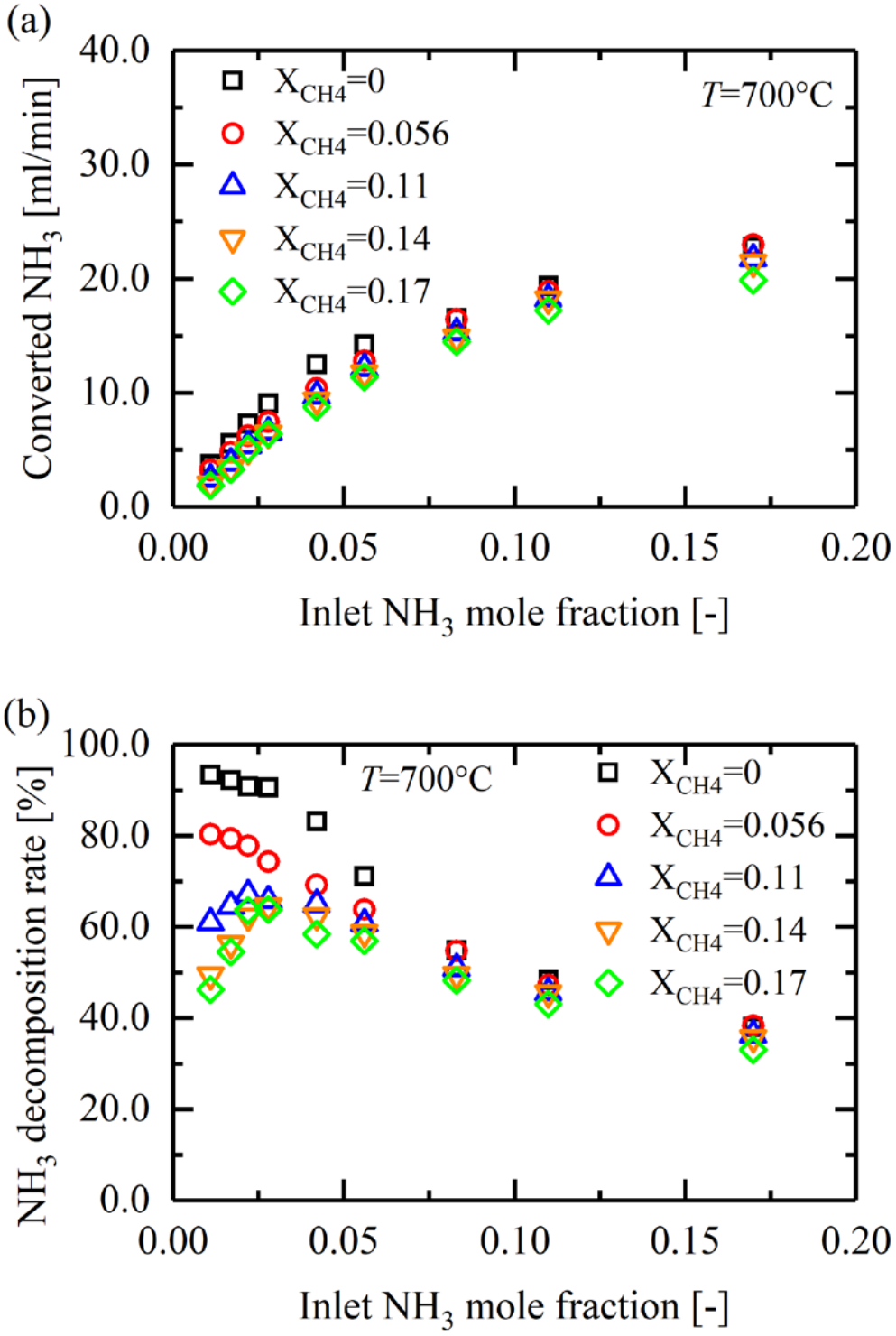

Fig. 3.13 Reaction characteristics of the ammonia decomposition at 700 °C. (a) Converted ammonia and (b) ammonia decomposition rate.

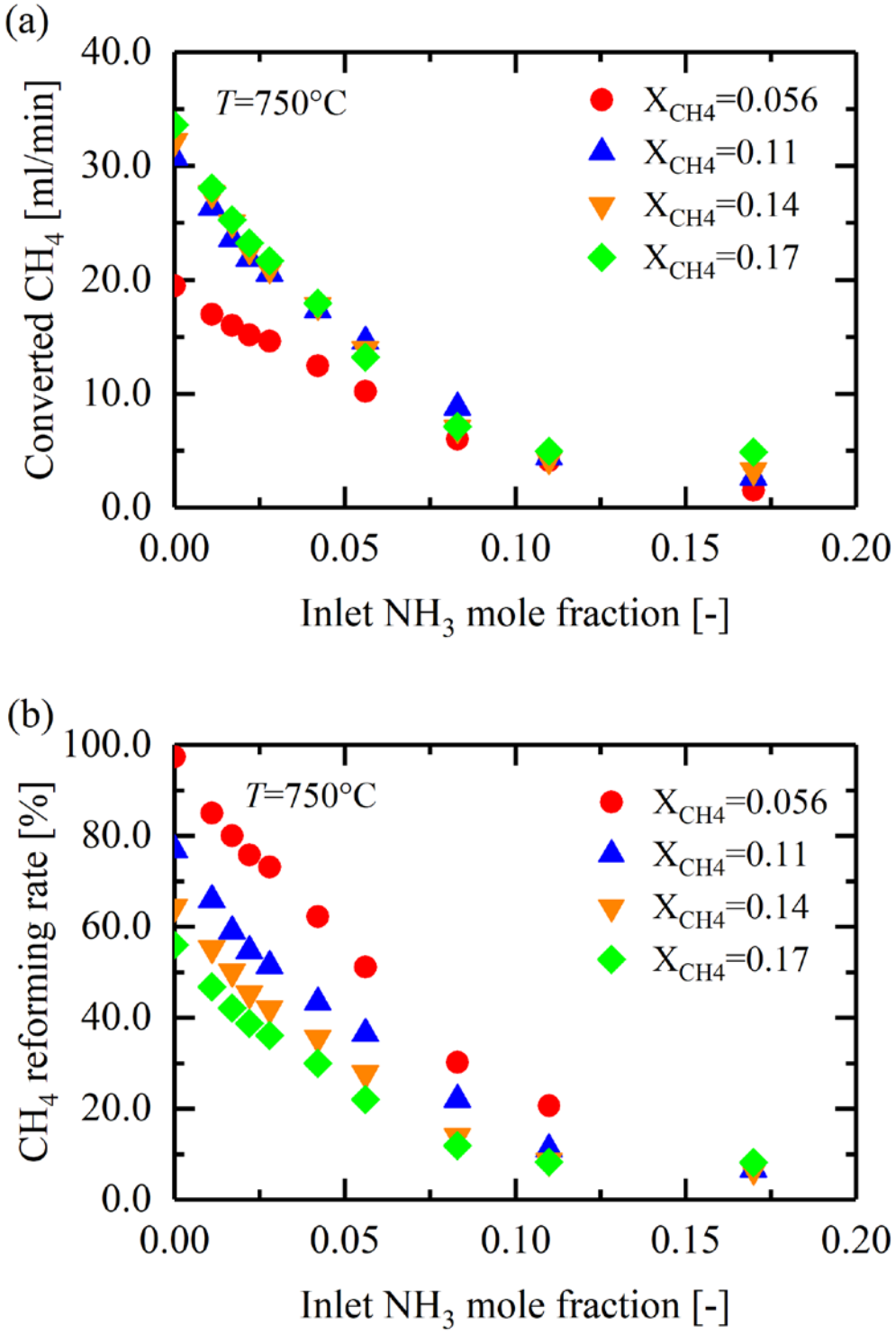

Fig. 3.14 Reaction characteristics of the methane reforming at 750 °C.
(a) Converted methane and (b) methane reforming rate.

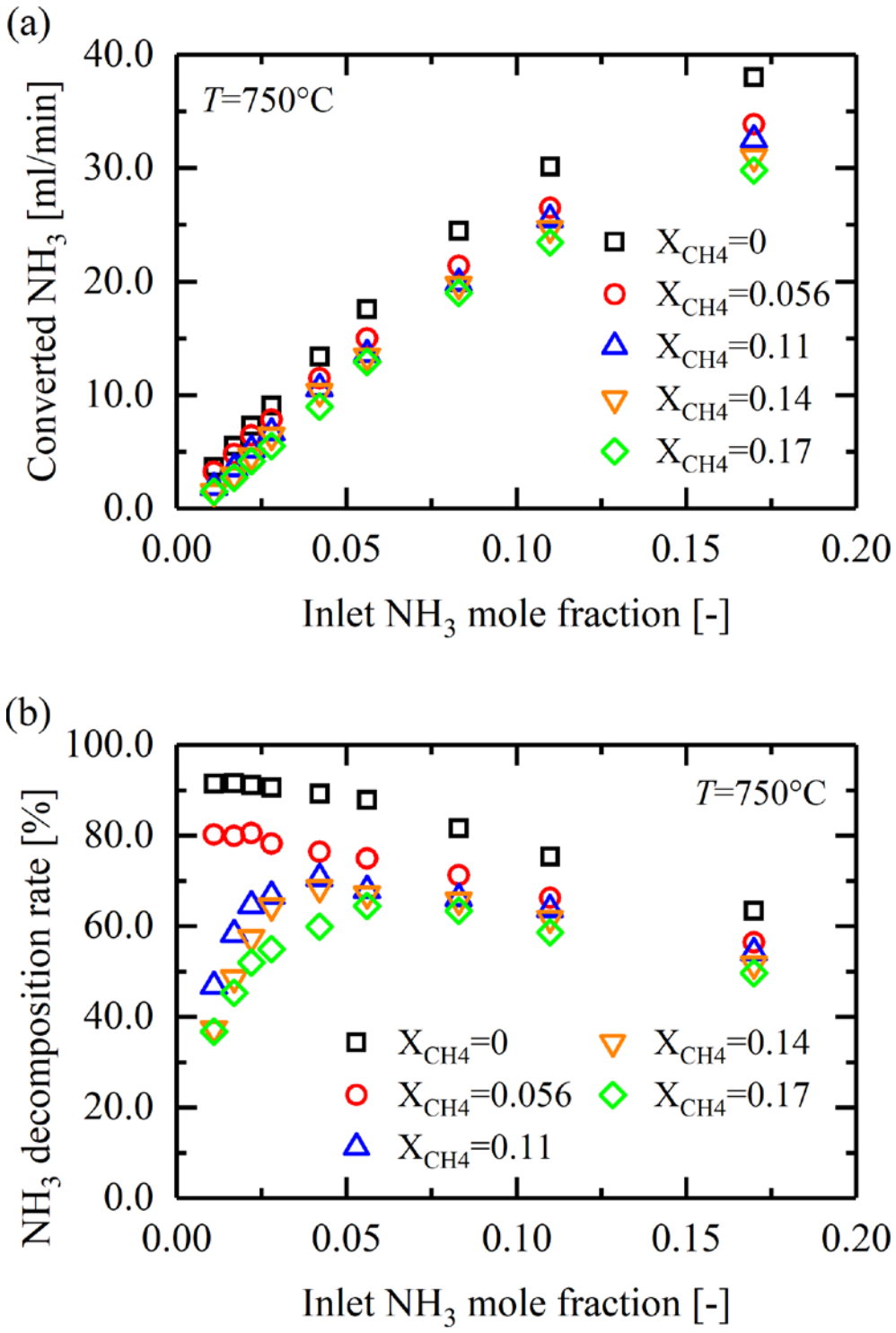

Fig. 3.15 Reaction characteristics of the ammonia decomposition at 750 °C. (a) Converted ammonia and (b) ammonia decomposition rate.

3.3.3 Effect of Temperature

Figs 3.16 and 3.17 show the results obtained at different temperatures. The total flow rate of the mixed gas was set at 360 ml/min. The inlet mole fractions of methane and steam were kept constant at X_{CH4}=0.11 and X_{H2O}=0.28, respectively. A higher mole fraction of ammonia indicates a lower concentration of balance argon. The amount of the converted methane and the methane reforming rate are shown in Fig. 3.16, whereas the amount of converted ammonia and the ammonia decomposition rate are plotted in Fig. 3.17.

In Fig. 3.16, the amount of converted methane is larger at a higher temperature when the composition of the supplied gas is the same. Its value decreases with an increase of the ammonia concentration in the supplied gas. There is a noticeable difference in its dependence on the temperature. The converted methane is more sensitive to the inlet ammonia concentration at a lower temperature, which can be confirmed from the slope of the curve. The decreasing (negative) slope is steeper at a lower temperature, implying that the suppression effects of the ammonia on the methane reforming reaction are more significant at a lower temperature and moderate at a higher temperature. In the case of the ammonia decomposition reaction shown in Fig. 3.17, on the other hand, a novel feature is observed in the decomposition rate. Although the ammonia decomposition rate generally appears to be higher at a higher temperature, its value drops under the conditions that the inlet ammonia concentration is low and the methane reforming reaction is relatively active. The decrease in the ammonia decomposition rate is more significant at a high temperature, implying that more of the reaction sites on the nickel surface are occupied by the species associated with the methane reforming reaction at higher temperatures.

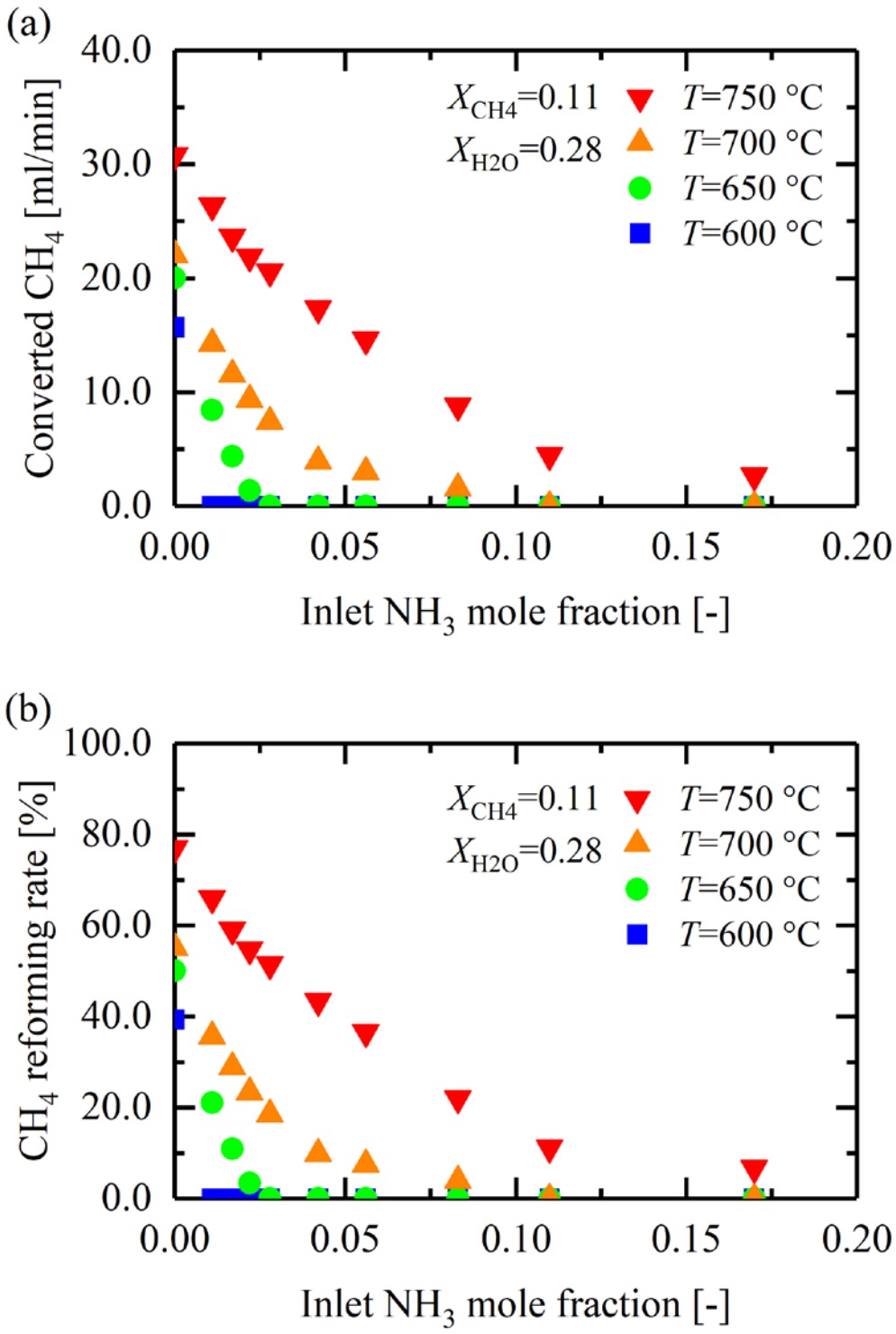

Fig. 3.16 Effect of temperature on the methane reforming.
(a) Converted methane and (b) methane reforming rate.

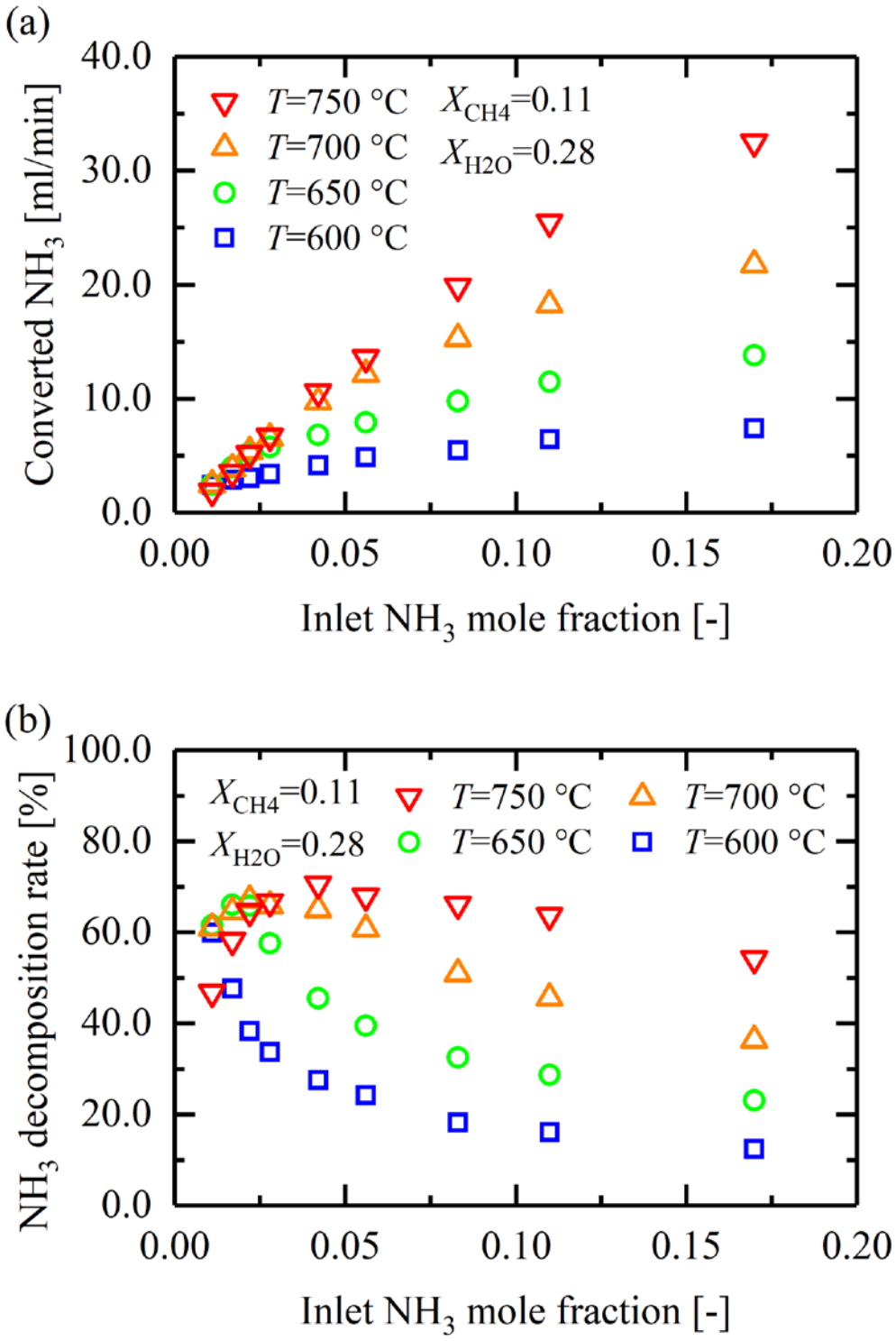

Fig. 3.17 Effect of temperature on the ammonia decomposition. (a) Converted ammonia and (b) ammonia decomposition rate.

3.4 Conclusions

The fundamental characteristics of the reforming and decomposition reactions of a methane–ammonia mixed fuel on a Ni–YSZ catalyst were experimentally investigated. The porous Ni–YSZ is a typical anode material of solid oxide fuel cells. A small amount of the crushed Ni–YSZ anode was packed in a thin quartz tube, and a mixture gas of methane, ammonia, steam and balance argon was supplied. The test section was placed in an electric furnace to control the catalyst temperature. The exhaust gas compositions were measured by gas chromatography varying the inlet gas composition and furnace temperature. The reaction rates of the steam methane reforming and ammonia decomposition are evaluated by measuring the exhaust gas compositions.

It was found that the steam methane reforming reaction was suppressed by adding ammonia to the fuel. This suppression effect was particularly significant at relatively low temperatures. The steam methane reforming was almost completely suppressed whereas the ammonia decomposition reaction was not affected by the methane in the fuel at 600 °C. The suppression effects became moderate at higher temperatures when the ammonia concentration was relatively low. Under the conditions in which the methane reforming was sufficiently active, the ammonia decomposition was suppressed. This trade-off of the two reactions shows that they share the same reaction sites on the catalyst and are competing with each other. The experimental results show that the ammonia decomposition generally preferentially occurs but the methane reforming becomes non-negligible at higher temperatures when the ammonia concentration is low.

Bibliography

1. Angeli SD, Monteleone G, Giaconia A, Lemonidou AA. State-of-the-art catalysts for CH_4 steam reforming at low temperature. *Int J Hydrogen Energy*. 2014;39:1979-1997. doi:10.1016/j.ijhydene.2013.12.001
2. Mogensen D, Grunwaldt JD, Hendriksen P V., Dam-Johansen K, Nielsen JU. Internal steam reforming in solid oxide fuel cells: Status and opportunities of kinetic studies and their impact on modelling. *J Power Sources*. 2011;196(1):25-38. doi:10.1016/j.jpowsour.2010.06.091
3. Sugihara S, Kawamura Y, Iwai H. Formulation of steam–methane reforming rate in Ni–YSZ porous anode of solid oxide fuel cells. *Heat Mass Transf*. 2018;54(8):2497-2505. doi:10.1007/s00231-018-2299-1
4. Chein R, Chen Y, Chang C, Chung JN. Numerical modeling of hydrogen production from ammonia decomposition for fuel cell applications. *Int J Hydrogen Energy*. 2010;35:589-597. doi:10.1016/j.ijhydene.2009.10.098
5. Kishimoto M, Furukawa N, Kume T, Iwai H, Yoshida H. Formulation of ammonia decomposition rate in Ni–YSZ anode of solid oxide fuel cells. *Int J Hydrogen Energy*. 2017;42(4):2370-2380. doi:10.1016/j.ijhydene.2016.11.183

Chapter 4

Effects of Mixed Fuel Reforming Reactions on Thermal Field of Ni-YSZ Anode of SOFCs

4.1 Introduction

In the previous chapters, the ideal fuel for the internal reforming of solid oxide fuel cells (SOFCs) has been discussed. High production rate of hydrogen, efficient utilization of the excess heat of electrochemical reaction, and moderate temperature distribution of the cell are the three key factors. Any kind of single fuel [1–9], however, cannot fully meet all these requirements because the efficient utilization of the excess heat, moderate temperature distribution in the cell, and high production rate of hydrogen are in trade-off relationship.

From the experimental results in Chapter 3, it is found that the ammonia decomposition reaction preferentially proceeds compared to the steam methane reforming on Ni–YSZ (yttria-stabilized zirconia) catalyst when the two fuels are simultaneously supplied. This fact provides us with an opportunity to delay the start of one (or more) reaction(s) by simply tuning the composition of the supplied mixture gas, thus, it may be possible to control the location and

magnitude of the endothermic reactions along the flow direction. The amount of excess heat utilization, on the other hand, should be determined by the overall reactions taking place in the cells. Therefore, the mixed fuel of methane and ammonia has a possibility of simultaneously achieving the high excess heat utilization and the suppression of the low-temperature region near the inlet in the direct reforming operation of SOFCs.

Therefore, in this chapter, we experimentally clarify the thermal field of Ni–YSZ catalysts, which represents the Ni–YSZ anode of SOFCs. The temperature distribution of the catalyst along the flow direction is measured at different mixture compositions to examine the possibility of controlling the local temperature of the cells. The efficiency of heat utilization and hydrogen production are also evaluated by measuring the exhausted gas compositions.

4.2 Experimental

In this chapter, thermal field of the catalyst along the flow direction is experimentally studied. The effect of the mixture composition in the mixed fuel on the temperature distribution of the catalyst is investigated to examine the possibility of controlling the local temperature of cells.

4.2.1 Reforming/Decomposition Reactions

When humidified methane is supplied to a Ni-based catalyst, a steam methane reforming reaction, Eq. (4.1), and a water–gas shift reaction, Eq. (4.2), proceed as dominant reactions.

$$CH_4 + H_2O \rightarrow CO + 3H_2 \qquad \Delta H^0_{298} = 206 \text{ kJ/mol} \tag{4.1}$$

$$CO + H_2O \leftrightarrow CO_2 + H_2 \qquad \Delta H^0_{298} = -41 \text{ kJ/mol} \tag{4.2}$$

The strongly endothermic nature allows us to efficiently utilize the heat generated by the electrochemical reaction in the cell of SOFCs. On the other hand, it causes an undesirable steep temperature drop near the inlet of the cell, resulting in the mechanical failure of the cell and decline of the reforming efficiency. Moreover, the steam reforming of methane fuel requires at least twice as much steam as methane.

The ammonia decomposition reaction can be expressed by the following Eq. (4.3).

$$NH_3 \rightarrow \frac{1}{2}N_2 + \frac{3}{2}H_2 \qquad \Delta H^0_{298} = 46 \text{ kJ/mol} \tag{4.3}$$

This is a weakly endothermic reaction and does not require a supply of steam, which are the advantages of using ammonia as a fuel for SOFCs compared with the reforming of hydrocarbons.

4.2.2 Catalyst Preparation

Ni–YSZ cermet (Ni:YSZ = 50:50 vol.%, 8 mol%Y_2O_3-ZrO_2) was used as a catalyst. NiO powder (Nickel (II) Oxide, Wako Pure Chemical Industries, Ltd.), YSZ powder (TOSOH-ZIRCONIA TZ-8Y, Tosoh Co.) were mixed with the addition of 3.3 wt% carbon black (Asahi #15, Asahi Carbon Co., Ltd.) as a pore–forming agent and ball-milled for 1 hour with zirconia balls and ethanol to disperse the particles. After milling, the ethanol was completely evaporated using a hot stirrer at approximately 130 °C. The resultant powder was uniaxially pressed in a die with a load of 64 MPa for 2 minutes to obtain a disk-shaped catalyst sample. The diameter and thickness of the disk were 30 mm and 3 mm, respectively. The disk was then sintered at 1400 °C for 5 hours and crushed into granules. By sieving with a mesh, the granules with a size ranging from 250 to 500 μm were screened and used as a catalyst. Note that NiO in the catalyst was reduced into Ni before the experiments. A mixture of nitrogen and hydrogen was supplied with a total flow rate of 100ml/min at a furnace temperature of 700 °C. The proportion of hydrogen in the mixture gas was set at 5% for the first 20 minutes and then increased to 10%. After that, the hydrogen concentration was increased by 10% every 5 minutes until it reached 100%. Finally, the catalyst was kept in pure hydrogen for 1 hour at 700 °C.

4.2.3 Experimental Setup

In the measurement of catalyst temperature distribution, 0.75 g and 1.5 g of the catalyst were packed to form lengths of 21 mm and 42 mm in the flow direction, respectively, as shown in Fig. 4.1 (a). The catalyst beds with sufficient lengths were employed to clearly observe the distribution of the local temperature.

Fig. 4.1 (b) shows a schematic picture of the gas supply system. A mixture gas of methane, steam, ammonia, and balance argon were supplied to the Ni–YSZ catalyst. The flow rates of

methane, ammonia, and balance argon were controlled by mass flow controllers. Steam was supplied by passing methane and argon through a bubbler. The concentration of steam was controlled to the desired values by changing the water bath temperature of the bubbler. The catalyst temperature was controlled by an electric furnace, whose temperature was monitored by a thermocouple attached to the quartz tube. The remaining ammonia and steam after the reforming reaction were eliminated respectively by a sulfuric acid trap and a cold trap. The flow rate of the exhaust gas was measured by a film flow meter. The exhaust gas concentration was measured by a gas chromatograph (GC-8A, Shimadzu Co.) to evaluate the reaction rates of methane and ammonia.

The electric furnace was slightly opened to measure the temperature distribution of the catalyst with an infrared (IR) camera (TVS-8500, NEC Avio). The IR camera was equipped with a 2-D InSb sensor with detection wavelength ranges of 3.4–4.1 μm and 4.5–5.1 μm. This enabled us to measure the surface temperature of the Ni–YSZ catalyst through the quartz tube. We performed a preliminary experiment to calibrate the IR camera. A K-type thermocouple was attached to the surface of a Ni–YSZ catalyst (not crushed) and the catalyst was placed in a quartz tube. Nitrogen was supplied to the catalyst so that no chemical reaction occurs. The surface temperature of the catalyst was measured by using both the attached thermocouple and the IR camera in a range of the furnace temperature from 600 to 750 °C. The emissivity of the Ni–YSZ surface assumed in IR imaging was used as a tuning parameter so that the output of the IR measurement can reproduce the temperature measured by the thermocouple. The emissivity was set at 0.98. The root-mean-square error of the IR measurements estimated on the basis of the thermocouple measurements is 0.5 K in the temperature range of this study.

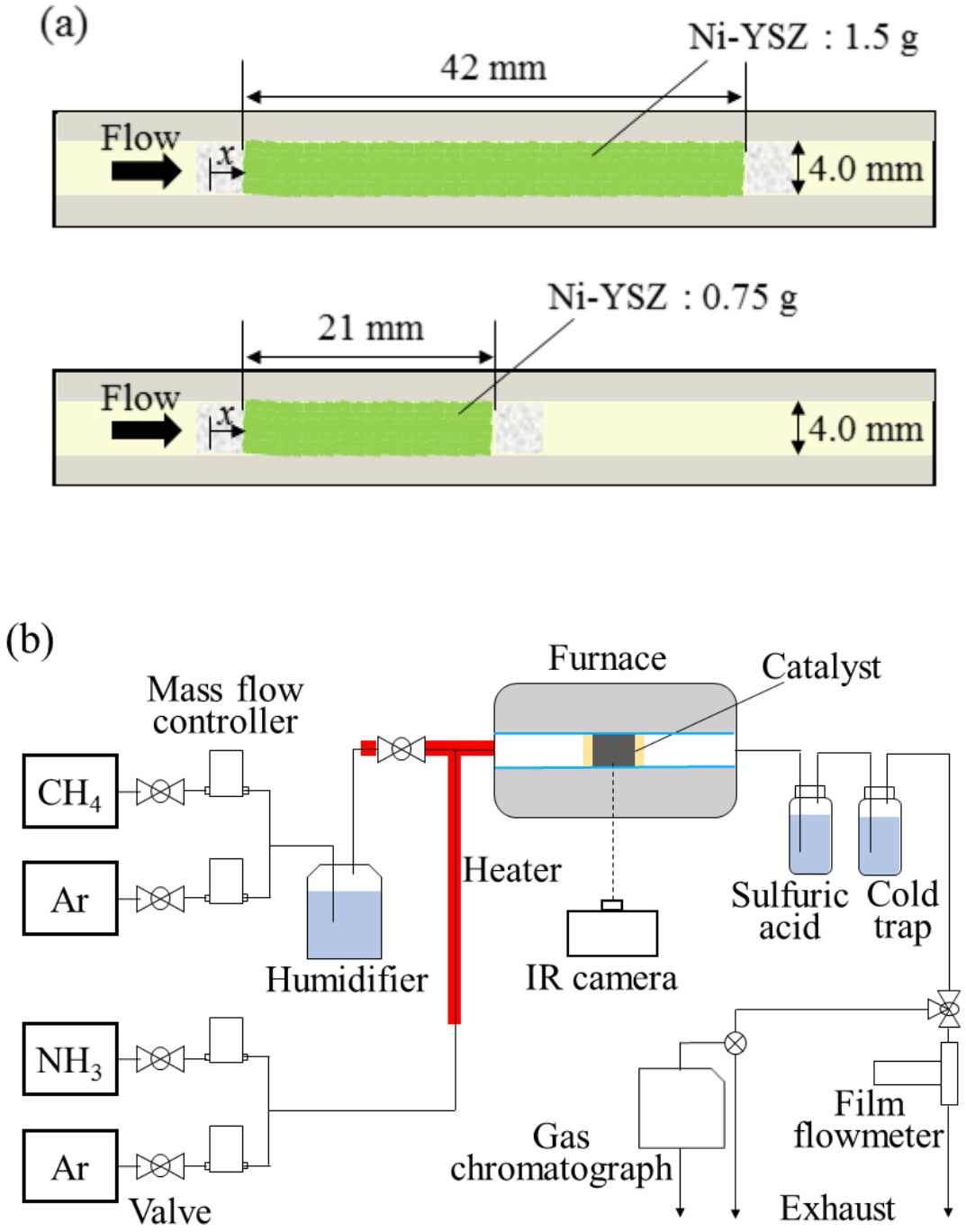

Fig. 4.1 Experimental setup. (a) Catalyst for the measurement of the temperature distribution and (b) gas supply system.

4.2.4 Experimental Conditions

Fig. 4.2 shows the flow rate of the gas composition in the mixed fuel. When the flow rate of methane was 0 ml/min, that is a single fuel of ammonia without methane was supplied, the flow rate of ammonia was 80 ml/min. The compositions of humidified methane and ammonia in the mixed fuel were determined by considering that the total hydrogen production rate from both methane and ammonia would become constant if the two fuels were completely converted to hydrogen. The total flow rate of the inlet gas and the temperature of the electric furnace were fixed at 360 ml/min and 700 °C, respectively.

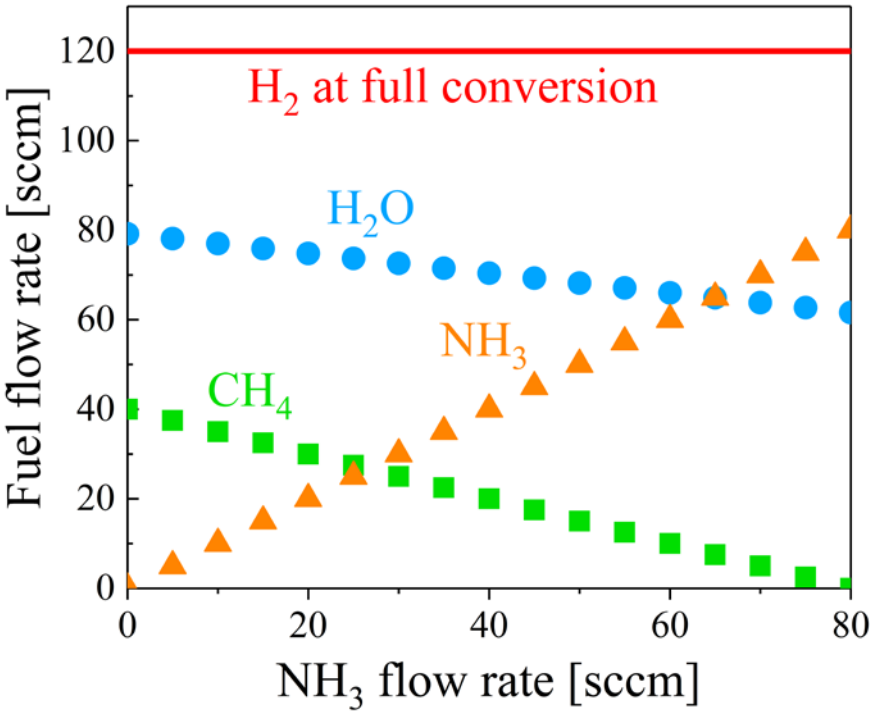

Fig. 4.2 Experimental conditions.

4.2.5 Data Reduction

To evaluate the experimental results, the reaction rates of methane and ammonia were calculated as

$$\text{CH}_4 \text{ Reforming rate } = \left(\frac{\Delta VF_{\text{CH}_4}}{VF_{\text{CH}_4,\text{ in}}}\right) \times 100 \; = \left(1 - \frac{VF_{\text{CH}_4,\text{ out}}}{VF_{\text{CH}_4,\text{ in}}}\right) \times 100 \; [\%], \tag{4.4}$$

$$\text{NH}_3 \text{ Decomposition rate } = \left(\frac{\Delta VF_{\text{NH}_3}}{VF_{\text{NH}_3,\text{ in}}}\right) \times 100 = \left(1 - \frac{2VF_{\text{N}_2,\text{ out}}}{VF_{\text{NH}_3,\text{ in}}}\right) \times 100 \; [\%], \tag{4.5}$$

where $VF_{\text{CH4, in}}$ and $VF_{\text{NH3, in}}$ are the volumetric flow rates of methane and ammonia at the inlet controlled by the mass flow controllers, whereas $VF_{\text{CH4, out}}$ and $VF_{\text{N2, out}}$ are those of methane and nitrogen at the outlet measured by gas chromatography, respectively.

4.2.6 Stability, Durability, and Reproducibility

To confirm that the catalyst was not degraded during the experiment, the reaction rate under the reference condition, i.e., an ammonia flow rate of 40 ml/min with balance argon of 320 ml/min at the inlet, was examined at the beginning and end of each series of experiments. In all cases, the difference in ammonia decomposition rate between the beginning and end of the experiment was less than 3.5%, which confirms the stability of the catalyst and the reproducibility of the results.

4.3 Results and discussion

As discussed in the previous chapter, the ammonia decomposition reaction preferentially proceeds over the steam methane reforming reaction. Moreover, the steam methane reforming reaction has a strongly endothermic nature, which is suitable for efficient heat utilization, whereas the ammonia decomposition reaction has a weakly endothermic nature, which can realize a gentle temperature distribution. From these characteristics, in the case of using the mixed fuel, it can be predicted that ammonia decomposition preferentially proceeds mainly in the upstream region of the cell, thus avoiding the steep temperature drop around the inlet, and methane steam reforming, which probably follows the decomposition of ammonia, enables the high efficiency of heat utilization to be retained. Therefore, the temperature distribution along the length of the Ni–YSZ catalyst was investigated by using an IR camera. The hydrogen production rate and the amount of endothermic heat of both reactions were also examined.

4.3.1 Measurement of Thermal Field

In this analysis, the amount of the catalyst was increased to 0.75 g and 1.5 g, which were equivalent to the streamwise lengths of 21 mm and 42 mm, respectively. To clearly recognize changes in local temperature on the catalyst caused by the reactions, a subtraction process was applied to the thermal images obtained by the IR camera as follows. First, a thermal image when argon was supplied was obtained as a reference, as shown in Fig. 4.3 (a), then another image was obtained when the fuel was supplied, as shown in Fig. 4.3 (b). Fig. 4.3 (c) was then obtained as the difference between the two. There appears to be a temperature distribution in the spanwise direction; however, this is due to the measurement of the cylindrical tube from the side. Therefore, the temperature at the center of the flow channel was used as the representative temperature at each position x in the evaluation.

The flow rate of ammonia was 80 ml/min when a single fuel of ammonia without methane was supplied. The compositions of humidified methane and ammonia in the mixed fuel were determined by considering that the total hydrogen production rate from both methane and ammonia would become constant if the two fuels were completely converted to hydrogen. The total flow rate of the inlet gas was fixed at 360 ml/min and the temperature of the electric furnace was fixed at 700 °C.

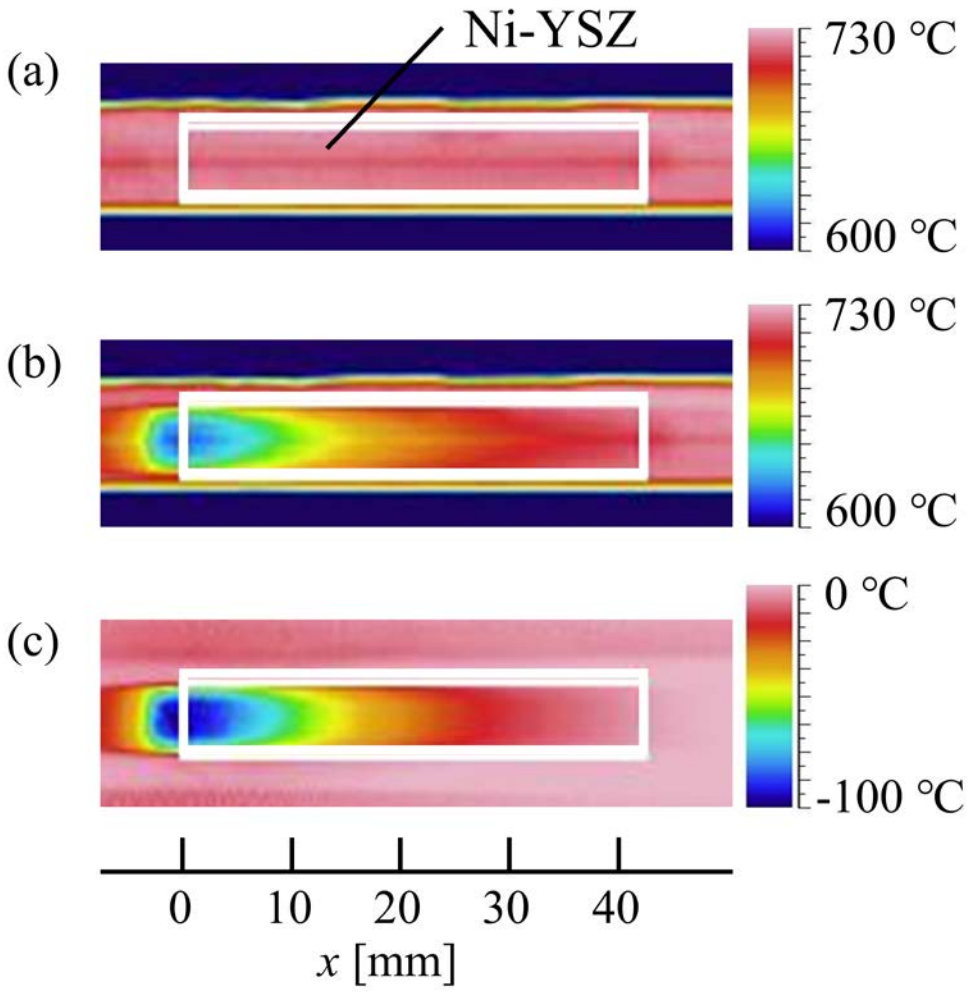

Fig. 4.3 Thermal images of the catalyst (a) without and (b) with reactions. (c) Difference between (a) and (b).

4.3.2 Temperature Distribution

Figs. 4.4 (a) and (b) show the one-dimensional distributions of the temperature drop in the flow direction at the center of the flow channels with the catalyst lengths of 42 mm and 21 mm, respectively. For the catalyst with a length of 42 mm, as shown in Fig. 4.4 (a), when the mole fraction of ammonia is 0, i.e., humidified methane is supplied without ammonia, there is a sharp drop in local temperature at the upstream edge of the catalyst. This is because of the strongly endothermic nature of the reforming reaction. As the mole fraction of ammonia increases, the magnitude of the temperature drop decreases and the peak position moves downstream, as shown by a white arrow. When the mole fraction of ammonia further increases, another peak appears at the upstream edge, as shown by a black arrow. This is associated with the endothermic ammonia decomposition. Fig. 4.4 (a) clearly shows that the temperature distribution can be controlled by tuning the inlet composition of the mixed fuel.

For the catalyst with a length of 21 mm, as shown in Fig. 4.4 (b), the temperature distribution where the catalyst is placed is almost the same as that in the upstream half of the catalyst with a length of 42 mm. On the other hand, in the downstream half, where no catalyst is placed, no peak of the temperature drop caused by steam methane reforming is observed. This is because there is no catalyst in the downstream half and the steam methane reforming reaction, which is delayed because of the ammonia decomposition reaction, cannot take place. Regarding the ammonia decomposition reaction, since it proceeds preferentially in the upstream region, a peak position similar to that observed in Fig. 4.4 (a) is also observed in Fig. 4.4 (b), as shown by a black arrow.

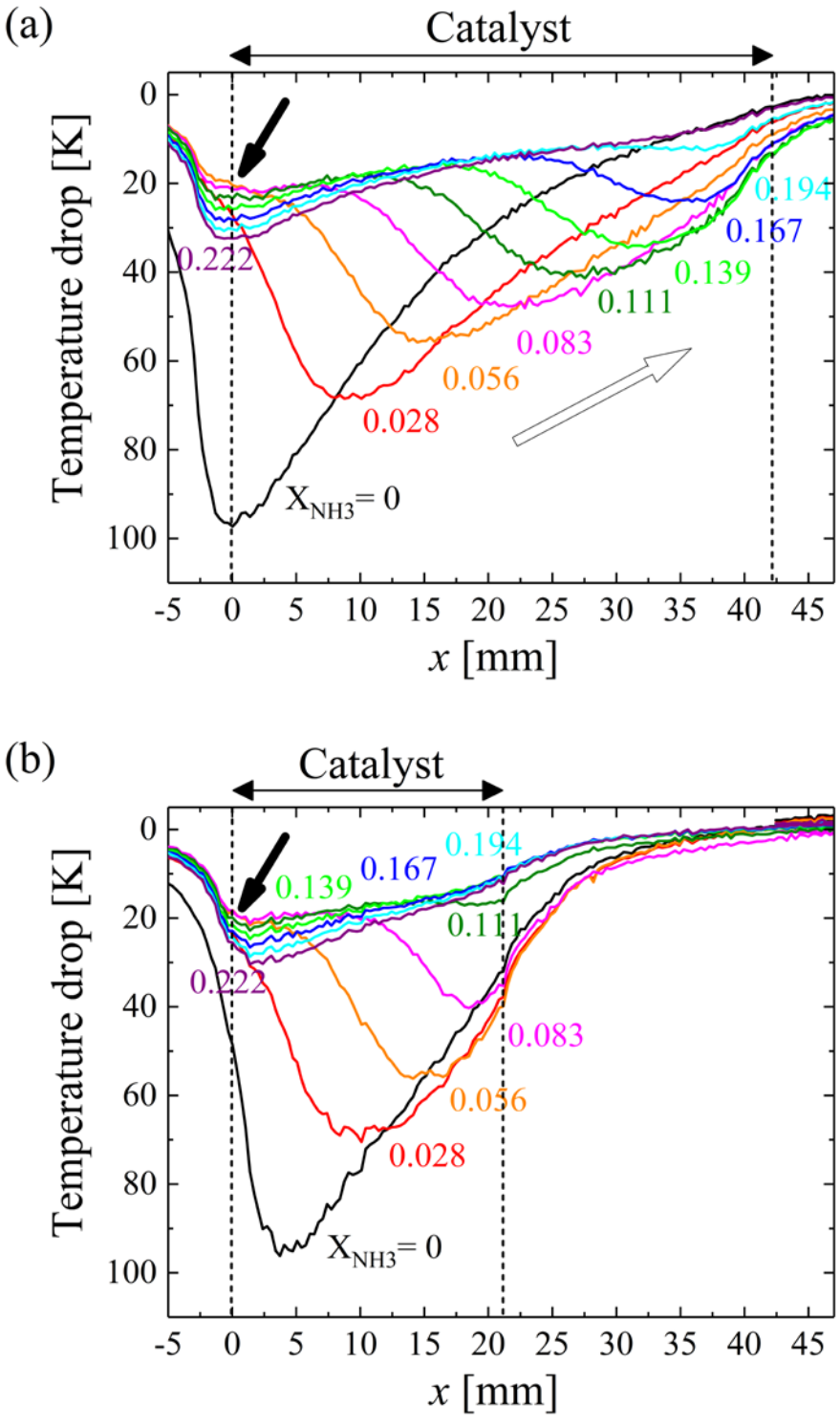

Fig. 4.4 Temperature distributions on the catalyst with lengths of (a) 42 mm and (b) 21 mm.

4.3.3 Hydrogen Production Rate

Figs. 4.5 (a) and (b) show the reaction rates of steam methane reforming and ammonia decomposition with the catalyst lengths of 42 mm and 21 mm, respectively. They also show the total hydrogen production rate from both reactions for each catalyst length. Note again that the compositions of humidified methane and ammonia in the mixed fuel are determined by considering that the total hydrogen production rate from both methane and ammonia would become constant if the two fuels were completely converted to hydrogen.

For the catalyst with a length of 42 mm, as shown in Fig. 4.5 (a), the hydrogen production rate slightly increases up to an ammonia mole fraction of 0.11. When the mole fraction of ammonia is more than 0.16, on the other hand, the hydrogen production rate starts to decrease. This is associated with the drop in the methane reforming rate caused by the reaction preference of ammonia decomposition at a high ammonia concentration.

For the catalyst with a length of 21 mm, as shown in Fig. 4.5 (b), the methane reaction and hydrogen production rates decrease with increasing ammonia even though the ammonia decomposition rate itself slightly increases up to a mole fraction of ammonia of 0.056. This indicates that sufficient steam methane reforming cannot take place within the catalyst with a length of 21 mm owing to the reaction preference of ammonia decomposition. It is worth mentioning that no steam methane reforming reaction is observed when the mole fraction of ammonia is larger than 0.14.

Fig. 4.5 (c) shows the differences in the reaction rates of methane and ammonia between the two lengths of the catalyst. Since the temperature distribution in the catalyst with a length of 21 mm is almost the same as that in the upstream half of the catalyst with a length of 42 mm, shown in Figs. 4.4 (a) and (b), it can be considered that the composition of the gas exhausted from the catalyst with a length of 21 mm represents that of the gas passing through the upstream

half of the catalyst with a length of 42 mm. Therefore, the differences in the reaction rates of methane and ammonia between the two lengths of the catalyst shown in Fig. 4.5 (c) represent the estimated rates of the reactions that proceed in the downstream half of the catalyst with a length of 42 mm. It is shown that up to an ammonia mole fraction of 0.14, the estimated reaction rate of methane increases. This indicates that the region where the methane reforming reaction proceeds shifts to the downstream part of the catalyst because a longer region of the catalyst from the inlet was occupied mainly by the preferential reaction, namely, the ammonia decomposition reaction. When the mole fraction of ammonia is more than 0.14, on the other hand, the estimated reaction rate of methane reforming rapidly decreases. This is because the amount of ammonia remaining after passing through the upstream half of the catalyst increased; thus, the downstream half of the catalyst was also used mainly for the ammonia decomposition reaction, resulting in the reduced activity of the steam methane reforming reaction. From these results, it can be predicted that the remaining ammonia when the ammonia mole fraction is high can be consumed if the catalyst is further longer. Furthermore, this shows that the region of the catalyst in which steam methane reforming proceeds can be controlled by changing the composition of the mixed fuel.

(a)

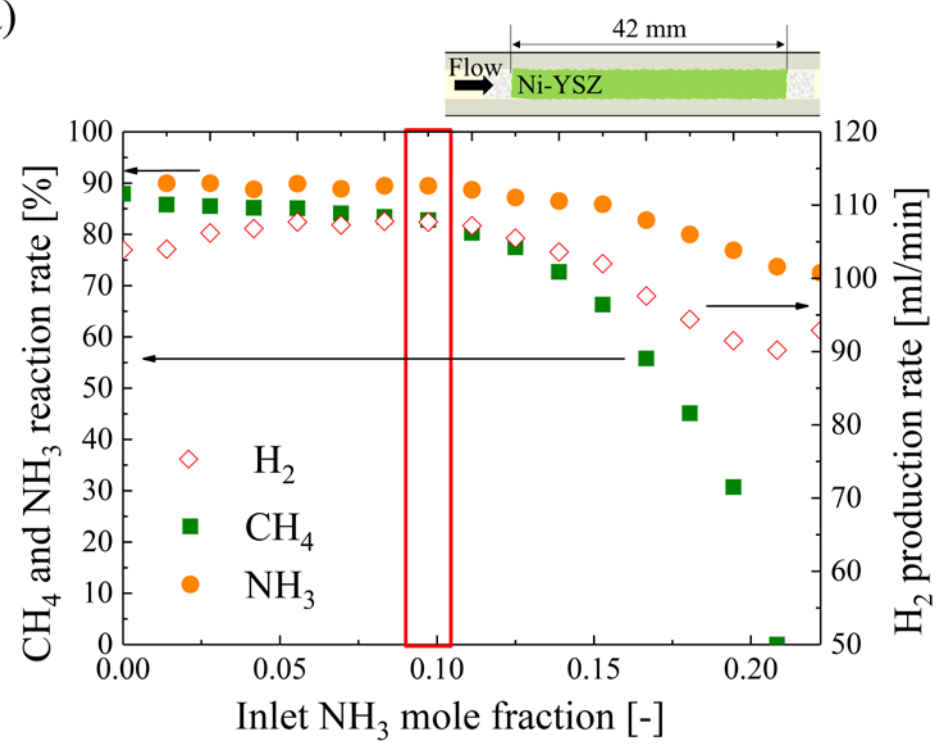
42 mm
Flow
Ni-YSZ
CH4 and NH3 reaction rate [%]
H2 production rate [ml/min]
H2
CH4
NH3
Inlet NH3 mole fraction [-]

(b)

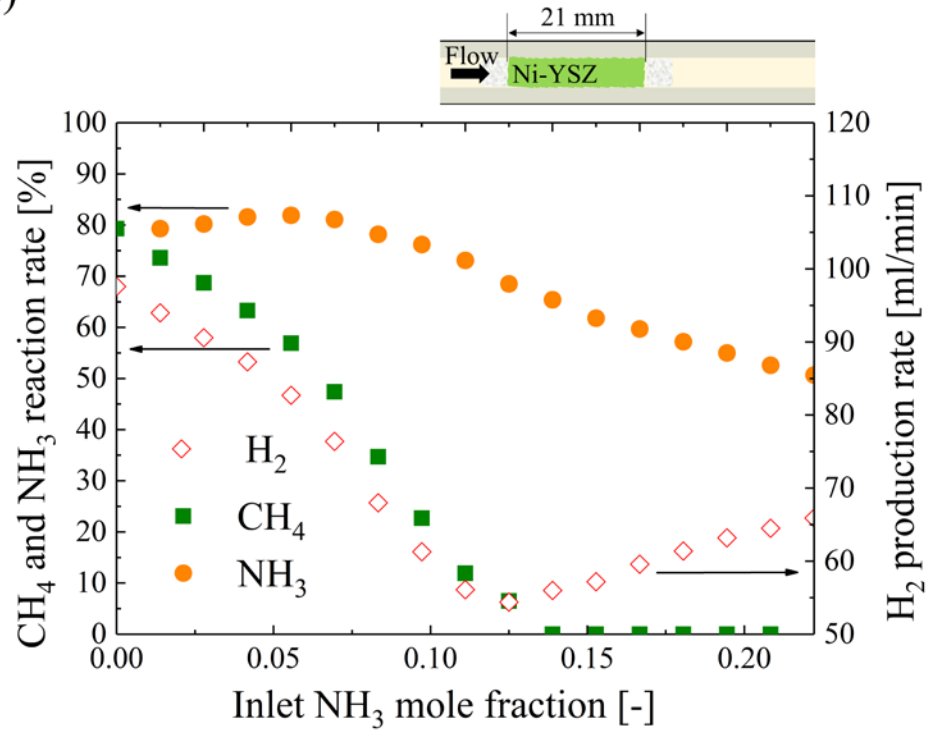
21 mm
Flow
Ni-YSZ
CH4 and NH3 reaction rate [%]
H2 production rate [ml/min]
H2
CH4
NH3
Inlet NH3 mole fraction [-]

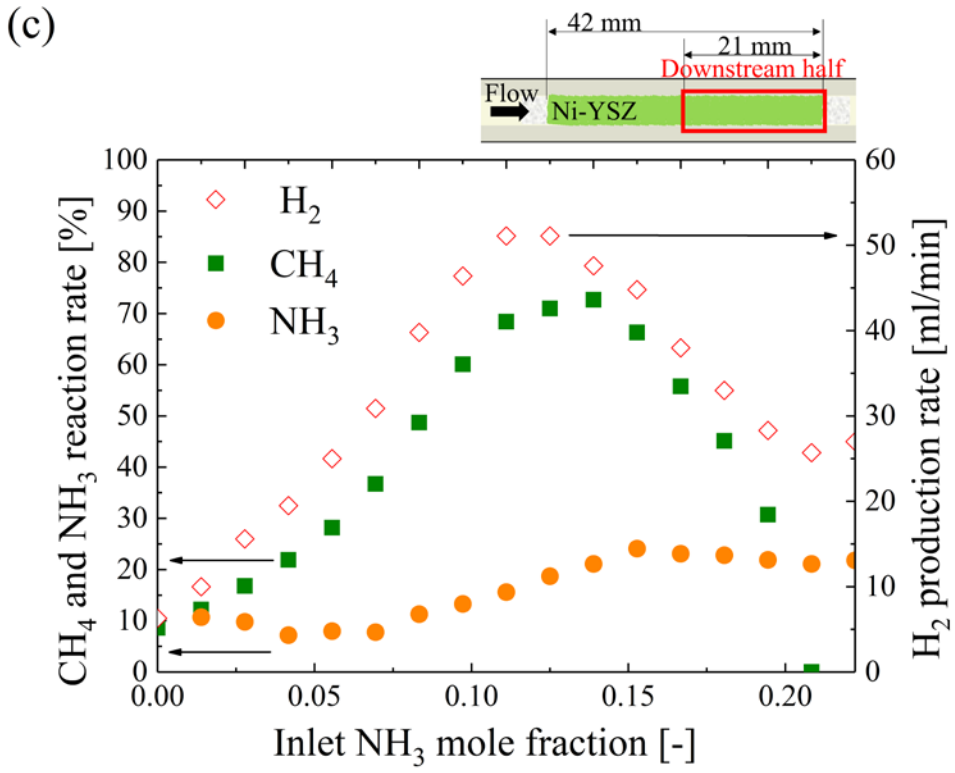

Fig. 4.5 Reaction rates and hydrogen production rate with the catalyst length of (a) 42 mm, (b) 21 mm, and (c) the difference of the two which represents the estimated rate of the reactions proceeding in the downstream half part of the catalyst with 42 mm length.

4.3.4 Heat Utilization

Fig. 4.6 shows the amounts of endothermic heat associated with the steam methane reforming and ammonia decomposition reactions when the catalyst length is 42 mm. It also includes the average, minimum, and maximum temperatures within the catalyst for each condition. It is shown that the total amount of endothermic heat decreases with increasing mole fraction of ammonia, resulting in an increase in average temperature. This is because the amount of endothermic heat of the ammonia decomposition reaction is smaller than that of the steam methane reforming reaction.

When the ammonia concentration in the mixed fuel is 0.10, as shown by a red column in Fig. 4.5 (a) and Fig. 4.6, the hydrogen production rate is maximized; its amount is larger than that for the single fuel of humidified methane and that for the single fuel of ammonia. In addition, although the amount of endothermic heat is 27% smaller than that of the single fuel of humidified methane because of the less endothermic nature of the ammonia decomposition reaction, it is 98% larger than that of the single fuel of ammonia, indicating the efficient utilization of the heat generated by the electrochemical reaction. Furthermore, the difference between the maximum and minimum temperatures within the catalyst is 56% smaller than that in the case of humidified methane without ammonia and almost equivalent to that of the single fuel of ammonia without methane. From these results, it can be clearly concluded that the mixed fuel has advantages in terms of hydrogen production rate, temperature distribution, and heat utilization over the single fuels of humidified methane and ammonia.

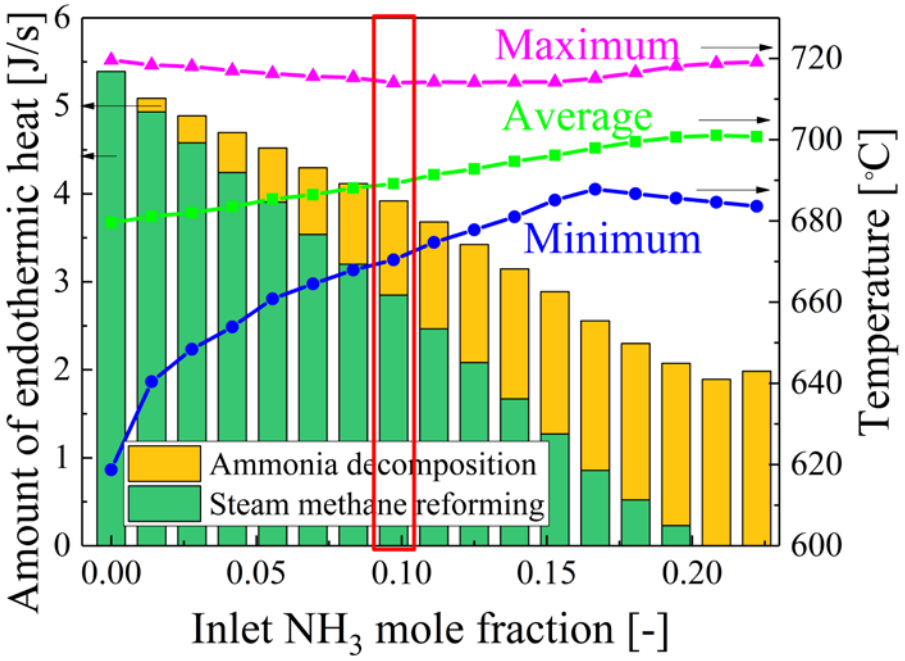

Fig. 4.6 Amounts of endothermic heat and catalyst temperature.

4.3.5 Hydrogen Reuse in SOFCs

Considering the fact that ammonia decomposition preferentially proceeds over steam methane reforming, there is one more advantage that can be expected from mixing methane and ammonia. When methane–ammonia mixed fuel is supplied to SOFCs, hydrogen is first produced from the decomposition of ammonia. This hydrogen is used as a fuel for the electrochemical reaction to generate electricity and, as a result, water is produced. This water can be used for steam methane reforming so that hydrogen is again produced and used for the electrochemical reaction. This shows a possibility that the hydrogen atoms originally contained in ammonia can act twice as a fuel for the electrochemical reaction. The amount of steam supply can also be reduced. To clarify the reuse of water in the methane–ammonia mixed fuel in SOFCs, further research is needed.

4. Conclusions

To control the temperature distribution and make it gentle along the flow direction in the anode of SOFCs while efficiently utilizing the heat generated by the electrochemical reaction, the concept of mixing fuels was examined. The combination of methane and ammonia, which have large differences in their reaction activity and endothermic nature, was adopted based on the fundamental reforming characteristics of the mixed fuel on the Ni–YSZ catalyst obtained in Chapter 3.

It was found that when the mixed fuel is supplied to the catalyst with a length along the flow direction, as the mole fraction of ammonia in the mixed fuel was increased, ammonia was preferentially consumed near the inlet and the reaction region of steam methane reforming on the catalyst was moved downstream, resulting in the shift of the position where the temperature of the catalyst sharply drops. The temperature distribution can be controlled by tuning the compositions of methane and ammonia in the mixed fuel.

When the mixture ratio of methane to ammonia was suitably adjusted, a higher hydrogen production rate was achieved compared with the cases of a single fuel of humidified methane and a single fuel of ammonia. The temperature difference within the catalyst was 56% smaller than that in the case of humidified methane and the amount of endothermic heat was 98% larger than that in the case of ammonia. Moreover, it shows a possibility that the hydrogen atoms originally contained in ammonia are used twice as a fuel for electrochemical reaction in an SOFC. Therefore, methane–ammonia mixed fuel has advantages in terms of hydrogen production rate, temperature distribution, and heat utilization over the single fuels of humidified methane and ammonia, and the concept of mixing fuels with large differences in their reaction activity and endothermic nature is an attractive option for realizing the more flexible operation of SOFCs.

Bibliography

1. Achenbach E, Riensche E. Methane/steam reforming kinetics for solid oxide fuel cells. *J Power Sources*. 1994;52(2):283-288. doi:10.1016/0378-7753(94)02146-5
2. Laosiripojana N, Assabumrungrat S. Catalytic steam reforming of methane, methanol, and ethanol over Ni/YSZ: The possible use of these fuels in internal reforming SOFC. *J Power Sources*. 2007;163(2):943-951. doi:10.1016/j.jpowsour.2006.10.006
3. Huang TJ, Wu CY, Wang CH. Fuel processing in direct propane solid oxide fuel cell and carbon dioxide reforming of propane over Ni–YSZ. *Fuel Process Technol*. 2011;92(8):1611-1616. doi:10.1016/j.fuproc.2011.04.007
4. Liu M, Peng R, Dong D, Gao J, Liu X, Meng G. Direct liquid methanol-fueled solid oxide fuel cell. *J Power Sources*. 2008;185(1):188-192. doi:10.1016/j.jpowsour.2008.06.076
5. Hong-xin YOU, Guo-dong GAO, Liang Z, Abudula A. Power generating performances of ethanol on the SOFC. *J Fuel Chem Technol*. 2010;38(1):116-120. doi:10.1016/S1872-5813(10)60023-0
6. Murray EP, Harris SJ, Jen H. Solid oxide fuel cells utilizing dimethyl ether fuel. *J Electrochem Soc*. 2002;149(9):A1127. doi:10.1149/1.1496484
7. Homel M, Gür TM, Koh JH, Virkar A V. Carbon monoxide-fueled solid oxide fuel cell. *J Power Sources*. 2010;195(19):6367-6372. doi:10.1016/j.jpowsour.2010.04.020
8. Wojcik A, Middleton H, Damopoulos I, Van Herle J. Ammonia as a fuel in solid oxide fuel cells. *J Power Sources*. 2003;118(1-2):342-348. doi:10.1016/S0378-7753(03)00083-1
9. Molouk AFS, Okanishi T, Muroyama H, Matsui T, Eguchi K. Electrochemical and catalytic behaviors of Ni–YSZ anode for the direct utilization of ammonia fuel in solid

oxide fuel cells. *J Electrochem Soc*. 2015;162(10):F1268-F1274.

doi:10.1149/2.1011510jes

Chapter 5

Formulation of Mixed Fuel Reaction Rate on Ni–YSZ Catalyst

5.1 Introduction

Solid Oxid Fuel Cells (SOFCs) are a promising technology owing to their high power generation efficiency. One of the important characteristics of SOFCs is their fuel flexibility. Because electrolytes of the SOFCs are typically oxygen–ion conducting ceramics, the fuel is not limited to hydrogen. Various kinds of fuel such as methane [1–3], propane [4–8], methanol [3,9–11], ethanol [9,12–17], dimethyl ether [18–21], carbon monoxide [22–25], and ammonia [26–28] can be used in SOFCs. The high operation temperature of SOFCs gives an additional advantage from the energy efficiency point of view: the excess heat can be effectively utilized in the endothermic reforming process of hydrocarbon fuels to generate hydrogen, which can also be regarded as a cooling process of the stack. A separate reformer is usually placed next to the SOFC stack today.

Since the typical SOFC anode such as Ni–YSZ (yttria-stabilized zirconia) contains nickel, which can function as a reforming catalyst, it is possible to directly supply hydrocarbon fuels or ammonia to the SOFCs to perform on-site reforming on the anode. It is an advanced

operation mode of SOFCs and called as a “direct reforming”. This operation eliminates the separate reformer so that the system can be simple and cost-competitive. The excess heat is internally utilized for the endothermic reforming process and this can be regarded as the internal cooling process of the stack. In spite of the intensive investigations on the direct reforming SOFCs [29–32], there are still challenges to realize this operation mode. Its impact on the temperature field is one of them. When methane is used as a fuel, for instance, the reforming reaction proceeds rapidly near the inlet of the anode channel, resulting in a decrease of the local cell temperature owing to its strongly endothermic nature. This generates unacceptable thermal stress and increase the risk of mechanical failure of cells [33–35]. When the weakly endothermic fuel such as ammonia is adopted, it is possible to obtain the relatively uniform temperature distribution, but the excess heat utilization is sacrificed because the amount of endothermic heat is small.

The idea of this study is to use a mixed fuel of methane and ammonia combining the advantages of the fuels having different characters. The experimental results presented in the previous chapters are positive, showing the feasibility of the proposed method to control the temperature field in the SOFC stacks. Because of the difficulty to experimentally measure the temperature field of an operating SOFC, it is significant to introduce the numerical simulation. One of the key factors to build up the numerical model of SOFCs fed with the mixed fuel is how to describe the direct reforming reactions. Since the experimental results indicate that the steam methane reforming and ammonia decomposition reactions interact each other, the reaction model should be able to describe the interactions of both fuels.

One straightforward method is to employ an elementary kinetics model considering all elementary reactions involved in the reforming and decomposition reactions [36–38]. The competitive nature of the two reactions will be automatically considered in this method. However, the computational load will be high particularly if it is applied to a stack level

simulation. In a stack level simulation of direct reforming SOFCs, an overall reaction model, in which the reaction rates are described with power-law expressions, is often employed because of its reasonable computational load [2,39,40]. Since the power-law model is obtained by fitting to a reliable experimental data, the obtained rate equation should be used within the range of the experimental condition. One challenge in the power-law model is how to introduce the competitive nature of the two reactions. To the best knowledge of the author, there is no simple method describing the two competitive reactions which is practically applicable to a stack-level simulation.

In this chapter, we propose a new reaction model to describe the two competitive reactions by implicitly considering the surface reaction model: adsorption, associative reaction, and desorption. The model can describe the mixed fuel condition by introducing the adsorption constants of the participating gas species on the surface, but without considering each elementary reaction. By fitting to the experimental results reported in Chapter 3, the reaction rate formulae of the steam methane reforming and ammonia decomposition which can be used even in the mixed fuel system are introduced. Furthermore, the effect of the YSZ support on the rate of steam methane reforming is examined considering the steam and ammonia adsorptions on YSZ.

5.2 Reaction Model

To describe the competitive nature of the two reactions, the adsorption and desorption phenomena of all chemical species on the nickel surface are considered. On the other hand, the associative reactions of steam methane reforming and ammonia decomposition on the nickel surface are regarded as the smallest components of overall reactions and the elementary reactions which consist these associative reactions are not taken into account. To achieve this goal, we propose a new reaction rate description method of the associative reactions on the surface. It does not require the use of elementary reactions and, instead, a constant which should be obtained from the fitting of the experimental data is introduced.

5.2.1 Reactions to be Considered

The overall reactions of steam methane reforming and ammonia decomposition reactions are described as Eq. (5.1) and Eq. (5.2), respectively. Water–gas shift reaction is given by Eq. (5.3).

$$CH_4 + H_2O \rightarrow CO + 3H_2 \qquad \Delta H^0_{298} = 206 \text{ kJ/mol} \tag{5.1}$$

$$NH_3 \rightarrow \frac{1}{2}N_2 + \frac{3}{2}H_2 \qquad \Delta H^0_{298} = 46 \text{ kJ/mol} \tag{5.2}$$

$$CO + H_2O \leftrightarrow CO_2 + H_2 \qquad \Delta H^0_{298} = -41 \text{ kJ/mol} \tag{5.3}$$

In this study, it is assumed that these surface reactions proceed in three steps: adsorption, associative reaction, and desorption. The adsorption and desorption reactions of all chemical species are in equilibrium states and the reaction rates are determined by the associative reactions on the nickel surface.

The adsorption and desorption of the chemical species in the steam methane reforming and ammonia decomposition can be described as follows;

$$CH_4 + V \overset{K_{CH_4}}{\longleftrightarrow} CH_{4ad} \tag{5.4}$$

$$H_2O + V \overset{K_{H_2O}}{\longleftrightarrow} H_2O_{ad} \tag{5.5}$$

$$H_2 + 2V \overset{K_H}{\leftrightarrow} 2H_{ad} \tag{5.6}$$

$$CO + V \overset{K_{CO}}{\longleftrightarrow} CO_{ad} \tag{5.7}$$

$$CO_2 + V \overset{K_{CO_2}}{\longleftrightarrow} CO_{2ad} \tag{5.8}$$

$$NH_3 + V \overset{K_{NH3}}{\longleftrightarrow} NH_{3ad} \tag{5.9}$$

$$N_2 + 2V \overset{K_N}{\leftrightarrow} 2N_{ad} \tag{5.10}$$

where V shows the vacant reaction sites on the nickel catalyst and the subscript "ad" means adsorption on the nickel surface. K_{CH4}, K_{H2O}, K_H, K_{CO}, K_{CO2}, K_{NH3}, and K_N are the equilibrium constants.

The associative reactions of methane and ammonia on nickel surface are described as follows:

$$CH_{4ad} + H_2O_{ad} \leftrightarrow 6H_{ad} + CO_{ad} \tag{5.11}$$

$$NH_{3ad} \leftrightarrow 3H_{ad} + N_{ad} \tag{5.12}$$

Note that in the elementary reaction model these reactions are further divided into several elementary reactions. Instead, in this analysis, these reactions are regarded as the smallest components of the reaction model.

When the coverage of each species j (j = CH_4, H_2O, H, CO, CO_2, NH_3, N, V) is denoted by θ_j, the equilibrium constants of the reactions shown in Eq. (5.4) to Eq. (5.10) are expressed with the coverages and partial pressures of the gases.

$$K_{CH_4} = \frac{\theta_{CH_4}}{P_{CH_4}\theta_V} \tag{5.13}$$

$$K_{H_2O} = \frac{\theta_{H_2O}}{P_{H_2O}\theta_V} \tag{5.14}$$

$$K_{\mathrm{H}} = \frac{{\theta_{\mathrm{H}}}^2}{P_{\mathrm{H_2}}{\theta_{\mathrm{V}}}^2} \tag{5.15}$$

$$K_{\mathrm{CO}} = \frac{\theta_{\mathrm{CO}}}{P_{\mathrm{CO}}\theta_{\mathrm{V}}} \tag{5.16}$$

$$K_{\mathrm{CO2}} = \frac{\theta_{\mathrm{CO2}}}{P_{\mathrm{CO_2}}\theta_{\mathrm{V}}} \tag{5.17}$$

$$K_{\mathrm{NH_3}} = \frac{\theta_{\mathrm{NH_3}}}{P_{\mathrm{NH_3}}\theta_{\mathrm{V}}} \tag{5.18}$$

$$K_{\mathrm{N}} = \frac{{\theta_{\mathrm{N}}}^2}{P_{\mathrm{N_2}}{\theta_{\mathrm{V}}}^2} \tag{5.19}$$

where P_{CH4}, P_{H2O}, P_{H2}, P_{CO}, P_{CO2}, P_{NH3}, and P_{N2} are the partial pressures of methane, steam, hydrogen, carbon monoxide, carbon dioxide, ammonia, and nitrogen.

5.2.2 Reaction Rate

In this analysis, the associative reaction on the nickel surface is assumed to be the rate-limiting step so that the overall reaction rates of steam methane reforming and ammonia decomposition can be represented by their associative reaction rates. Since the associative reaction takes place on the surface, its reaction rate can be expressed by the products of coverage of the participating species, θ_j, and vacant reaction site, θ_{v}. The power of each coverage is usually the stoichiometric value. This is because the probability of the association of chemical species including vacant sites can be calculated by the power of the coverages with their stoichiometric values.

When the associative reaction is regarded as the smallest component of the reactions, the sequential elementary reactions will be represented by one associative reaction. In this case, the probability of a certain number of the sequential associations of a chemical species with vacant sites should be represented by the probability of one association of a chemical species with a certain number of neighboring vacant sites. However, these two probabilities are generally different, so that the probability description of one associative reaction should be

adjusted to successfully represent the probability of the sequential associations. To achieve this, we introduce a constant as the power of the coverage of vacant site θ_v, which will be shown in the following examples.

5.2.2.1 Reaction Rate of Steam Methane Reforming

When the reaction rate of the associative reaction of the steam methane reforming on the catalyst surface, shown in Eq. (5.11), is described on the basis of the proposed model, the rate equation can be expressed as follows;

$$R_{\mathrm{SMR}} = {k_{\mathrm{SMR}}}^{+}\theta_{\mathrm{CH_4}}\theta_{\mathrm{H_2O}}{\theta_{\mathrm{V}}}^{a} - {k_{\mathrm{SMR}}}^{-}{\theta_{\mathrm{H}}}^{6}\theta_{\mathrm{CO}} \tag{5.20}$$

$${k_{SMR}}^{+} = {A_{SMR}}^{+}\exp\left(-\frac{\Delta {E_{SMR}}^{+}}{RT}\right) \tag{5.21}$$

$${k_{SMR}}^{-} = {A_{SMR}}^{-}\exp\left(-\frac{\Delta {E_{SMR}}^{-}}{RT}\right) \tag{5.22}$$

where ${k_{\mathrm{SMR}}}^{+}$ and ${k_{\mathrm{SMR}}}^{-}$ show the reaction rate constants of forward and backward reactions so that their temperature dependence can be described by Arrhenius equations, shown in Eqs. (5.21) and (5.22). The power of θ_v is a constant a. This can be explained as follows. If the elementary reactions on the surface are considered, four hydrogen atoms in methane are adsorbed step-by-step on nickel. In this case, the number of vacant sites which is required for each adsorption step is just one. These reactions proceed sequentially so that the probability of methane adsorption as a whole can be calculated as the products of the probability of each step. On the other hand, if the stoichiometric number of vacant sites for Eq. (5.20) is adopted as a, namely $a = 5$, the term ${\theta_{\mathrm{V}}}^{\mathrm{a}}$ shows the probability that five neighboring vacant sites located next to the adsorbed site can be used for the reaction. Clearly, the probability of the products of each sequential step in which only one adjacent vacant site is required and the probability of the existence of five continuous vacant sites are not necessarily the same. Therefore, the value of a, which is expected to be around 5, should be obtained by fitting the experimental data.

5.2.2.2 Reaction Rate of Ammonia Decomposition

The reaction rate of ammonia decomposition can be calculated in the same manner as the case of methane. When the reaction rate of ammonia decomposition on nickel surface can be determined by its associative reaction on the surface, the reaction rate can be expressed as follows;

$$R_{\mathrm{ADC}} = k_{\mathrm{ADC}}{}^{+}\theta_{\mathrm{NH_3}}\theta_{\mathrm{V}}{}^{b} - k_{\mathrm{ADC}}{}^{-}\theta_{\mathrm{H}}{}^{3}\theta_{\mathrm{N}} \tag{5.23}$$

$$k_{ADC}{}^{+} = A_{ADC}{}^{+}\exp\left(-\frac{\Delta E_{ADC}{}^{+}}{RT}\right) \tag{5.24}$$

$$k_{ADC}{}^{-} = A_{ADC}{}^{-}\exp\left(-\frac{\Delta E_{ADC}{}^{-}}{RT}\right) \tag{5.25}$$

where $k_{\mathrm{ADC}}{}^{+}$ and $k_{\mathrm{ADC}}{}^{-}$ show the reaction rate constants of forward and backward reactions so that their temperature dependence can be described by Arrhenius equation, shown in Eqs. (5.24) and (5.25). The power of θ_{v} is a constant b. As discussed in the case of methane, it is expected that the constant b takes a value around 3 and it should be obtained from the fitting of the experimental results.

5.2.2.3 Reaction Rates under Mixed Condition

When the associative reactions on the surface are regarded as a rate-limiting step, the reaction rates of the steam methane reforming and ammonia decomposition are expressed by Eqs. (5.20) to (5.23). The species considered are methane, ammonia, steam, hydrogen, carbon monoxide, carbon dioxide and nitrogen. The sum of the coverages of all species is unity;

$$\theta_{\mathrm{CH_4}} + \theta_{\mathrm{H_2O}} + \theta_{\mathrm{H}} + \theta_{\mathrm{CO}} + \theta_{\mathrm{CO_2}} + \theta_{\mathrm{NH_3}} + \theta_{\mathrm{N}} + \theta_{\mathrm{V}} = 1 \tag{5.26}$$

From Eqs. (5.13) to (5.19) and Eq. (5.26), the coverages of each species can be described as follows;

$$\theta_{\mathrm{V}} = \frac{1}{1+K_{\mathrm{CH_4}}P_{\mathrm{CH_4}}+K_{\mathrm{H_2O}}P_{\mathrm{H_2O}}+\sqrt{K_{\mathrm{H}}P_{\mathrm{H_2}}}+K_{\mathrm{CO}}P_{\mathrm{CO}}+K_{\mathrm{CO_2}}P_{\mathrm{CO_2}}+K_{\mathrm{NH_3}}P_{\mathrm{NH_3}}+\sqrt{K_{\mathrm{N}}P_{\mathrm{N_2}}}} \quad (5.27)$$

$$\theta_{\mathrm{CH_4}} = \frac{K_{\mathrm{CH_4}}P_{\mathrm{CH_4}}}{1+K_{\mathrm{CH_4}}P_{\mathrm{CH_4}}+K_{\mathrm{H_2O}}P_{\mathrm{H_2O}}+\sqrt{K_{\mathrm{H}}P_{\mathrm{H_2}}}+K_{\mathrm{CO}}P_{\mathrm{CO}}+K_{\mathrm{CO_2}}P_{\mathrm{CO_2}}+K_{\mathrm{NH_3}}P_{\mathrm{NH_3}}+\sqrt{K_{\mathrm{N}}P_{\mathrm{N_2}}}} \quad (5.28)$$

$$\theta_{\mathrm{H_2O}} = \frac{K_{H_2O}P_{H_2O}}{1+K_{\mathrm{CH_4}}P_{\mathrm{CH_4}}+K_{\mathrm{H_2O}}P_{\mathrm{H_2O}}+\sqrt{K_{\mathrm{H}}P_{\mathrm{H_2}}}+K_{\mathrm{CO}}P_{\mathrm{CO}}+K_{\mathrm{CO_2}}P_{\mathrm{CO_2}}+K_{\mathrm{NH_3}}P_{\mathrm{NH_3}}+\sqrt{K_{\mathrm{N}}P_{\mathrm{N_2}}}} \quad (5.29)$$

$$\theta_{H} = \frac{\sqrt{K_H P_{H_2}}}{1+K_{\mathrm{CH_4}}P_{\mathrm{CH_4}}+K_{\mathrm{H_2O}}P_{\mathrm{H_2O}}+\sqrt{K_{\mathrm{H}}P_{\mathrm{H_2}}}+K_{\mathrm{CO}}P_{\mathrm{CO}}+K_{\mathrm{CO_2}}P_{\mathrm{CO_2}}+K_{\mathrm{NH_3}}P_{\mathrm{NH_3}}+\sqrt{K_{\mathrm{N}}P_{\mathrm{N_2}}}} \quad (5.30)$$

$$\theta_{\mathrm{CO}} = \frac{K_{\mathrm{CO}}P_{\mathrm{CO}}}{1+K_{\mathrm{CH_4}}P_{\mathrm{CH_4}}+K_{\mathrm{H_2O}}P_{\mathrm{H_2O}}+\sqrt{K_{\mathrm{H}}P_{\mathrm{H_2}}}+K_{\mathrm{CO}}P_{\mathrm{CO}}+K_{\mathrm{CO_2}}P_{\mathrm{CO_2}}+K_{\mathrm{NH_3}}P_{\mathrm{NH_3}}+\sqrt{K_{\mathrm{N}}P_{\mathrm{N_2}}}} \quad (5.31)$$

$$\theta_{\mathrm{CO_2}} = \frac{K_{\mathrm{CO_2}}P_{\mathrm{CO_2}}}{1+K_{\mathrm{CH_4}}P_{\mathrm{CH_4}}+K_{\mathrm{H_2O}}P_{\mathrm{H_2O}}+\sqrt{K_{\mathrm{H}}P_{\mathrm{H_2}}}+K_{\mathrm{CO}}P_{\mathrm{CO}}+K_{\mathrm{CO_2}}P_{\mathrm{CO_2}}+K_{\mathrm{NH_3}}P_{\mathrm{NH_3}}+\sqrt{K_{\mathrm{N}}P_{\mathrm{N_2}}}} \quad (5.32)$$

$$\theta_{\mathrm{NH_3}} = \frac{K_{\mathrm{NH_3}}P_{\mathrm{NH_3}}}{1+K_{\mathrm{CH_4}}P_{\mathrm{CH_4}}+K_{\mathrm{H_2O}}P_{\mathrm{H_2O}}+\sqrt{K_{\mathrm{H}}P_{\mathrm{H_2}}}+K_{\mathrm{CO}}P_{\mathrm{CO}}+K_{\mathrm{CO_2}}P_{\mathrm{CO_2}}+K_{\mathrm{NH_3}}P_{\mathrm{NH_3}}+\sqrt{K_{\mathrm{N}}P_{\mathrm{N_2}}}} \quad (5.33)$$

$$\theta_{\mathrm{N}} = \frac{\sqrt{K_{\mathrm{N}}P_{\mathrm{N_2}}}}{1+K_{\mathrm{CH_4}}P_{\mathrm{CH_4}}+K_{\mathrm{H_2O}}P_{\mathrm{H_2O}}+\sqrt{K_{\mathrm{H}}P_{\mathrm{H_2}}}+K_{\mathrm{CO}}P_{\mathrm{CO}}+K_{\mathrm{CO_2}}P_{\mathrm{CO_2}}+K_{\mathrm{NH_3}}P_{\mathrm{NH_3}}+\sqrt{K_{\mathrm{N}}P_{\mathrm{N_2}}}} \quad (5.34)$$

By substituting from Eqs. (5.27) to (5.34) to Eqs. (5.20) and (5.23), the reaction rates of the two reactions can be calculated.

5.2.2.4 Water-Gas Shift Reaction

In this analysis, it is assumed that water–gas shift reaction is in equilibrium state. The equilibrium constant $K_{\mathrm{eq,\,WGS}}$ can be calculated by the empirical equations as follows [41];

$$K_{\mathrm{eq,WGS}} = \exp(-0.2935Z^3 + 0.6351Z^2 + 4.1788Z + 0.3169) \quad (5.35)$$

$$Z = \frac{1000}{T} - 1 \quad (5.36)$$

5.2.3 Adsorption Constant

The adsorption constant of each species on nickel surface can be calculated from Van't Hoff equation, as shown in Eq. (5.37). The changes of enthalpy and entropy indicate the differences between the standard enthalpy and entropy in the gaseous phase and those in the adsorbed phase on nickel, respectively.

$$K_i = \exp\left(-\frac{\Delta G}{RT}\right) = \exp\left(-\frac{\Delta H - T\Delta S}{RT}\right) \quad (5.37)$$

where ΔG, ΔH and ΔS denote the changes of Gibbs free energy, enthalpy and entropy, respectively.

The properties adopted for our calculation are summarized in Table 5.1. The changes of enthalpy ΔH and entropy ΔS of steam, hydrogen, carbon monoxide and carbon dioxide due to the adsorption are cited from the DFT calculation results [42]. Those of methane are obtained from the thermal data based on the experiment [43]. Those of nitrogen are obtained from the DFT calculation [44]. Regarding ammonia, although several reports can be found about the change of enthalpy ΔH_{NH3}, the values are different depending on the reports [45–47]. Moreover, there seems to be no valid report on the change of entropy ΔS_{NH3} associated with the adsorption on the nickel surface. Therefore, we introduced the values of $\Delta H_{NH3,\,Ni}$ and $\Delta S_{NH3,\,Ni}$ from our fitting calculation.

Table 5.1 Kinetic model parameters used for calculation

Reaction	ΔH [kJ mol^{-1}]	ΔS [J mol^{-1} K^{-1}]
$CH_4 + V \overset{K_{CH_4}}{\longleftrightarrow} CH_{4ad}$	–41.6	–194
$H_2O + V \overset{K_{H_2O}}{\longleftrightarrow} H_2O_{ad}$	–18	–83
$H_2 + 2V \overset{K_H}{\leftrightarrow} 2H_{ad}$	–92	–129
$CO + V \overset{K_{CO}}{\longleftrightarrow} CO_{ad}$	–121	–132
$CO_2 + V \overset{K_{CO_2}}{\longleftrightarrow} CO_{2ad}$	–28	–103
$NH_3 + V \overset{K_{NH3}}{\longleftrightarrow} NH_{3ad}$	Not Available Fitting	Not Available Fitting
$N_2 + 2V \overset{K_N}{\leftrightarrow} 2N_{ad}$	173	–91.6

5.2.4 Effect of Catalyst Support

It is reported that the catalyst support affects the reaction rate of steam methane reforming. One of the possible reasons is the difference of the steam adsorption on the support, which depends on the support material. Its characteristics difference varies the rate of the steam methane reforming on the catalyst from –0.6 to +1 order when the rate is expressed by the power-law type equation [48]. When the single fuel of humidified methane is supplied, the effect of steam adsorption on the support, namely YSZ, is automatically included in the reaction rate estimation on nickel in the proposed model. When the mixed fuel of methane and ammonia is supplied, however, the steam adsorption on YSZ surface may change because of ammonia and its decomposed gases. It may affect the reaction rate of steam methane reforming on nickel. Therefore, we revise the proposed model to include the possible effects of the steam adsorption change on YSZ.

Assuming that the steam adsorption on YSZ, described as $\theta_{\mathrm{H2O,\,YSZ}}$, has some effects on the steam adsorption on nickel, the reaction rate of steam methane reforming is modified as follows;

$$R_{\mathrm{SMR}} = {k_{\mathrm{SMR}}}^{+}\theta_{\mathrm{CH_4}} f\left(\theta_{\mathrm{H_2O,\,YSZ}}\right)\theta_{\mathrm{H_2O}}{\theta_{\mathrm{V}}}^{a} - {k_{\mathrm{SMR}}}^{-}{\theta_{\mathrm{H}}}^{6}\theta_{\mathrm{CO}} \tag{5.38}$$

where f is some kind of function associated with the steam adsorption on YSZ, and $\theta_{\mathrm{H2O,\,YSZ}}$ is the coverage of steam on YSZ. The adsorption phenomenon of steam on the YSZ surface is described as the same manner on the nickel surface as shown in Eq. (5.29).

$$\theta_{\mathrm{H_2O,\,YSZ}} = \frac{K_{\mathrm{H_2O,\,YSZ}}P_{\mathrm{H_2O}}}{1+K_{\mathrm{CH_4,\,YSZ}}P_{\mathrm{CH_4}}+K_{\mathrm{H_2O,\,YSZ}}P_{\mathrm{H_2O}}+\sqrt{K_{\mathrm{H,\,YSZ}}P_{\mathrm{H_2}}}+K_{\mathrm{CO,\,YSZ}}P_{\mathrm{CO}}+K_{\mathrm{CO_2,\,YSZ}}P_{\mathrm{CO_2}}+K_{\mathrm{NH_3,\,YSZ}}P_{\mathrm{NH_3}}+\sqrt{K_{\mathrm{N,\,YSZ}}P_{\mathrm{N_2}}}} \tag{5.39}$$

where $K_{\mathrm{CH4,\,YSZ}}$, $K_{\mathrm{H2O,\,YSZ}}$, $K_{\mathrm{H,\,YSZ}}$, $K_{\mathrm{CO,\,YSZ}}$, $K_{\mathrm{CO2,\,YSZ}}$, $K_{\mathrm{NH3,\,YSZ}}$, and $K_{\mathrm{N,\,YSZ}}$ are the equilibrium

constants of adsorption for each species on YSZ.

Here, we estimated the order of the adsorption constant of each gas referring to the value adsorbed by other materials [46,47,49–52]. It is also assumed that the adsorption of ammonia is dominant and adsorption constants of other gases can be neglected. Therefore, Eq. (5.39) can be modified as;

$$\theta_{\mathrm{H_2O,\,YSZ}} \approx \frac{K_{\mathrm{H_2O}} P_{\mathrm{H_2O}}}{K_{\mathrm{NH_3}} P_{\mathrm{NH_3}}} \tag{5.40}$$

When the reaction rate of the steam methane reforming is described by Eq. (5.38), the function f should meet the physical requirement of the equation form, that is, $f = 1$ when the ammonia supply is zero and $f = 0$ when the supplied gas is only ammonia. To be consistent with these physical requirements, we changed Eq. (5.40) to Eq. (5.41).

$$\theta_{\mathrm{H_2O,\,YSZ}} \approx \frac{K_{\mathrm{H_2O}} P_{\mathrm{H_2O}}}{K_{\mathrm{H_2O}} P_{\mathrm{H_2O}} + K_{\mathrm{NH_3}} P_{\mathrm{NH_3}}} \tag{5.41}$$

In addition, since there is no information of the absolute value of adsorption constants on YSZ, it is not reasonable to estimate them. Here, what is important is the relativity of the adsorption strength of steam and ammonia on YSZ surface. Therefore, we define the ratio of adsorption constant of steam $K_{\mathrm{H2O,\,YSZ}}$ to adsorption constant of ammonia $K_{\mathrm{NH3,\,YSZ}}$ as a relative value of adsorption constants $K_{\mathrm{rel\_H2O\text{-}NH3,\,YSZ}}$. Then, the function f can be described as follows;

$$f\left(\theta_{\mathrm{H_2O,\,YSZ}}\right) = \frac{P_{\mathrm{H_2O}}}{P_{\mathrm{H_2O}} + K_{\mathrm{rel\_H_2O\text{-}NH_3,\,YSZ}} P_{\mathrm{NH_3}}} \tag{5.42}$$

5.3 Numerical Model

To be compared with the experimental data presented in Chapter 3, a 1-D simulation model is developed which represents the test section of the experiment. The reaction models proposed in the above sections are implemented.

5.3.1 Problem Statement and Assumptions

Fig. 5.1 shows the schematic diagram of the 1-D model of the test section in Chapter 3. $X_{i,j}$ is the mole fraction of species j in the cell i, and T_i is the temperature of the cell i. The geometry of grids in the calculation are described in Table 5.2. The microstructure of the Ni–YSZ catalyst is given as shown in Table 3, referring to the experimental measurement [53]. V_{cat} and V_{rea} in Eq. (5.44) are the volume of the catalyst and test section, respectively. W_{cat} and ρ_{cat} in Eq. (5.45) denote the weight and density of the catalyst, respectively.

$$\varepsilon = 1.0 - \frac{V_{\mathrm{cat}}}{V_{\mathrm{rea}}} \tag{5.43}$$

$$V_{\mathrm{cat}} = \frac{W_{\mathrm{cat}}}{\rho_{\mathrm{cat}}} \tag{5.44}$$

$$V_{\mathrm{rea}} = \frac{\pi \times d^2 \times L}{4} \tag{5.45}$$

In the test section, the packed catalyst is modeled as a porous body. To calculate the reforming/decomposition reactions through the porous catalyst, following assumptions are made:

1. Steady state.
2. Uniform flow only for x direction.
3. No pressure drop. (The effect of the porous catalyst for flow is not assumed)
4. Gases and catalyst are the same temperature. (Thermal equilibrium state)
5. Streamwise mass diffusion is negligible.

6. Porous catalyst is isotropic and homogeneous.

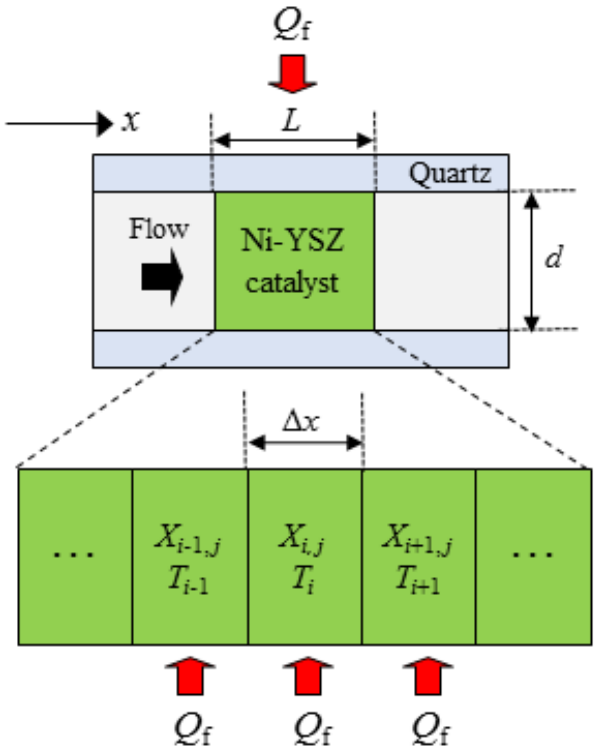

Fig. 5.1 Schematic of the 1-D model representing the test section in Chapter 3.

Table 5.2 Model geometry.

	Catalyst length L	Quartz tube inner diameter d
Size [mm]	2.8	7.0
Number of grids	1.0×10^3	–

Table 5.3 Microstructure parameters of Ni–YSZ catalyst.

Parameter	Value
Porosity ε [-]	0.544
Ni–Pore contact area density $S'_{\text{Ni-Pore}}$ [m^2 m^{-3}]	5.57×10^4

5.3.2 Governing Equations

In this simulation, following equations are considered to describe the phenomena.

1. Continuity equation

$$\frac{\partial}{\partial x}(\rho v) = 0 \tag{5.46}$$

2. Energy equation

$$\rho v C_p \frac{\partial T}{\partial x} = \frac{\partial}{\partial x}\left(\lambda \frac{\partial T}{\partial x}\right) + Q \tag{5.47}$$

3. Mass transfer equation

$$\rho v \frac{\partial M_j X_j}{\partial x} = S_j \tag{5.48}$$

where ρ is the density of the mixed gas, v is the velocity of the flow, C_p is the molar heat capacity, λ is the effective thermal conductivity, Q is the source term for heat transfer, M_j is the molar mass of each species j, X_j is the mole fraction of each species j, and S_j is the source term for mass transfer.

5.3.3 Physical Properties

The properties of the mixed gas vary depending on its temperature and composition.

Density

Density of the mixed gas can be calculated based on the ideal gas law as follows;

$$\rho = \frac{P\bar{M}}{R_0 T} \tag{5.49}$$

where $\bar{M}$ is the average molar mass.

Effective molar heat capacity at constant pressure

Molar heat capacity of the mixed gas can be calculated with the heat capacity of each component gas.

$$C_{\mathrm{p}} = \sum_j Y_j C_{\mathrm{p}j} \tag{5.50}$$

where Y_j is the mass fraction of each species. Heat capacity of each component gas is given as a function of temperature based on the property data [54].

Viscosity

Viscosity of the mixed gas can be calculated by the semi-empirical model that includes viscosity of each component gas [55].

$$\mu = \sum_j \left(\frac{X_j \mu_j}{\sum_k X_k \Phi_{j,k}} \right) \tag{5.51}$$

Viscosity of each component gas can be obtained as a function of temperature. $\Phi_{j,k}$ is a dimensionless number calculated by a semi-empirical Bromley and Wilke equation as follows [56];

$$\Phi_{j,k} = \frac{1}{\sqrt{8}} \left(1 + \frac{M_j}{M_k} \right)^{-\frac{1}{2}} \left[1 + \left(\frac{\mu_j}{\mu_k} \right)^{\frac{1}{2}} \left(\frac{M_k}{M_j} \right)^{\frac{1}{4}} \right]^2 \tag{5.52}$$

Effective thermal conductivity

Effective thermal conductivity of the mixed gas can be calculated by the semi-empirical model that includes thermal conductivity of each component gas [55].

$$\lambda = \sum_j \left(\frac{X_j \lambda_j}{\sum_k X_k \Phi_{j,k}} \right) \tag{5.53}$$

where λ_j is given as a function of temperature based on the property data [54].

In this numerical model, it is assumed that the gas and solid phase in the flow go to thermal equilibrium immediately. Therefore, the heat transfer between gas and solid phase can be represented by the effective thermal conductivity of the gas and solid. The effective thermal conductivity of the porous media is given by Eq. (5.54). The value ϕ is a constant which is determined by the ratio of thermal conductivity of mixed gas to that of solid, and ϕ = 0.040 is adopted [57].

$$\lambda_{\mathrm{eff}} = \lambda_{\mathrm{gas}} \times \left\{ \varepsilon + \frac{(1-\varepsilon)}{\phi + \frac{2}{3} \times \frac{\lambda_{\mathrm{gas}}}{\lambda_{\mathrm{cat}}}} \right\} \tag{5.54}$$

where the thermal conductivity of Ni–YSZ is assumed 11.0 W m^{-1} K^{-1} regardless of the temperature.

5.3.4 Source Terms

The source terms for the mass transfer equation expressed by Eq. (5.48), S_j, are associated with the generation and consumption of the gas species participating the steam methane reforming, $S_{\mathrm{SMR},j}$, water–gas shift reaction, $S_{\mathrm{WGS},j}$, and ammonia decomposition, $S_{\mathrm{ADC},j}$. Seven mass transfer equations corresponding to CH_4, H_2O, H_2, CO, CO_2, NH_3 and N_2 are solved.

The source term of energy equation Q consists of reaction heats of steam methane reforming Q_{SMR}, ammonia decomposition Q_{ADC}, water–gas shift reaction Q_{WGS} and the radiant heat from the electric furnace Q_{f}, as shown in Eq. (5.55). The reaction heat of each reaction can be calculated by Eqs. (5.56) to (5.58). $S'_{\text{Ni-Pore}}$ is the total area of Ni facing the pores in the catalyst [53]. F_{WGS} denotes the reaction amount of water–gas shift reaction, while ΔH_{SMR}, ΔH_{ADC}, and ΔH_{WGS} are the enthalpy changes by the steam methane reforming, ammonia decomposition and water–gas shift reaction, respectively. T_{fur} and T denote the temperature of the electric furnace and the mixed gas, respectively. Here, the emissivity of the catalyst α was set at 0.98. σ denotes the Stefan-Boltzmann constant.

$$Q = Q_{\mathrm{SMR}} + Q_{\mathrm{ADC}} + Q_{\mathrm{WGS}} + Q_{\mathrm{f}} \tag{5.55}$$

$$Q_{\mathrm{SMR}} = S'_{\mathrm{Ni-Pore}} R_{\mathrm{SMR}} \Delta H_{\mathrm{SMR}} \tag{5.56}$$

$$Q_{\mathrm{ADC}} = S'_{\mathrm{Ni-Pore}} R_{\mathrm{ADC}} \Delta H_{\mathrm{ADC}} \tag{5.57}$$

$$Q_{\mathrm{WGS}} = F_{\mathrm{WGS}} \Delta H_{\mathrm{WGS}} \tag{5.58}$$

$$Q_{\mathrm{f}} = \frac{\alpha\sigma\left(T_{\mathrm{fur}}^4 - T^4\right)}{V_{\mathrm{cat}}} \tag{5.59}$$

5.3.5 Fitting Experimental Data

In this analysis, the experimental data reported in Chapter 3 is used for fitting the parameters of the proposed reaction model. Table 5.4 summarizes the experimental conditions used for the fitting. The parameters to be fitted are shown in Table 5.5. For the steam methane reforming, the constant a in Eq. (5.38), the forward and backward reaction constants: k^+ and k^- are fit. Note that the reaction rate constants, shown in Eqs. (5.21) and (5.22), have temperature dependence. Therefore, the values of frequency factors and activation energies for both forward and backward reactions ($A_{SMR}{}^+$, $A_{SMR}{}^-$, $\Delta E_{SMR}{}^+$, and $\Delta E_{SMR}{}^-$) are fit. For the ammonia decomposition, the constant b in Eq. (5.23), the forward and backward reaction constants: k^+ and k^- ($A_{ADC}{}^+$, $A_{ADC}{}^-$, $\Delta E_{ADC}{}^+$, and $\Delta E_{ADC}{}^-$), the enthalpy and entropy changes of ammonia caused by adsorption, $\Delta H_{ad\_NH3,\ Ni}$ and $\Delta S_{ad\_NH3,\ Ni}$, and the relative value of adsorption constants $K_{rel\_H2O\text{-}NH3,\ YSZ}$, which represents the effect of YSZ as a catalyst support are fitted. The fitting calculation is to minimize the root mean square of the deviation between the experimental data and numerical results, as shown in Eq. (5.60).

$$RMS = \sqrt{\frac{1}{N}\sum_l^N \left(x_{j,\,\mathrm{EXP},\,l} - x_{j,\,\mathrm{SIM},l}\right)^2} \tag{5.60}$$

where N is the number of the experimental conditions, species j denotes either CH_4 or NH_3, and $x_{j,\,EXP,\,l}$ and $x_{j,\,SIM,\,l}$ denote the conversion rates of experiment and simulation of species j, respectively.

Table 5.4 Experimental conditions.

Fuel	No.	F_{CH4} [sccm]	F_{H2O} [sccm]	F_{NH3} [sccm]	T [°C]
Mixed	144	20 / 40 / 50 / 60	100	4 / 6 / 8 / 10 / 15 / 20 / 30 / 40 / 60	600 / 650 / 700 / 750

Table 5.5 Fitting parameters.

Reaction	Reaction rate constant k^+ and k^- (A^+, A^-, ΔE^+,*and* ΔE^-)	Sequential association representing value a or b	Adsorption constant K_{NH3} ($\Delta H_{ad\_NH3,Ni}$, $\Delta S_{ad\_NH3,\ Ni}$)	Relative adsorption constant $K_{rel\_H2O\text{-}NH3,\ YSZ}$ (A_{rel} and ΔE_{rel})
Steam methane reforming	✓	✓	–	✓
Ammonia decomposition	✓	✓	✓	–

5.4 Results and Discussion

To verify our proposed model and its reaction rate expressions, the experimental data of the mixed fuel reported in Chapter 3 are numerically fit. Fit parameters for each reaction are shown in Table 5.5.

5.4.1 Steam Methane Reforming under Mixed Condition

The reaction rate model of the steam methane reforming when the mixed fuel is supplied is described by Eq. (5.38). As discussed in the section 5.2.2, the reaction rate constants of the steam methane reforming reaction, both forward one and backward one, are functions of temperature which can be described by the Arrhenius type equations. Therefore, in the fitting process, the reaction rate constants are fit to the Arrhenius model. As shown in Table 5.5, the reaction rate constants k_{SMR}^{+} and k_{SMR}^{-} (A_{SMR}^{+}, A_{SMR}^{-}, ΔE_{SMR}^{+}, and ΔE_{SMR}^{-}), relative adsorption constant $K_{rel\_H2O\text{-}NH3,\ YSZ}$ (A_{rel} and ΔE_{rel}), the sequential association representing value a are the parameters to be fit. As summarized in Table 5.4, one hundred and forty four experimental data with different temperatures and concentrations of methane and ammonia are used.

Fig. 5.2 shows the methane reforming rate as a function of a concentration of ammonia in the mixed fuel when the inlet fuel is 700 °C. When the reaction rate constants $k_{SMR}^{+}=1.13\times10^{20}\exp(-1.46\times10^{5}/RT)$, $k_{SMR}^{-}=5.00\times10^{24}\exp(-3.12\times10^{5}/RT)$, the relative adsorption constant $K_{rel\_H2O\text{-}NH3,\ YSZ}=5.55\times10^{-10}\exp(-2.6419\times10^{5}/RT)$, and the sequential association representing value a=5, the RMS value defined by Eq. (5.60) reaches minimum. The simulation model successfully reproduces the results of the experiments. Note that the value of a reaches 5, which indicates that the probability of sequential reactions of hydrogen dissociation from methane is equivalent to the probability of association of five neighboring vacant sites.

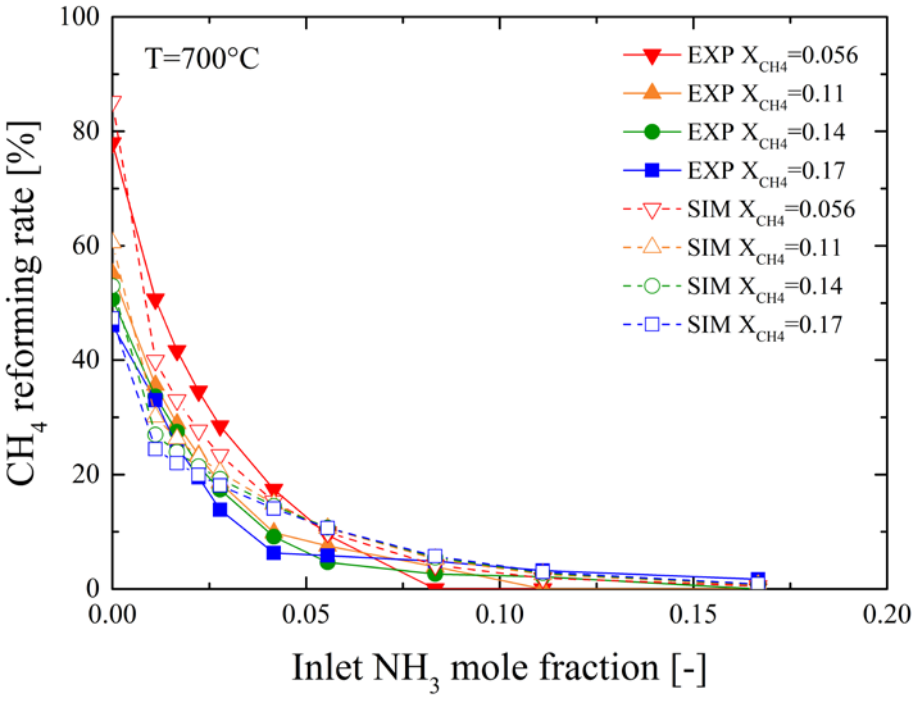

Fig. 5.2 Fit results of Methane reforming rate at 700 °C.

5.4.2 Ammonia Decomposition under Mixed Condition

The reaction rate model of the ammonia decomposition when the mixed fuel is supplied is described by Eq. (5.28). As the steam methane reforming, the reaction rate constants of the ammonia decomposition can be described by the Arrhenius type equations. Therefore, in the fitting process, the reaction rate constants are fit to the Arrhenius model. As summarized in Table 5.5, the reaction rate constants k_{ADC}^{+} and k_{ADC}^{-} (A_{ADC}^{+}, A_{ADC}^{-}, ΔE_{ADC}^{+}, and ΔE_{ADC}^{-}), the enthalpy and entropy changes of ammonia caused by adsorption, $\Delta H_{ad\_NH3,\,Ni}$ and $\Delta S_{ad\_NH3,\,Ni}$, and the sequential association representing values b are the parameters to be fit. One hundred and forty four experimental data with different temperatures and concentrations of methane and ammonia, which are also used to make the fitting of the reforming rate calculation, are employed.

Fig. 5.3 shows the ammonia decomposition rate as a function of a concentration of ammonia in the mixed fuel when the inlet fuel is 700 °C. When the reaction rate constants $k_{ADC}^{+}=1.50\times10^{4}\exp(-1.00\times10^{5}/RT)$, $k_{ADC}^{-}=5.00\times10^{25}\exp(-3.12\times10^{5}/RT)$, the enthalpy and entropy changes $\Delta H_{ad\_NH3,\ Ni}=-9$ kJ mol^{-1} and $\Delta S_{ad\_NH3,\ Ni}=0$ J mol^{-1} K^{1}, and the sequential association representing value $b=3$, the RMS value defined by Eq. (5.60) reaches minimum. The simulation model successfully reproduces the results of the experiments. Note that the value of b reaches 3, which indicates that the probability of sequential reactions of hydrogen dissociation from ammonia is equivalent to the probability of association of three neighboring vacant sites. The changes of enthalpy $\Delta H_{ad\_NH3,\ Ni}=-9$ kJ mol^{-1} and entropy $\Delta S_{NH3,\ Ni}=0$ J mol^{-1} K^{-1} can be considered reasonable values referring to the report which studies the adsorption phenomena of other materials [47,58–60].

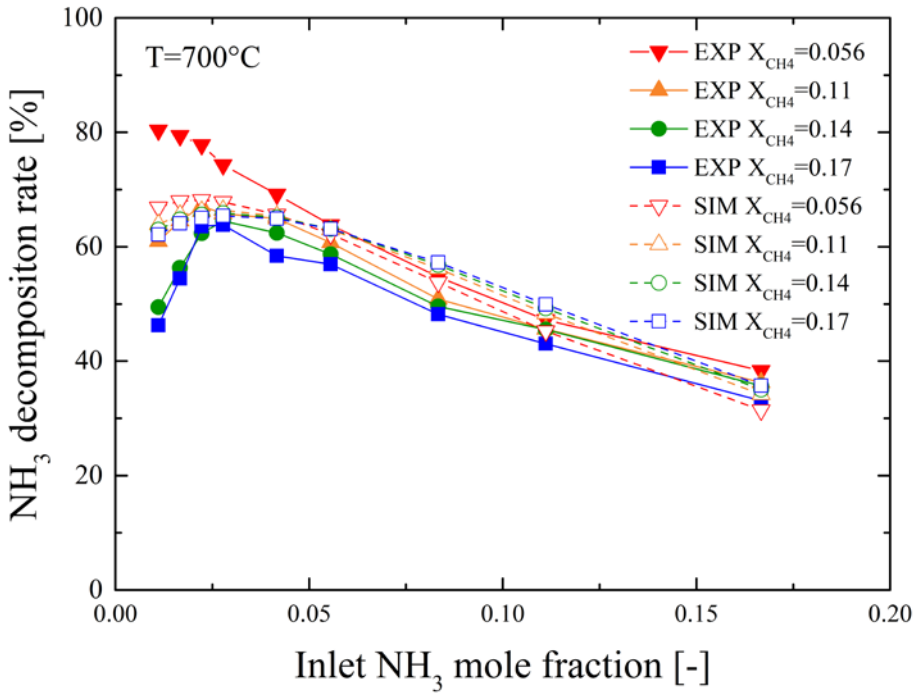

Fig. 5.3 Fit results of Ammonia decomposition rate at 700 °C

5.4.3 Temperature Dependency of the Proposed Model

Fig. 5.4, Fig. 5.5, and Fig. 5.6 are the fit results of the mixed fuel when the temperature is at 750, 650, and 600 °C, respectively. In all cases, it can be confirmed that the simulation results successfully reproduce the experimental results, as the case at 700 °C.

Figs. 5.7 and 5.8 show the temperature dependence of the reaction rates constants of the steam methane reforming and the ammonia decomposition reactions, both forward and backward ones. It is confirmed that their temperature dependence clearly fit on the Arrhenius plot. Note that the simulation results shown in Figs. 5.2 to 5.6 already adopted the reaction rate constants as a function of temperature shown in Figs. 5.7 and 5.8.

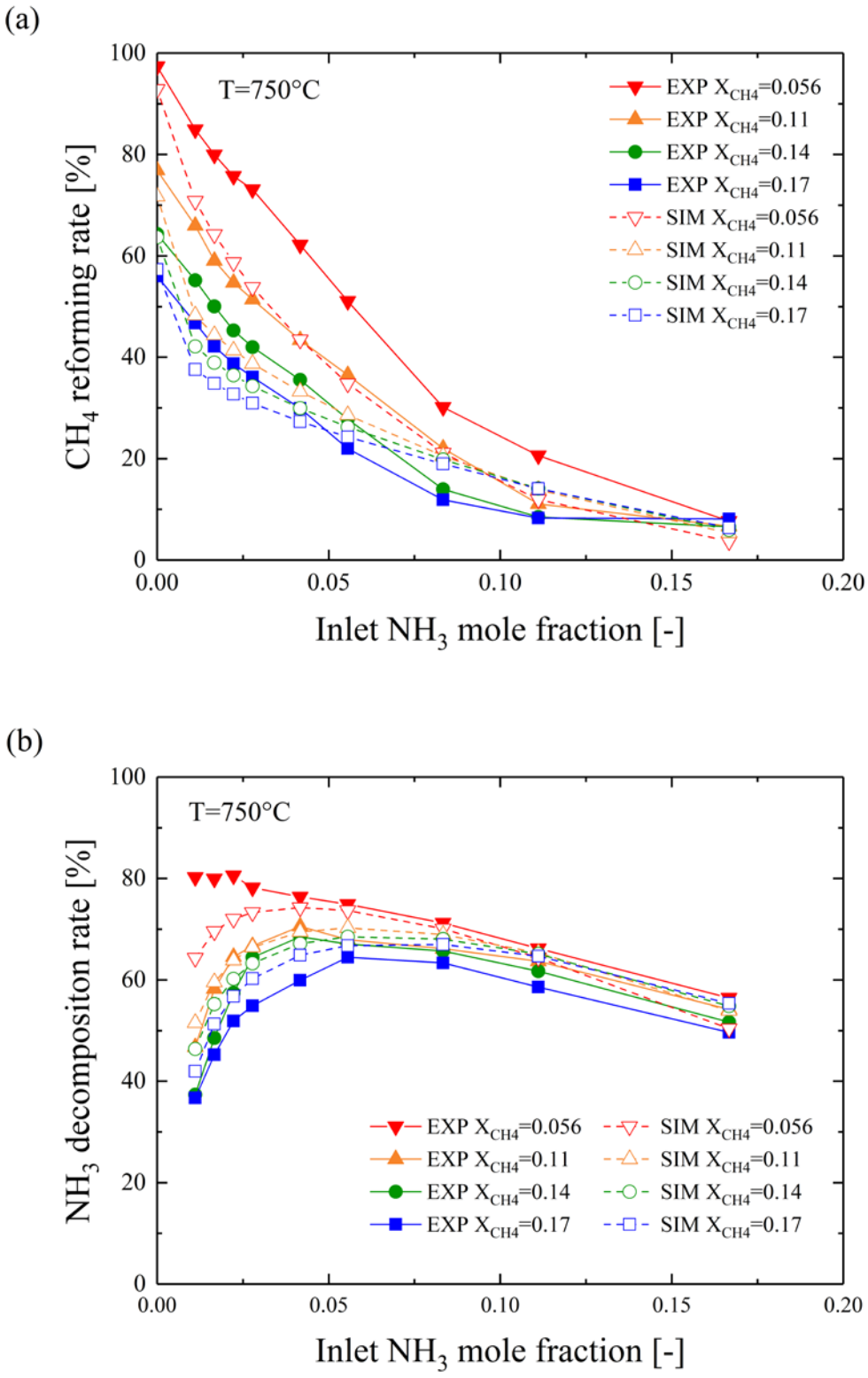

Fig. 5.4 Fit results at 750 °C.
(a) Methane reforming rate and (b) ammonia decomposition rate.

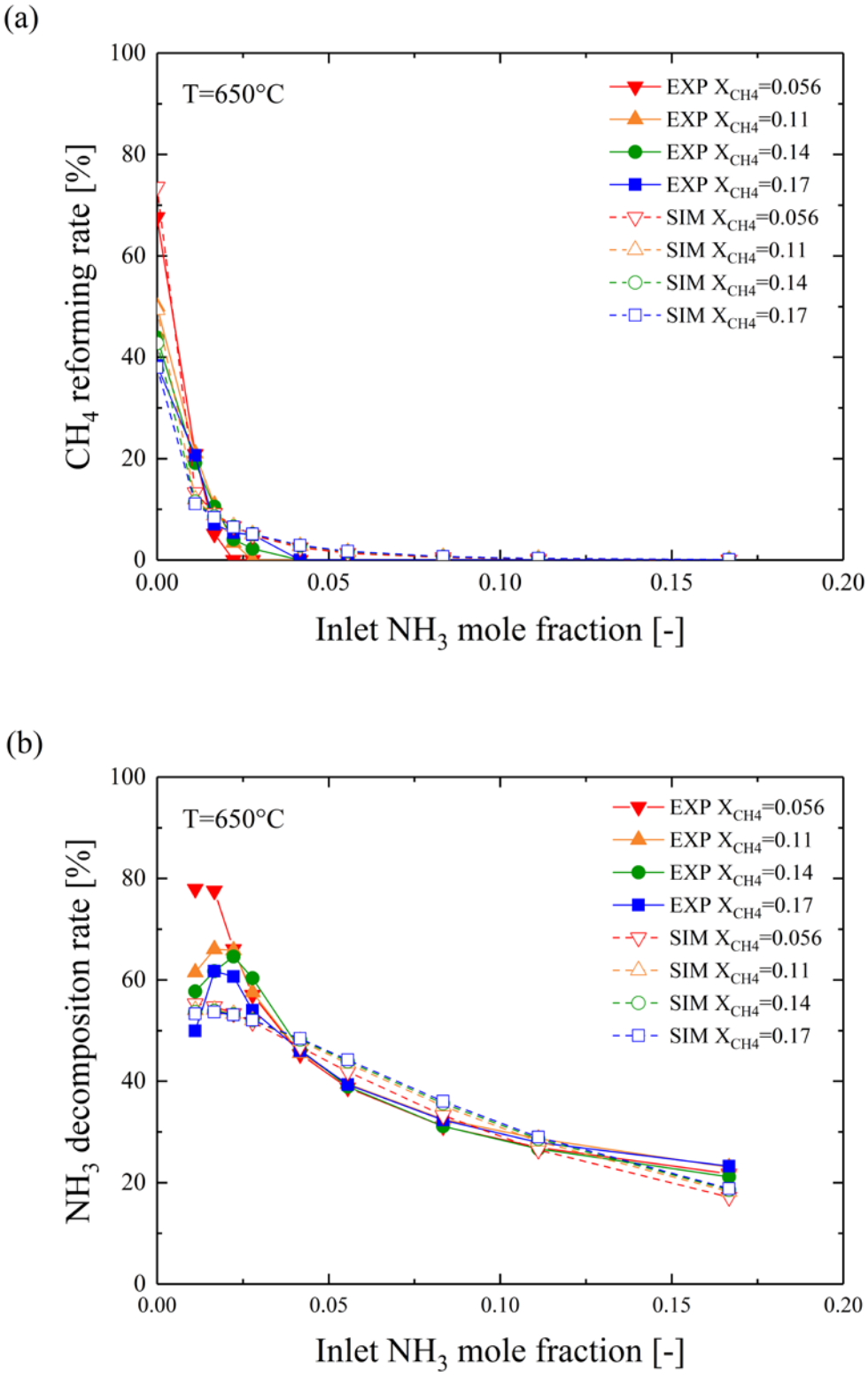

Fig. 5.5 Fit results at 650 °C.
(a) Methane reforming rate and (b) ammonia decomposition rate.

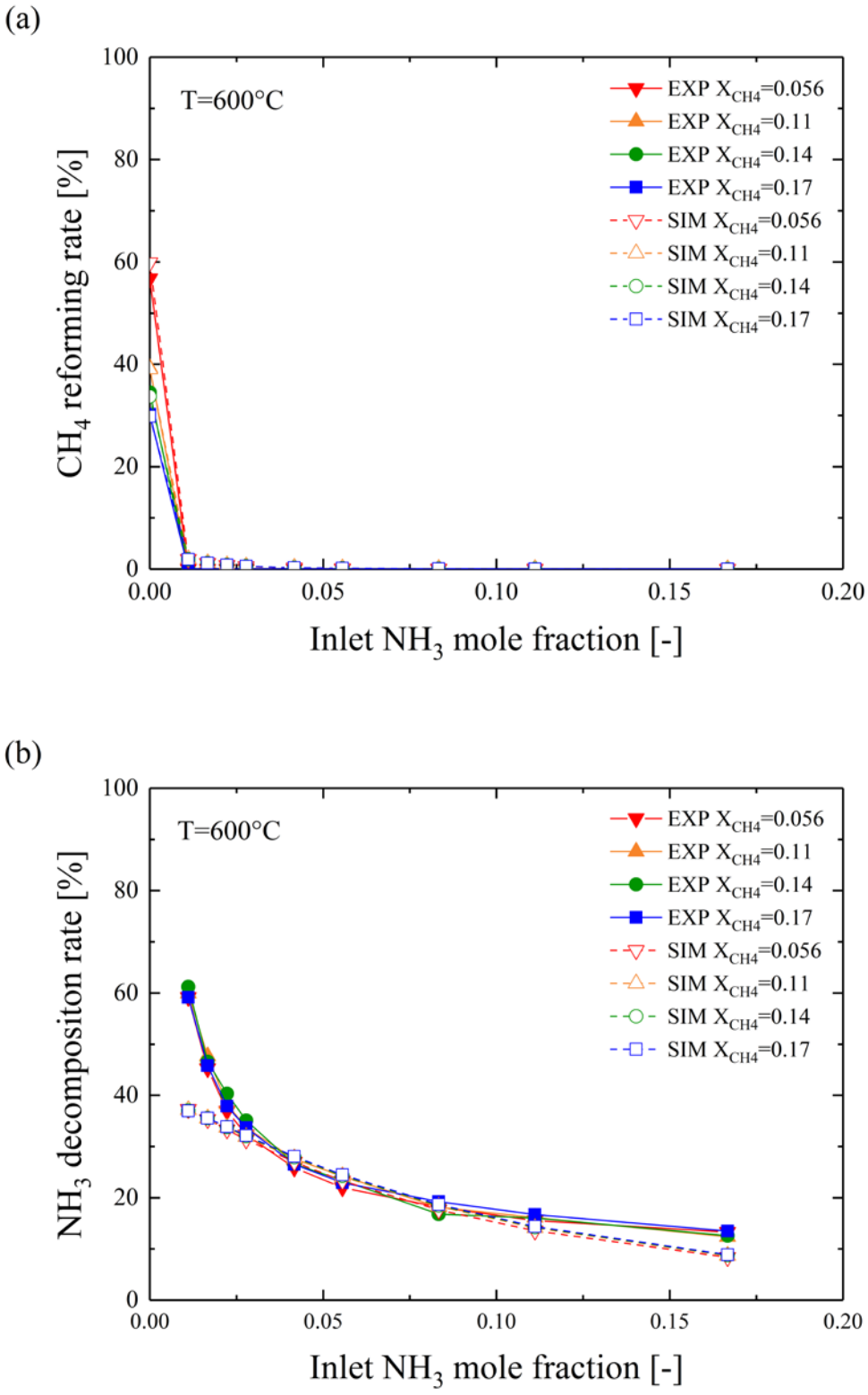

Fig. 5.6 Fit results at 600 °C.
(a) Methane reforming rate and (b) ammonia decomposition rate.

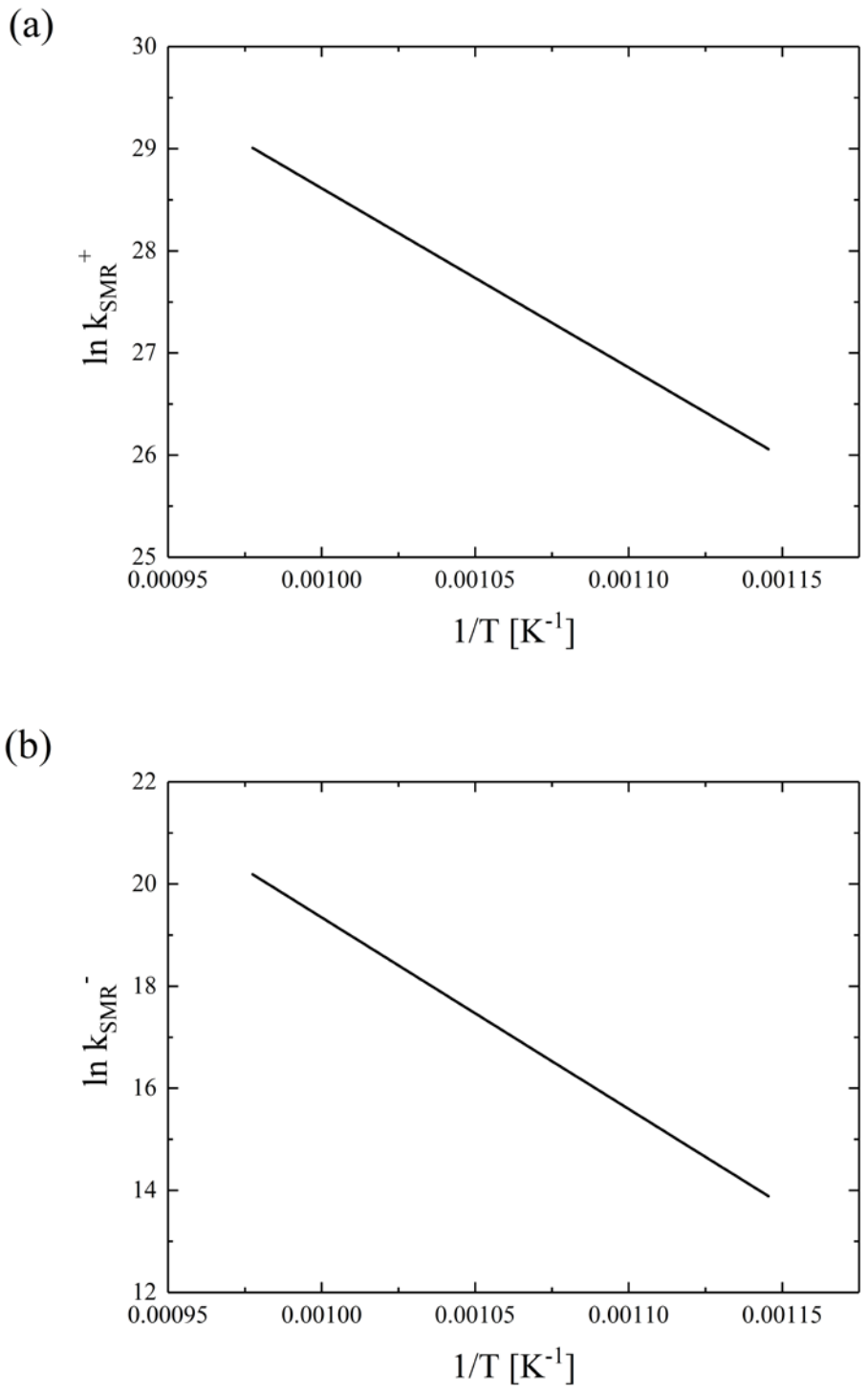

Fig. 5.7 Temperature dependence of reaction rate constants of steam methane reforming. (a) Forward reaction $k_{SMR}{}^{+}$ and (b) backward reaction $k_{SMR}{}^{-}$.

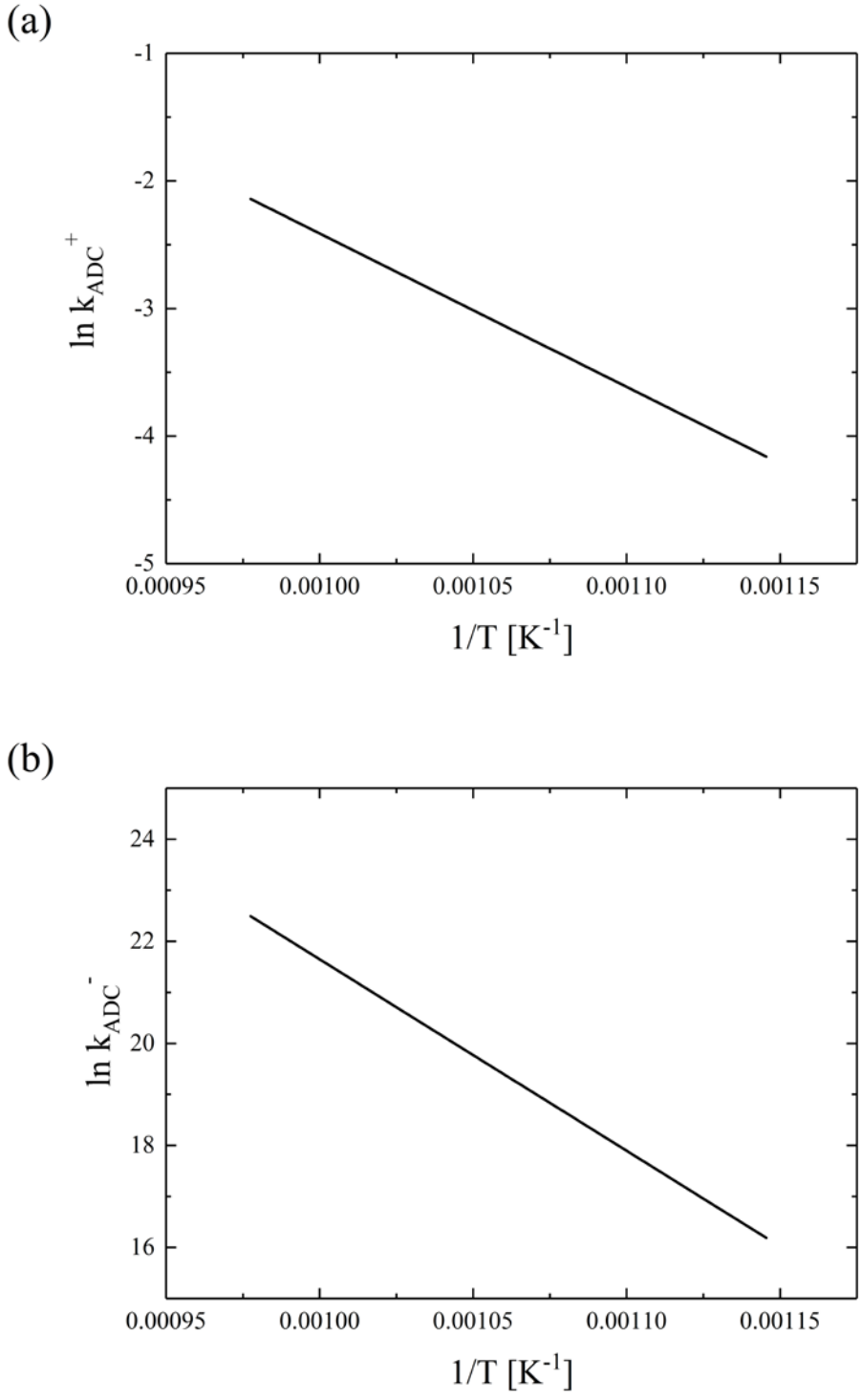

Fig. 5.8 Temperature dependence of reaction rate constants of ammonia decomposition. (a) Forward reaction $k_{ADC}{}^{+}$ and (b) backward reaction $k_{ADC}{}^{-}$.

5.4.4 Reaction Rate Formulae under Mixed Condition

The parameters obtained by the fitting calculation are shown in Table 5.6. The final results of reaction rate formulae of the steam methane reforming and ammonia decomposition reactions on the basis of our model are expressed as follows;

$$R_{\mathrm{SMR}} = 1.13 \times 10^{20} \exp\left(-\frac{1.46\times10^{5}}{RT}\right) \theta_{\mathrm{CH_4}} f\left(\theta_{\mathrm{H_2O,\,YSZ}}\right) \theta_{\mathrm{H_2O}} {\theta_{\mathrm{V}}}^{5} - 5.00 \times 10^{24} \exp\left(-\frac{3.12\times10^{5}}{RT}\right) {\theta_{\mathrm{H}}}^{6} \theta_{\mathrm{CO}} \quad (5.61)$$

$$R_{\mathrm{ADC}} = 1.50 \times 10^{4} \exp\left(-\frac{1.00\times10^{5}}{RT}\right) \theta_{\mathrm{NH_3}} {\theta_{\mathrm{V}}}^{3} - 5.00 \times 10^{25} \exp\left(-\frac{3.12\times10^{5}}{RT}\right) {\theta_{\mathrm{H}}}^{3} \theta_{\mathrm{N}} \quad (5.62)$$

where the coverage value of each species is expressed from Eq. (5.27) to (5.34), the adsorption constant of each species is expressed by Eq. (5.37) with using the enthalpy and entropy changes shown in Table. 5.1 and our fit results ($\Delta H_{\mathrm{ad\_NH3,\,Ni}}$=–9 kJ mol^{-1} and $\Delta S_{\mathrm{ad\_NH3,\,Ni}}$=0 J mol^{-1} K^{-1}), and the function f which represents the relative adsorption effect on YSZ is described by Eq. (5.42).

Table 5.6 Parameters obtained from fitting calculation.

	Steam methane reforming	Ammonia decomposition
Reaction rate constants	$A_{\mathrm{SMR}}{}^{+}$ = 1.13E+20	$A_{\mathrm{ADC}}{}^{+}$ = 1.50E+04
	$E_{\mathrm{SMR}}{}^{+}$ = 1.46E+05	$E_{\mathrm{ADC}}{}^{+}$ = 1.00E+05
	$A_{\mathrm{SMR}}{}^{-}$ = 5.00E+24	$A_{\mathrm{ADC}}{}^{-}$ = 5.00E+25
	$E_{\mathrm{SMR}}{}^{-}$ = 3.12E+05	$E_{\mathrm{ADC}}{}^{-}$ = 3.12E+05
Sequential association representing value	a = 5	b = 3
Adsorption constant	–	$\Delta H_{\mathrm{ad\_NH3,\,Ni}}$ = –9 kJ mol^{-1}
	–	$\Delta S_{\mathrm{ad\_NH3,\,Ni}}$ = 0 J mol^{-1} K^{-1}
Relative adsorption constant	$K_{\mathrm{rel\_H2O\text{-}NH3,\,YSZ}}$ = 5.55E–10 exp(26419/T)	–

5.4.5 Validity of the Model of Catalyst Support

As discussed in section 5.2.4, it is predicted that the catalyst support, namely YSZ, gives some effect on steam methane reforming, thus, to describe it, we introduced the relative value of adsorption constants of ammonia to steam on the surface of YSZ: $K_{\text{rel\_H2O-NH3, YSZ}}$. To confirm the validity of the model, the temperature dependency of the relative adsorption constants $K_{\text{rel\_H2O-NH3, YSZ}}$ is examined. Furthermore, the calculation without the model is conducted to confirm the effect of the model in the simulation.

5.4.5.1 Temperature Dependence of Relative Adsorption Constant

As discussed in section 5.2.4, the relative adsorption constant should be represented by Arrhenius type equation because both adsorption constants of steam and ammonia follow the Arrhenius equations. By fitting the experimental results with four different inlet temperatures, we succeeded in obtaining the temperature dependence of relative adsorption constant $K_{\text{rel\_H2O-NH3, YSZ}}$, as shown in Eq. (5.75).

$$K_{\text{rel\_H2O-NH3, YSZ}} = 5.55 \times 10^{-10} \exp\left(-\frac{2.6419\times10^{5}}{RT}\right) \tag{5.75}$$

where R denotes the ideal gas constant. The figure is shown in Fig. 5.9.

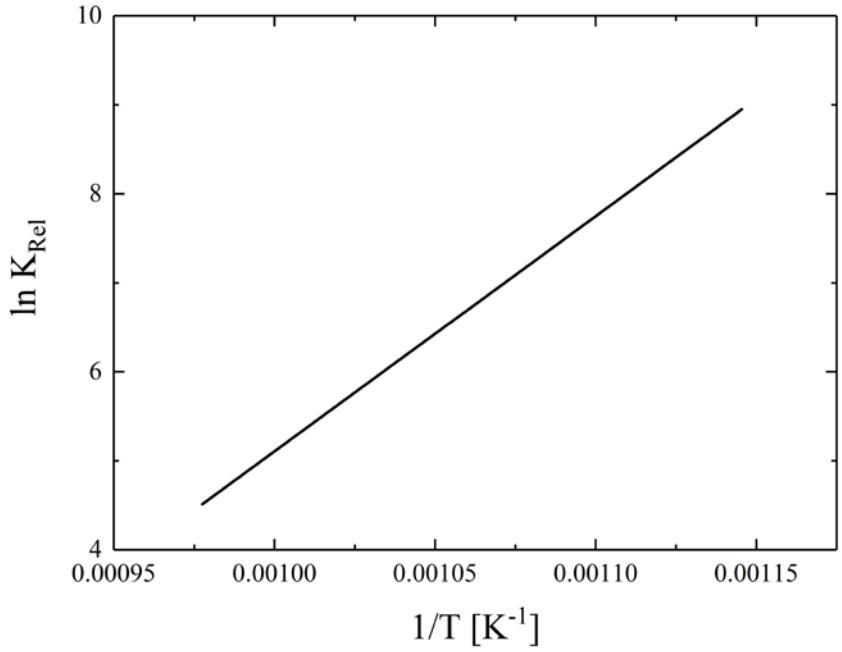

Fig. 5.9 Temperature dependence of relative adsorption constant $K_{rel\_H2O\text{-}NH3,\ YSZ}$.

5.4.5.2 Comparison with and without the Relative Adsorption Model

Fig. 5.10 shows the simulation results without the relative adsorption model when the inlet temperature is 700 °C. As clearly shown in Fig. 5.10 (a), even if the concentration of ammonia in the mixed fuel is increased, the reforming rates of methane in all conditions do not decrease sufficiently as the case with the relative adsorption model, shown in Fig. 5.3. On the other hand, the decomposition rates of ammonia have little changes. This indicates that the ammonia adsorption on YSZ support plays an important role in the reaction rates of steam methane reforming when the mixed fuel is supplied to Ni–YSZ catalyst.

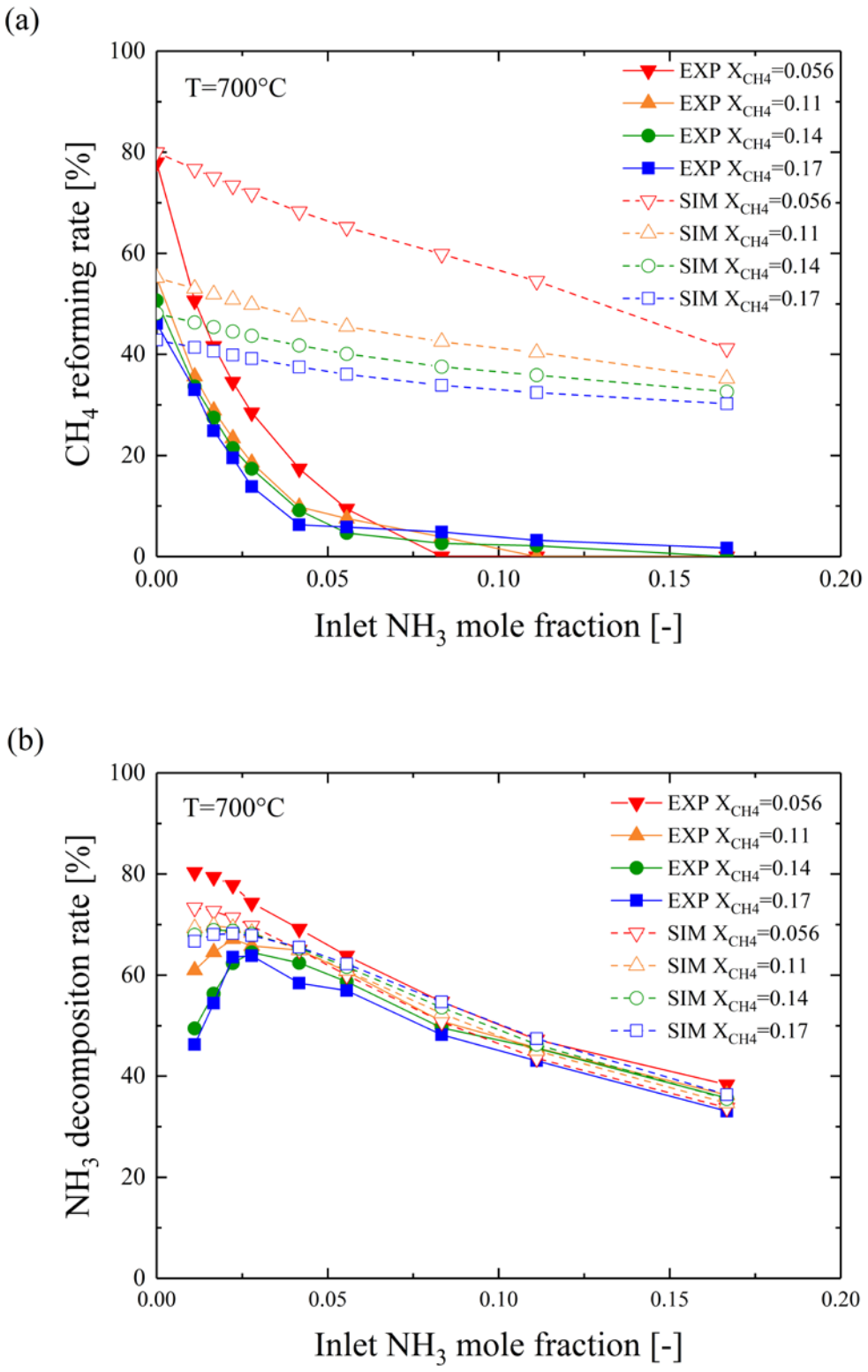

Fig. 5.10 Fit results without the relative adsorption model at 700 °C.
(a) Methane reforming rate and (b) ammonia decomposition rate.

5.5 Conclusions

To describe the reaction phenomena of the mixed fuel of methane and ammonia on the Ni–YSZ catalyst, a reaction model is proposed. The model includes the adsorption constants of conceivable chemical species to describe the competitive adsorption condition in the mixed fuel, on the other hand, it does not get into the elementary reaction model, which makes the model computationally friendly and applicable even to a larger scale simulation. The model also considers the effect of catalyst support, namely YSZ, on the rate of steam methane reforming.

By fitting the experimental data to the model, the reaction rate formulae of the steam methane reforming and ammonia decomposition that can describe the mixed fuel condition are successfully introduced. The new reaction rate formulae can reproduce the all experimental results which are obtained at different temperatures and different mixture compositions. This indicates that the new formulae can be regarded as more general expressions of the reaction rates compared to the equations reported so far and can be applicable to all kinds of numerical simulations. It was also found that YSZ, the catalyst support, gives some effect on the rate of steam methane reforming. The comprehensive study of the effect of a catalyst support on the reforming rate is expected to fully understand the phenomena.

Bibliography

1. Achenbach E, Riensche E. Methane/steam reforming kinetics for solid oxide fuel cells. *J Power Sources*. 1994;52(2):283-288. doi:10.1016/0378-7753(94)02146-5
2. Achenbach E. Three-dimensional and time-dependent simulation of a planar solid oxide fuel cell stack. *J Power Sources*. 1994;49(1-3):333-348. doi:10.1016/0378-7753(93)01833-4
3. Laosiripojana N, Assabumrungrat S. Catalytic steam reforming of methane, methanol, and ethanol over Ni/YSZ: The possible use of these fuels in internal reforming SOFC. *J Power Sources*. 2007;163(2):943-951. doi:10.1016/j.jpowsour.2006.10.006
4. Lo Faro M, La Rosa D, Monforte G, Antonucci V, Arico AS, Antonucci P. Propane conversion over a Ru/CGO catalyst and its application in intermediate temperature solid oxide fuel cells. *J Appl Electrochem*. 2007;37(2):203-208. doi:10.1007/s10800-006-9245-5
5. Huang TJ, Wu CY, Wang CH. Fuel processing in direct propane solid oxide fuel cell and carbon dioxide reforming of propane over Ni–YSZ. *Fuel Process Technol*. 2011;92(8):1611-1616. doi:10.1016/j.fuproc.2011.04.007
6. Lo Faro M, La Rosa D, Nicotera I, Antonucci V, Aricò AS. Electrochemical investigation of a propane-fed solid oxide fuel cell based on a composite Ni–perovskite anode catalyst. *Appl Catal B Environ*. 2009;89(1-2):49-57. doi:10.1016/j.apcatb.2008.11.019
7. Alphonse P, Ansart F. Catalytic coatings on steel for low-temperature propane prereforming to solid oxide fuel cell (SOFC) application. *J Colloid Interface Sci*. 2009;336(2):658-666. doi:10.1016/j.jcis.2009.04.079
8. Chen F, Zha S, Dong J, Liu M. Pre-reforming of propane for low-temperature SOFCs.

Solid State Ionics. 2004;166(3-4):269-273. doi:10.1016/j.ssi.2003.12.004

9. Jiang Y, Virkar A V. A High Performance, Anode-supported solid oxide fuel cell operating on direct alcohol. *J Electrochem Soc*. 2001;148(7):A706. doi:10.1149/1.1375166

10. Liu M, Peng R, Dong D, Gao J, Liu X, Meng G. Direct liquid methanol-fueled solid oxide fuel cell. *J Power Sources*. 2008;185(1):188-192. doi:10.1016/j.jpowsour.2008.06.076

11. Lo Faro M, Stassi A, Antonucci V, et al. Direct utilization of methanol in solid oxide fuel cells: An electrochemical and catalytic study. *Int J Hydrogen Energy*. 2011;36(16):9977-9986. doi:10.1016/j.ijhydene.2011.05.053

12. Jordão B, Sarruf M, Hong J, Steinberger-wilckens R, Emílio P, Miranda V De. CeO_2–Co_3O_4–CuO anode for direct utilisation of methane or ethanol in solid oxide fuel cells. *Int J Hydrogen Energy*. 2018;43:6340-6351. doi:10.13140/RG.2.2.13804.46721

13. Hong-xin YOU, Guo-dong GAO, Liang Z, Abudula A. Power generating performances of ethanol on the SOFC. *J Fuel Chem Technol*. 2010;38(1):116-120. doi:10.1016/S1872-5813(10)60023-0

14. Steil MC, Nobrega SD, Georges S, Gelin P, Uhlenbruck S, Fonseca FC. Durable direct ethanol anode-supported solid oxide fuel cell. *Appl Energy*. 2017;199(1):180-186. doi:10.1016/j.apenergy.2017.04.086

15. Farrell B, Linic S. Direct electrochemical oxidation of ethanol on SOFCs: Improved carbon tolerance of Ni anode by alloying. *Appl Catal B Environ*. 2016;183:386-393. doi:10.1016/j.apcatb.2015.11.002

16. Douvartzides SL, Coutelieris FA, Demin AK, Tsiakaras PE. Electricity from ethanol fed SOFCs: The expectations for sustainable development and technological benefits. *Int J Hydrogen Energy*. 2004;29(4):375-379. doi:10.1016/S0360-3199(03)00047-8

17. Thanomjit C, Patcharavorachot Y, Ponpesh P, Arpornwichanop A. Thermodynamic analysis of solid oxide fuel cell system using different ethanol reforming processes. *Int J Hydrogen Energy*. 2015;40(21):6950-6958. doi:10.1016/j.ijhydene.2015.03.155

18. Murray EP, Harris SJ, Jen H. Solid oxide fuel cells utilizing dimethyl ether fuel. *J Electrochem Soc*. 2002;149(9):A1127. doi:10.1149/1.1496484

19. Liu Y, Guo Y, Wang W, et al. Study on proton-conducting solid oxide fuel cells with a conventional nickel cermet anode operating on dimethyl ether. *J Power Sources*. 2011;196(22):9246-9253. doi:10.1016/j.jpowsour.2011.07.051

20. Su C, Ran R, Wang W, Shao Z. Coke formation and performance of an intermediate-temperature solid oxide fuel cell operating on dimethyl ether fuel. *J Power Sources*. 2011;196(4):1967-1974. doi:10.1016/j.jpowsour.2010.10.011

21. Laosiripojana N, Assabumrungrat S. Catalytic steam reforming of dimethyl ether (DME) over high surface area Ce-ZrO_2 at SOFC temperature: The possible use of DME in indirect internal reforming operation (IIR-SOFC). *Appl Catal A Gen*. 2007;320:105-113. doi:10.1016/j.apcata.2006.12.018

22. Homel M, Gür TM, Koh JH, Virkar A V. Carbon monoxide-fueled solid oxide fuel cell. *J Power Sources*. 2010;195(19):6367-6372. doi:10.1016/j.jpowsour.2010.04.020

23. Zhang H, Chen J, Zhang J. Performance analysis and parametric study of a solid oxide fuel cell fueled by carbon monoxide. *Int J Hydrogen Energy*. 2013;38(36):16354-16364. doi:10.1016/j.ijhydene.2013.09.144

24. Li C, Shi Y, Cai N. Carbon deposition on nickel cermet anodes of solid oxide fuel cells operating on carbon monoxide fuel. *J Power Sources*. 2013;225:1-8. doi:10.1016/j.jpowsour.2012.10.018

25. Inui Y, Urata A, Ito N, Nakajima T, Tanaka T. Performance simulation of planar SOFC using mixed hydrogen and carbon monoxide gases as fuel. *Energy Convers*

Manag. 2006;47(13-14):1738-1747. doi:10.1016/j.enconman.2005.10.014

26. Wojcik A, Middleton H, Damopoulos I, Van Herle J. Ammonia as a fuel in solid oxide fuel cells. *J Power Sources*. 2003;118(1-2):342-348. doi:10.1016/S0378-7753(03)00083-1

27. Molouk AFS, Okanishi T, Muroyama H, Matsui T, Eguchi K. Electrochemical and catalytic behaviors of Ni–YSZ anode for the direct utilization of ammonia fuel in solid oxide fuel cells. *J Electrochem Soc*. 2015;162(10):F1268-F1274. doi:10.1149/2.1011510jes

28. Okanishi T, Okura K, Srifa A, et al. Comparative study of ammonia-fueled solid oxide fuel cell systems. *Fuel Cells*. 2017;17(3):383-390. doi:10.1002/fuce.201600165

29. Janardhanan VM, Heuveline V, Deutschmann O. Performance analysis of a SOFC under direct internal reforming conditions. *J Power Sources*. 2007;172(1):296-307. doi:10.1016/j.jpowsour.2007.07.008

30. Peters R, Dahl R, Klüttgen U, Palm C, Stolten D. Internal reforming of methane in solid oxide fuel cell systems. *J Power Sources*. 2002;106(1-2):238-244. doi:10.1016/S0378-7753(01)01039-4

31. Aguiar P, Adjiman CS, Brandon NP. Anode-supported intermediate temperature direct internal reforming solid oxide fuel cell. I: Model-based steady-state performance. *J Power Sources*. 2004;138(1-2):120-136. doi:10.1016/j.jpowsour.2004.06.040

32. Liese EA, Gemmen RS. Performance comparison of internal reforming against external reforming in a Solid Oxide Fuel Cell, gas turbine hybrid system. *J Eng Gas Turbines Power*. 2005;127(1):86-90. doi:10.1115/1.1788689

33. Dicks AL. Advances in catalysts for internal reforming in high temperature fuel cells. *J Power Sources*. 1998;71(1-2):111-122. doi:10.1016/S0378-7753(97)02753-5

34. Iwai H, Yamamoto Y, Saito M, Yoshida H. Numerical simulation of intermediate-

temperature direct-internal-reforming planar solid oxide fuel cell. *Energy*. 2011;36(4):2225-2234. doi:10.1016/j.energy.2010.03.058

35. Wongchanapai S, Iwai H, Saito M, Yoshida H. Selection of suitable operating conditions for planar anode-supported direct-internal-reforming solid-oxide fuel cell. *J Power Sources*. 2012;204:14-24. doi:10.1016/j.jpowsour.2011.12.029
36. Bebelis S, Zeritis A, Tiropani C, Neophytides SG. Intrinsic kinetics of internal steam reforming of CH_4 over a Ni-YSZ-cermet catalyst-electrode. *Ind Eng Chem Res*. 2000;39(12):4920-4927.
37. Ahmed K, Foger K. Kinetics of internal steam reforming of methane on Ni/YSZ-based anodes for solid oxide fuel cells. *Catal Today*. 2000;63(2-4):479-487. doi:10.1016/S0920-5861(00)00494-6
38. Wang Y, Yoshiba F, Kawase M, Watanabe T. Performance and effective kinetic models of methane steam reforming over Ni/YSZ anode of planar SOFC. *Int J Hydrogen Energy*. 2009;34(9):3885-3893. doi:10.1016/j.ijhydene.2009.02.073
39. Lehnert W, Meusinger J, Thom F. Modelling of gas transport phenomena in SOFC anodes. *J Power Sources*. 2000;87:57-63.
40. Haberman BA, Young JB. Three-dimensional simulation of chemically reacting gas flows in the porous support structure of an integrated-planar solid oxide fuel cell. *Int J Heat Mass Transf*. 2004;47:3617-3629. doi:10.1016/j.ijheatmasstransfer.2004.04.010
41. Twigg MV. *Catalyst Handbook*. Wolfe Publishing LTD; 1989.
42. Nagasawa T, Hanamura K. Prediction of overpotential and effective thickness of Ni/YSZ anode for solid oxide fuel cell by improved species territory adsorption model. *J Power Sources*. 2017;353:115-122. doi:10.1016/j.jpowsour.2017.03.154
43. Herrera Delgado K, Maier L, Tischer S, Zellner A, Stotz H, Deutschmann O. Surface reaction kinetics of steam- and CO_2-reforming as well as oxidation of methane over

nickel-based catalysts. *Catalysts*. 2015;5(2):871-904. doi:10.3390/catal5020871

44. Appari S, Janardhanan VM, Jayanti S, Maier L, Tischer S, Deutschmann O. Micro-kinetic modeling of NH_3 decomposition on Ni and its application to solid oxide fuel cells. *Chem Eng Sci*. 2011;66(21):5184-5191. doi:10.1016/j.ces.2011.07.007

45. Rawls R. *Physical Chemistry*. Vol 58.; 1980. doi:10.1021/cen-v058n022.p020

46. Zhang J, Xu H, Li W. Kinetic study of NH_3 decomposition over Ni nanoparticles: The role of la promoter, structure sensitivity and compensation effect. *Appl Catal A Gen*. 2005;296(2):257-267. doi:10.1016/j.apcata.2005.08.046

47. Al-Shammeri KK, Saleh JM. Adsorption and decomposition of ammonia on metal films of nickel, palladium, tungsten, and aluminum. *J Phys Chem*. 1986;90(13):2906-2910. doi:10.1021/j100404a025

48. Igarashi A. Recent topics on production and use of hydrogen. *J Hydrog Energy Syst Soc Japan*. 2000;25(2):62-70.

49. OYAMA ST. Kinetics of ammonia decomposition on vanadium nitride. *J Catal*. 1992;133:358-369.

50. McCabe RW. Kinetics of ammonia decomposition on nickel. *J Catal*. 1983;79(2):445-450. doi:10.1016/0021-9517(83)90337-8

51. Grunze M, Driscoll RK, Burland GN, Cornish JCL, Pritchard J. Molecular and dissociative chemisorption of N2 on Ni(110). *Surf Sci*. 1979;89(1-3):381-390. doi:10.1016/0039-6028(79)90624-1

52. Parks EK, Nieman GC, Kerns KP, Riley SJ. The thermodynamics of nitrogen adsorption on nickel clusters: Ni19-Ni71. *J Chem Phys*. 1998;108(9):3731-3739. doi:10.1063/1.475779

53. Sugihara S, Kawamura Y, Iwai H. Formulation of steam-methane reforming rate in Ni–YSZ porous anode of solid oxide fuel cells. *Heat Mass Transf*. 2018;54(8):2497-

2505. doi:10.1007/s00231-018-2299-1

54. Incropera F. P., Dewitt D. P. *Introduction to Heat Transfer 3rd Edition.* John Wiley & Sons Inc.; 1996.

55. Bird R.B., Stewart W.E., Lightfoot E.N. *Transport Phenomena, 2 Edition.* John Wiley & Sons Inc.; 2006.

56. Bromley L.A., Wilke C. R. Viscosity behavior of gases. *Ind Eng Chem*. 1951;43:1641-1648.

57. The Japan Society of Fluid Mechanics. *Ryutai Rikigaku Handbook* [*Fluid Dynamics Handbook*]. Maruzen; 1998.

58. Campbell CT, Sellers JRV. The entropies of adsorbed molecules. *J Am Chem Soc*. 2012;134(43):18109-18115. doi:10.1021/ja3080117

59. Mhadeshwar AB, Wang H, Vlachos DG. Thermodynamic consistency in microkinetic development of surface reaction mechanisms. *J Phys Chem B.* 2003;107(46):12721-12733. doi:10.1021/jp034954y

60. Saha D, Deng S. Characteristics of ammonia adsorption on activated alumina. *J Chem Eng Data*. 2010;55(12):5587-5593. doi:10.1021/je100405k

Chapter 6

Conclusions

6.1 Conclusions

Use of a methane–ammonia mixed fuel for solid oxide fuel cells is proposed. The reaction characteristics of the mixed fuel on Ni–YSZ catalysts is experimentally investigated. The reaction model of the steam methane reforming and ammonia decomposition reactions under the competitive adsorption condition is proposed and the reaction rate formulae are introduced. The contents of each chapter can be summarized as follows.

In Chapter 1, solid oxide fuel cells (SOFCs) directly fed with non-hydrogen fuels are introduced. The advantages and challenges of the direct reforming SOFCs are addressed.

In Chapter 2, the concept of SOFCs fed with a mixed fuel is discussed. The aim of mixing fuels is to achieve the arbitrary control of cell temperature and the effective utilization of excess heat in the system by combining fuels with different reaction characteristics and activities. Among several possible combinations of hydrogen carriers, we adopted methane

and ammonia. The hydrogen reuse in the SOFCs is also an expected advantage. In this chapter, surface reactions on a Ni–YSZ (yttria-stabilized zirconia) catalyst is also discussed. Adsorption phenomena need to be considered to describe the competitive adsorption condition of the methane–ammonia mixed fuel. The reaction model of the mixed fuel can be constructed by using the overall adsorptions and associative reactions instead of a description based on the elementary reactions.

In Chapter 3, fundamental characteristics of the reforming and decomposition reactions of the methane–ammonia mixed fuel on a Ni–YSZ catalyst were experimentally investigated. A small amount of the crashed Ni–YSZ, which is a typical anode material of solid oxide fuel cells was packed in a thin quartz tube and a mixture gas of methane, ammonia, steam and balance argon was supplied. The test section was placed in an electric furnace to control the catalyst temperature. The exhaust gas compositions were measured by a gas chromatography varying the inlet gas composition and the furnace temperature. The reaction rates of the steam methane reforming and the ammonia decomposition were evaluated by measuring the exhaust gas compositions. It was found that the steam methane reforming reaction was suppressed by adding ammonia to the fuel. This suppression effect is particularly significant at relatively low temperatures. The steam methane reforming is almost completely suppressed while the ammonia decomposition reaction is not affected by the methane in the fuel at 600 °C. The suppression effects become moderate at higher temperatures when the ammonia concentration is relatively low. Under the conditions in which the methane reforming is sufficiently active, the ammonia decomposition is suppressed. This trade-off of the two reactions shows that they share the same reaction sites on the catalyst and are competing each other. The experimental results show that the ammonia decomposition is generally preferred but the methane reforming becomes non-negligible at higher temperatures when the ammonia

concentration is low.

In Chapter 4, several important characteristics as a fuel for solid oxide fuel cells of the methane–ammonia mixed fuel were experimentally investigated on the basis of the results reported in Chapter 3. The streamwise length of the catalyst region packed in the test tube was increased to 21 mm and 42 mm and the test section was placed in the electric furnace. The furnace was slightly opened to measure the temperature distribution of the catalyst with an infrared camera. The reaction rates of the steam methane reforming and the ammonia decomposition were evaluated by measuring the exhaust gas compositions using a gas chromatography. It was found that the difference of the reaction preference of methane and ammonia clearly affected the temperature distribution of the catalyst. As the mole fraction of ammonia in the mixed fuel was increased, ammonia was preferentially consumed and the reaction region of steam methane reforming on the catalyst was moved downstream, resulting in the shift of the position where the temperature of the catalyst sharply drops. By tuning the compositions of methane and ammonia in the mixed fuel, the temperature distribution was successfully controlled. When the mixture ratio of methane to ammonia was suitably adjusted, a higher hydrogen production rate was achieved compared with the cases of a single fuel of humidified methane or a single fuel of ammonia. The temperature difference within the catalyst was 56% smaller than that in the case of humidified methane, indicating that an improved durability of the system because of the less thermal stress. The amount of endothermic heat was 98% larger than that in the case of ammonia and almost equivalent to that in the case of methane, indicating the efficient heat utilization capability of the mixed fuel.

In Chapter 5, a reaction model to describe the reaction phenomena of the mixed fuel of methane and ammonia on a Ni–YSZ catalyst was proposed. The model includes the adsorption constants of participating chemical species to describe the competitive adsorption condition in the mixed fuel, while it does not consider the detailed elementary reactions to reduce the computational load because the proposed model is aimed to be applicable to stack level simulations. The model also considers the effect of catalyst support, namely YSZ, on the rate of steam methane reforming. By fitting the experimental data reported in Chapter 3 to the proposed model, the reaction rate formulae of the steam methane reforming and ammonia decomposition that can describe the mixed fuel conditions were successfully obtained. The new formulae can be regarded as more general expressions of the reaction rates compared to the equations reported so far and can be applicable to all kinds of numerical simulations. It was also found that YSZ, the catalyst support, gave some effect on the rate of the steam methane reforming.

6.2 Suggestions for Future Works

In this thesis, a methane–ammonia mixed fuel for solid oxide fuel cells is proposed. The reaction characteristics of the mixed fuel on Ni–YSZ catalyst are experimentally investigated. The reaction model of the steam methane reforming and ammonia decomposition under the competitive adsorption condition is constructed and the reaction rate formulae are introduced. Here, as for the suggestions for future study, two remaining related themes are discussed.

Firstly, to confirm the effectiveness of the methane–ammonia mixed fuel for solid oxide fuel cells, both experiment and simulation studies including the electrochemical reaction are expected. The power generation characteristics should be compared depending on the fuels. The hydrogen reuse effect can be also examined when the electricity generation is taken into account.

Secondly, the constructed model reported in Chapter 5 includes a crude assumption for the effect of catalyst support on the steam methane reforming reaction. It is certainly reported in the literature that the support gives an effect of steam methane reforming, however, the detail mechanisms are still unknown. Both of the kinetic study and experimental study for the effect of catalyst support are expected to update our model.

Nomenclature

A	Frequency factor	[–]
C_p	Molar heat capacity	[J mol^{-1} K^{-1}]
d	Inner diameter	[m]
E	Activation energy	[J]
F	Volumetric flow rate	[m^3 s^{-1}]
ΔG	Gibbs free energy change	[J]
ΔH	Enthalpy change	[kJ mol^{-1}]
K	Equilibrium constant	[–]
L	Length	[m]
M_j	Molar mass of species j	[kg mol^{-1}]
P_j	Partial pressure of species j	[Pa]
Q	Heat generation term	[W m^{-3}]
R	Ideal gas constant	[J mol^{-1} K^{-1}]
R_{ADC}	Reaction rate of ammonia decomposition	[mol m^{-2} s^{-1}]
R_{SMR}	Reaction rate of steam methane reforming	[mol m^{-2} s^{-1}]
ΔS	Entropy change	[J mol^{-1} K^{-1}]
S_j	Mass transport source term for species j	[kg m^{-3} s^{-1}]
$S'_{Ni\text{-}Pore}$	Ni–pore interface area density	[m^2 m^{-3}]
T	Temperature	[K]
T_f	Furnace temperature	[K]
V	Vacant reaction site on Ni surface	[–]
V_{cat}	Volume of catalyst	[m^3]

V_{rea}	Volume of reaction region in test section	[m^3]
v	Velocity	[m s^{-1}]
X_j	Molar fraction of species j	[–]
Y_j	Mass fraction of species j	[–]

Greek symbols

α	Emissivity	[–]
ε	Porosity	[–]
λ	Thermal conductivity	[W m^{-1} K^{-1}]
θ	Coverage	[–]
ρ	Density	[kg m^{-3}]
σ	Stefan-Boltzmann constant	[W m^{-2} K^{-4}]
μ	Viscosity	[Pa s]

Superscripts

0	Standard state
+	Forward reaction
–	Backward reaction

Subscripts

ad	Adsorption
ADC	Ammonia decomposition
cat	Catalyst
eq	Equilibrium state
EXP	Experiment

fur	Furnace
gas	Gas
i	Cell number
j	Species
rel	Relative value
SIM	Simulation
SMR	Steam methane reforming
V	Vacant reaction site
WGS	Water–gas shift reaction
0	Standard state